Development of Human Brain Sodium Magnetic Resonance Imaging (^{23}Na MRI) Methods

DEVELOPMENT OF HUMAN BRAIN SODIUM MAGNETIC RESONANCE IMAGING (^{23}Na MRI) METHODS

BY

Paul Polak, M.A.Sc

A THESIS
SUBMITTED TO THE SCHOOL OF BIOMEDICAL ENGINEERING
AND THE SCHOOL OF GRADUATE STUDIES
OF McMASTER UNIVERSITY
IN PARTIAL FULFILMENT OF THE REQUIREMENTS
FOR THE DEGREE OF
DOCTOR OF PHILOSOPHY

Doctor of Philosophy (2022)
School of Biomedical Engineering
McMaster University
Hamilton, Ontario

TITLE:	Development of Human Brain Sodium Magnetic Resonance Imaging (^{23}Na MRI) Methods
AUTHOR:	Paul Polak M.A.Sc (Biomedical Engineering) McMaster University, Hamilton, Canada
SUPERVISOR:	Dr. Michael D. Noseworthy
NUMBER OF PAGES:	xviii, 181

Abstract

Sodium (^{23}Na) plays a critical role in all organisms – it is crucial in cellular homeostasis, pH regulation and action potential propagation in muscle and neuronal fibres. Healthy cells have a low intracellular ^{23}Na and high extracellular concentration, with the sodium-potassium pump maintaining this sodium gradient. In the human brain approximately 50% of its total energy consumption is occupied by maintenance of this gradient, demonstrating the pump's importance in health. A failure of the sodium-potassium pump leads to cellular apoptosis and ultimately necrosis, with potentially disastrous results for neurological function.

Magnetic resonance imaging (MRI) of ^{23}Na is of great interest because of the ubiquity of sodium in cellular processes. However, it is hampered by many technical challenges. Among these are a low gyromagnetic ratio, short T_2^* relaxation times, and low concentrations all of which lead to long acquisitions in order to account for the poor inherent signal. In addition, ^{23}Na MRI requires specialized hardware, non-standard pulse sequences and reconstruction methods in order to create images. These have all contributed to render clinical applications for ^{23}Na MRI virtually non-existent, despite research indicating sodium's role in various neurological disorders, including multiple sclerosis, Alzheimer's, stroke, cancer, and traumatic brain injury.

This work is motivated by a desire to use ^{23}Na MRI in clinical settings. To that end, hardware and software methods were initially developed to process sodium images. In order to quantify the imaging system the point-spread function (PSF) and the related modulation transfer function (MTF) were calculated with the aid of a 3D-printed resolution phantom with different ^{23}Na concentrations in gelatin. Two pulse sequences, density-adapted projection reconstruction (DA-3DPR) and Fermat looped orthogonally encoded trajectories (FLORET), with similar acquisition times were tested. Reconstructions were performed with the non-uniform fast Fourier transform. Results indicated a full-width, half-maximum (FWHM) value of 1.8 for DA-3DPR and 2.3 for FLORET. In a follow-up study, simulation experiments were added to various sodium phantom concentrations in 3% agar. The simulations indicated high potential variability in the MTF calculations depending on the methodology, while the phantom experiments found a FWHMs of 2.0 (DA-3DPR), and 2.5 (FLORET).

Diffusion tensor imaging (DTI) is an MRI technique with wide adoption for the assessment of a variety of neurological disorders. Combining DTI with ^{23}Na MRI could provide novel insight into brain pathology; however, a study with a healthy population is warranted before examinations with other populations. Fifteen subjects were scanned with DTI and sodium MRI, and the latter was used to derive voxel-wise tissue sodium concentration (TSC). Regional grey and white matter (WM) TSC was analyzed and compared to fractional anisotropy (FA) and cerebrospinal fluid (CSF) proximity. Results indicated that WM voxels proximal to CSF regions (i.e. corpus callosum)

could have lower than expected FA values and higher measured TSC, with an inverse correlation between TSC and distance to CSF. This is likely the result of the broad PSF of ^{23}Na MRI, as regions distal to CSF did not exhibit this phenomenon. This potentially represents a confounding effect when interpreting sodium concentrations, especially in regions proximal to the high ^{23}Na content in CSF.

Acknowledgements

What a strange thing it is to write this section! After the last few years of struggles to get to this point it does seem a little surreal, and yet it is only fitting to recognize the people without whom none of this would be possible.

First and foremost my gratitude to my supervisor Dr. Michael D. Noseworthy. Mike is simply an exceptional graduate advisor with his encouragement, positivity, expertise, and flexibility. He treats his students with the utmost respect, and has inspired me to pursue independent ideas and research. Most graduate advisors have an admirable depth of knowledge in some particular field – Mike however has a breadth of knowledge that I have found unique in the academic world. To say that he has been an ideal supervisor for me is an understatement of the highest order.

Next to my supervising committee Carel DeMatteo, Dr. Gillian Ruth Goward and Dr. Troy Farncombe. Their guidance of this work has been essential, and I would not be writing this without their help. Thank you to all.

Norm Konyer is the Senior Scientific Officer at Imaging Research Centre in St. Joseph's Healthcare Hamilton. Norm is an absolute *magician* with radiofrequency coils, and he provided the expertise, tools, and wisdom to

help me in building the sodium coil. The consistency and quality I found in my experiments is due in no small measure to his guidance.

To my friends and labmates in the IRC – the pandemic has limited our personal interactions the last two years, and that is truly regrettable. But especially to Arv, Ethan, Cam, Alejandro, and Nick – all the very best! Thank you for being part of my graduate experience.

And finally my love and gratefulness for the support offered by Elizabeth Switzer and my family; both those who are still with us and those who are not – in memory forever bright.

Paul Polak
Denver, CO
April 3 2022

For Lizzes who has always been there for me, and
for Dave who I wish could still be.

Glossary

3DPR 3D projection reconstruction

ADC apparent diffusion coefficient

ADP adenosine diphosphate

ATP adenosine triphosphate

BART Berkeley Advanced Reconstruction Toolkit

BBB blood brain barrier

BLOSI Bloch-Siegert

BMI body mass index

CSF cerebrospinal fluid

DA-3DPR density adapted, 3D projection reconstruction

DCF density compensation function

DM direct modulation

DQC double quantum coherences

DTI diffusion tensor imaging

FFT fast Fourier transform

FH Fourier 1^{st} harmonic

FID free induction decay

FLORET Fermat looped orthogonally encoded trajectories

FOV field of view

FSL FMRIB Software Library

FWHM full width at half maximum

GM grey matter

$^{1}\boldsymbol{H}$ hydrogen

ISTO irreducible spherical tensor operator

MQC multiple quantum coherences

MRI magnetic resonance imaging

MS multiple sclerosis

MTF modulation transfer function

NMR nuclear magnetic resonance

NUFFT non-uniform fast Fourier transform

PSF point-spread function

$\boldsymbol{B_1^-}$ receive field

$\boldsymbol{B_1^+}$ transmit field

RF radiofrequency

ROI region of interest

SQC single quantum coherence

SNR signal to noise ratio

$\boldsymbol{^{23}Na}$ sodium

$[\boldsymbol{Na}]_{\boldsymbol{e}}$ extracellular sodium concentration

$[\boldsymbol{Na}]_{\boldsymbol{i}}$ intracellular sodium concentration

$\boldsymbol{Na^+K^+\!-ATPase}$ sodium-potassium pump

TA acquisition time

TBI traumatic brain injury

TE echo time

TQC triple quantum coherences

TR repetition time

TSC tissue sodium concentration

UTE ultra-short echo time

VGSC voltage gated sodium channels

WM white matter

Contents

List of Figures

Chapter 1

Introduction

Magnetic resonance imaging (MRI) is an established in vivo medical imaging modality. It is an essential tool in modern clinical practice, with applications in neurology, cardiology, oncology, orthopedics, and pediatrics representing only a partial list. MRI is based upon the interactions of hydrogen (^1H) atoms, a main magnetic field, radiofrequency (RF) and magnetic gradient pulses in order to create an image. In fact, the term MRI is usually taken to mean hydrogen or "proton MRI" because this type of scanning dominates the modality. Most do not realize that MRI can be done (in theory) using a significant variety of nuclei. The physics behind magnetic resonance indicates that there are many other nuclei that occur in vivo which would be interesting to image, including ^{31}P, ^{13}C, and sodium (^{23}Na).

^{23}Na is the most abundant cation in vivo, and is essential to metabolic processes, making it an attractive candidate to image with magnetic resonance techniques. Unfortunately, numerous technical challenges abound, including a low gyromagnetic ratio, short T_2^* relaxation times, and poor ^{23}Na

concentration (relative to hydrogen). These combine to produce low signal to noise ratios (SNR) for ^{23}Na MRI, leading to large imaging voxels and long acquisition times. Despite these difficulties, ^{23}Na MRI remains an attractive prospect for brain imaging, because of sodium's essential role in various pathologies, including multiple sclerosis (MS), stroke, epilepsy, cancer and traumatic brain injury. Thus, there is considerable interest in developing robust methods for ^{23}Na brain MRI.

1.1 Outline

This thesis follows the McMaster University format of a "sandwich thesis", such that published or submitted material is surrounded with opening chapters and a summary and conclusions chapter at the end. The main objectives for this work were focused on the development of methods for sodium brain MRI, and are as follows:

1. Build, tune, and match a radiofrequency (RF) head coil compatible with a clinical General Electric Healthcare 3 T MRI.
2. Develop an MRI pulse sequence which can capture and spatially encode the ^{23}Na signal from an MRI experiment.
3. Implement an image reconstruction pipeline for ^{23}Na.
4. Design and build a resolution phantom to allow quantification of imaging system performance.
5. Generate a tissue sodium content (TSC) imaging procedure which balances the low signal of ^{23}Na MRI with acquisition times which are

clinically viable.

Chapter 2 discusses some of the biological motivation behind this work, including an overview of the sodium-potassium pump. This chapter also outlines sodium's role in various neurological disorders, and demonstrates the potential for ^{23}Na MRI.

Chapter 3 investigates the nuclear magnetic resonance (NMR) properties of sodium. The most notable difference between ^{23}Na and proton MRI from a physics perspective is that sodium's spin is 3/2, which leads to magnetic *and* electric terms in its energy equation. This leads to more complicated NMR spectra, and influences the design choices when developing the imaging methods. It also discusses intra- and extracellular ^{23}Na concentrations and their contributions to the observed tissue sodium concentration.

Chapter 4 contains a review of MRI theory, including signal generation, spatial encoding, ^{23}Na pulse sequences and non-Cartesian image reconstruction. It also gives an overview of the point-spread function (PSF) and its related modulation transfer function (MTF), both of which are used to quantify imaging performance.

In Chapter 5 the objectives and hypotheses contained in this dissertation are described. One of the goals was to study mild traumatic brain injury with sodium MRI scanning. However, this became impossible for two reasons due to Covid-19. First of all research MRI scanning was cancelled for almost two years. The second reason was that during Covid there was a significant reduction in concussions (almost to zero) due to the cancellation of recreational and varsity sports.

The development of any imaging method should also have associated with it the techniques to quantify performance. One such measurement is the PSF; however, this can be difficult to measure directly. Chapter 6 is a pilot study that outlines the measurement of the MTF in a 3D-printed phantom – the MTF being related to the PSF by the Fourier transform. Three sodium concentrations in gelatin were used as the testing medium, and imaging performance was evaluated in both density adapted, 3D projection reconstruction (DA-3DPR) and Fermat looped orthogonally encoded trajectories (FLORET). These techniques and the 3D-printed phantom can be readily applied to measure the MTF in other applications.

Chapter 7 expands upon the previous chapter, and uses sodium suspended in an agar solution as the medium in the imaging experiments. A simulation study was also conducted to determine the effect of imaging noise on the evaluation of the MTF, under two methodologies: direct modulation, and one based on Fourier harmonics. The imaging performance of DA-3DPR and FLORET pulse sequences were then evaluated in the phantom, and the MTFs were calculated by both MTF methods. The results indicate that: (i) the Fourier harmonic MTF quantification is less affected by imaging noise, and (ii) image SNR and the PSF are largely indifferent to acquisition type.

Diffusion tensor imaging (DTI) provides information on brain structure by measuring the unrestricted or restricted diffusion of water. DTI is used to evaluate pathology in a wide array of brain disorders. ^{23}Na brain MRI could provide complementary information; however, there are few studies in the literature combining these two techniques. Chapter 8 provides details into the investigation of combining ^{23}Na MRI with proton DTI in fifteen healthy subjects, to provide a “baseline” of complementary information. The results indicate that areas near sources of cerebrospinal fluid (CSF) have a higher measured ^{23}Na concentration – the likely effect of a broad PSF confounding the high sodium concentration in the CSF with surrounding tissue. This is potentially problematic for examining ^{23}Na concentration in white matter pathologies, as the largest bundle of white matter (i.e. the corpus callosum) is proximal to the lateral ventricles. Despite this caveat, DTI and ^{23}Na provide information on the brain structure and sodium concentration, and could be jointly useful in investigating pathology.

Chapter 9 summarizes this dissertation, provides conclusions and suggests areas for further research.

Chapter 2

Biological Aspects of Sodium

2.1 Sodium Function in Healthy Tissue

Sodium (^{23}Na) is an essential ion in living organisms, responsible for cellular homeostasis, pH regulations, fluid balance, and action potentials in muscle and neuronal fibres [1–4]. It has an essential role in various trans-membrane ionic exchanges, including sodium-calcium exchange, sodium-bicarbonate co-transporter, and the sodium-potassium-activated adenosine triphosphatase ($Na^+K^+-ATPase$ i.e. the sodium-potassium pump, see figure 2.1), which pumps 3 Na^+ out of the cell into the extracellular space, replacing them with 2 K^+ ions. This process is driven against the electrochemical gradient (i.e. keeping extracellular sodium higher and intracellular potassium lower), and thus requires energy provided by the hydrolysis of adenosine triphosphate (ATP) [1,2]. Disruptions that occur in the sodium-potassium pump leads to increased intracellular ^{23}Na concentration, ($[Na]_i$), which can prelude cellular apoptosis or necrosis. The normal $[Na]_i$ is $\approx$ 15 mM, while the extracellular concentration ($[Na]_e$) is $\approx$ 140 mM.

Maintenance of the electrochemical gradient in cells as a percentage of the total energy consumption varies as to the relevant organ. In the heart, $\approx$ 15% of the energy is related to "non-service" mechanisms – that is, energy consumption for the purpose of organ maintenance, rather than "service" function which benefits the entire body (i.e. cardiac cycle) [3]. In the brain, this percentage rises to $\approx$ 50% [3]. This high relative percentage of energy consumed in maintaining the gradient indicates the importance of the sodium-potassium pump in healthy brain tissue.

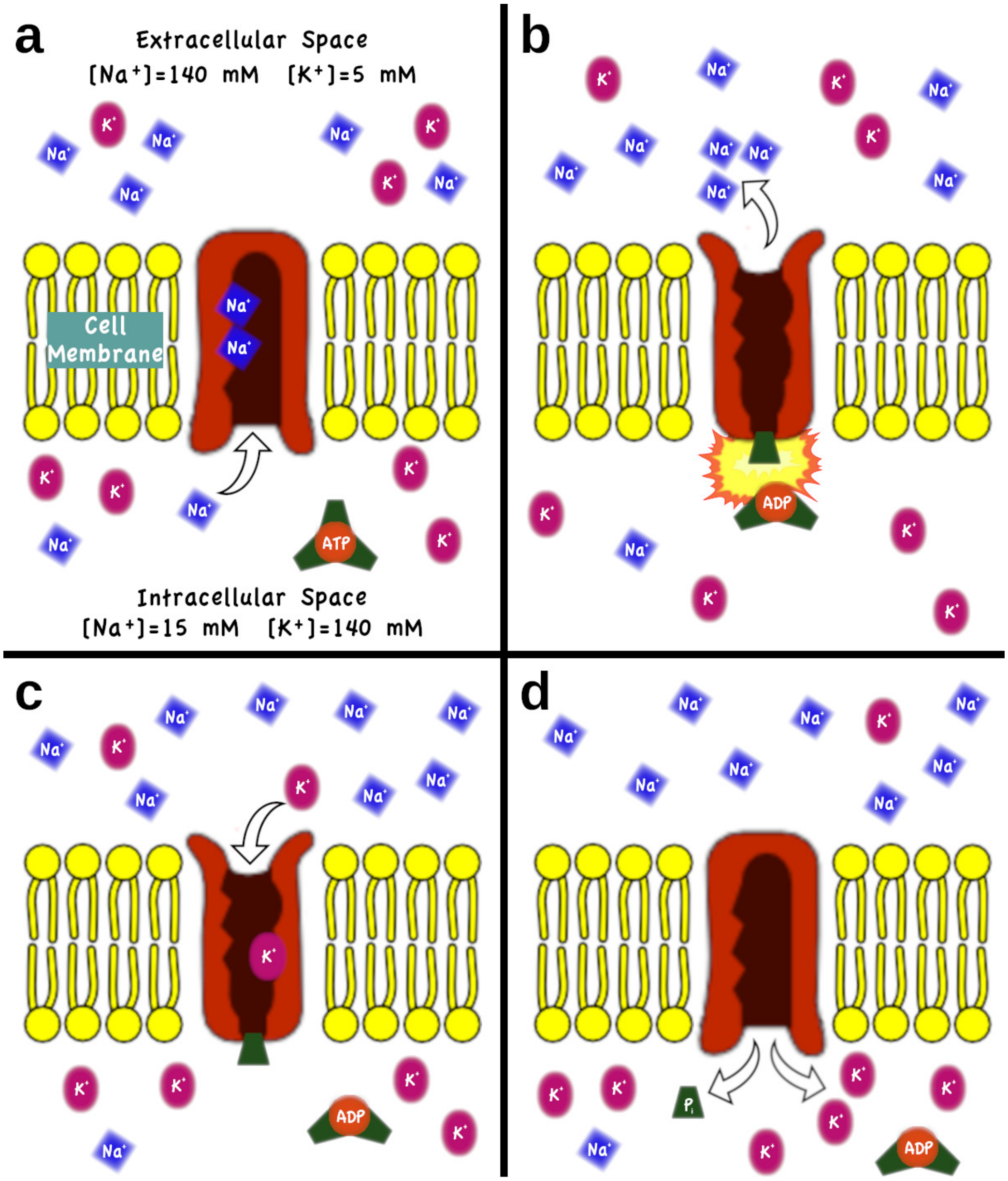

Figure 2.1: Sodium-potassium pump. (a) Na+ ions move into ion channel (b) ATP provides energy to open ion channel and 3 Na+ ions released to the extracellular space – adenosine diphosphate (ADP) released by process (c) Open channel attracts 2 K+ ions and (d) channel reverts to closed state, releasing inorganic phosphate and 2 K+ to intracellular space. Original illustration by author with free clip art provided by: https://www.clker.com.

2.2 Sodium Dysfunction in Brain Diseases

Sodium plays an important role in healthy brain function, with the careful balance between $[Na]_i$ and $[Na]_e$ maintained by the $Na^+K^+-ATPase$. As such, we might expect sodium concentrations to be disrupted from homeostasis during a neurological disorder. Common brain disorders, as outlined in Law et al. [5], cite the following as the most important problems in neuroradiology:

1. Infection and inflammation
2. Metabolic disorders
3. Tumor
4. Trauma
5. Congenital abnormalities
6. Epilepsy
7. Hypoxia and ischemia

In regards specifically to the above, we briefly discuss ^{23}Na in terms of the specific maladies of Multiple Sclerosis (MS) (1 above), Alzheimer's (2), cancer (3), epilepsy (6), stroke (7), and traumatic brain injury (TBI) (4).

2.2.1 Multiple Sclerosis

Multiple Sclerosis is a demyelinating disease characterized by focal lesions which are visible with proton (^1H) T_2 magnetic resonance imaging (MRI).

Demyelination of axons reduces the conduction potential in white matter (WM) [6,7] leading to patient disability. In addition, an elevation of nitric oxide interferes with normal mitochondria function, and a reduced production of ATP [6]. The breakdown of the $Na^+K^+-ATPase$ mechanism follows, as eventually ATP stores are exhausted [8,9]. This leads to an increase in $[Na]_i$, which coupled with the sodium-calcium exchange allows Ca^{2+} to accumulate inside the cell. Increased intracellular calcium migrates to the mitochondria further impairing ATP production and exasperating the energy crisis. An influx of calcium has been shown to be fatal to cells [10,11], likely due to the ubiquitous nature of calcium as an important second messenger.

As a chronic disease, there is particular interest in uncovering the progression of MS over time, and in an examination of the temporal evolution of WM lesions, Eisele et al. [12] measured ^1H diffusion and tissue sodium concentration (TSC). The findings indicated a reduced apparent diffusion coefficient (ADC) and normal TSC in newly formed lesions. The authors suggested that this indicates a mostly intact underlying tissue structure and thus a potential target for early therapeutics, as these lesions have not yet resulted in a breakdown of the blood brain barrier (BBB). Over time, the ADC and TSC in these newly formed lesions “normalized” to the measures found in older lesions, potentially indicating damage to the BBB.

2.2.2 Alzheimer’s Disease

Alzheimer’s disease is a debilitating and progressive form of dementia that produces memory loss, behavioral changes, and cognitive impairment [13]. Structurally, Alzheimer’s is characterized by brain atrophy and this is most easily evaluated with structural ^{1}H MRI. However, there are also metabolic markers in Alzheimer's, including down regulation of glucose metabolism [14] which can precede cognitive symptoms by years [15]. Positron emission tomography can be used to evaluate metabolic function in the brain; however, ^{23}Na MRI can provide a non-invasive alternative in detecting tissue disintegration and potentially provide a biomarker to track disease progression. Mellon et al. [16] and Mohamed et al. [17] used ^{23}Na MRI to detect increases in TSC in patients with Alzheimer's compared to controls. While these were comparatively small studies, their results indicate that further research into the use of ^{23}Na MRI for Alzheimer's disease is needed.

2.2.3 Cancer

Brain tumors represent a relatively small subset of diagnosed cancers; however, they are among the most deadly [18, 19]. A hallmark of the most aggressive brain tumors is rapid angiogenesis, as these tumors rapidly outstrip their blood supply, resulting in an upregulation of factors which further increase vessel formation and lead to tumor growth in a vicious cycle [20,21]. Both angiogenesis and tumor cell proliferation are associated with a reduced $Na^{+}K^{+} - ATPase$, resulting in an increase in $[Na]_{i}$. An elevated TSC is also linked with tumor malignancy [22, 23]. The increased TSC has been attributed with both an increase in intracellular sodium, and in the extracellular volume fraction – both of which are associated with cellular proliferation [24].

2.2.4 Epilepsy

Action potentials are generated and propagated by the voltage gated sodium channels (VGSC). Genetic mutations can cause the malformations of the VGSC, and is why epilepsy can also be described as a "channelopathy" [25]. Dysfunction of these channels can lead to $Na^+K^+-ATPase$ disruptions, with the result an increase in $[Na]_i$ [26]. Chronic epilepsy has been shown to lead to an increase in the extracellular volume, leading to alterations in the TSC [27]. Preclinical MRI by Wang et al. indicated a decrease in apparent diffusion coefficient and an increase in TSC when seizures were instigated in rats [28] – the authors interpreted this as being related to ^{23}Na migration into the excited neurons. In a ^{23}Na MRI study of 9 patients with epilepsy, Ridley et al. found an increase in TSC in the regions identified as epileptogenic [29]. However, despite these promising initial imaging studies the precise role that ^{23}Na plays in epilepsy has not been fully investigated. In particular, how TSC alters before and after seizures has not been elucidated [30].

2.2.5 Stroke

Strokes have two subtypes- occlusive and hemorrhagic, where the former involves the lodging of a clot or thrombus in an artery/arteriole in the brain, while the latter involves the rupture of a weakened blood vessel and subsequent catastrophic intracranial bleeding. The clinical management of both subtypes is notably different. In terms of sodium all MRI work has focused on occlusive stroke, which occurs as a result of a loss of perfusion to brain tissue. The usual treatment is to administer a recombinant tissue plasmogen (tPa) within a narrow window (within 3 hours) after onset. The volume of viable tissue is typically estimated with the difference between the perfusion weighted images and ADC from ^1H MRI [31], known as diffusion-perfusion mismatch. The bigger the mismatch the greater the potential for recovery if the thrombus is removed. Treatment with tPa is often not administered when either the diffusion-perfusion mismatch is too small, or more than 3 hours has passed since stroke onset. However, this procedure can underestimate treatment potential – TSC has been shown to indicate viable tissue outside of the perfusion-diffusion mismatch [32, 33].

2.2.6 Traumatic Brain Injury

Unlike MS, stroke or cancer, traumatic brain injuries (TBI) occur as a result of an acute event, and are not typically degenerative in their mild form. The mechanical and physiological injuries are a result of complex interactions of rotational, shearing, linear and decelerating events [34, 35]. The physical forces cause damage to the underlying structure of brain tissue, and can result in axonal dysfunction, ionic fluxes, and neurotransmitter disorder [36]. Complicating TBI in vivo is that the TBI events are unique from patient to patient, resulting in spatially heterogeneous manifestations of insult. These "diffuse axonal injuries" can occur in any WM tissue, although by the nature of its central location (a form of pivot point) and the fact it is an exceptionally dense bundle of fibers the corpus callosum is a common region [37–39] where damage is seen.

The complete neurometabolic consequences as a result of a TBI is extensive and complicated, and a variety of intersecting processes have been found.

Studies have found increased glutamate in the synaptic cleft following a TBI event, which results in excessive/prolonged stimulation of glutamate receptors [36, 40, 41]. This subsequently leads to a dysregulation of potassium, as the extracellular concentration of K^+ increases. Furthermore, this then places an increased burden on the Na^+K^+–$ATPase$, as the escalated demand forces cells to exhaust their ATP stores. At this point the TBI cascade resembles that which occurs in MS: as the ATP is exhausted, $[Na]_i$ increases, and the sodium-calcium exchange causes the concentration of Ca^{2+} to increase in mitochondria [42, 43]. The result is impaired mitochondrial function and further aggravation of the cellular energy crisis. Again, the increase in $[Na]_i$ precedes the resulting dysfunction and potential necrosis in axonal tissue.

Initial efforts to image the effects of TBI with ^{23}Na MRI indicated that TSC was reduced in patients with TBI compared to controls [44, 45]. It should be noted that these studies were somewhat limited in scope, and more investigation in this area is warranted.

In summary, of the seven most important problems in neuroradiology, the literature provides evidence of the efficacy of ^{23}Na MRI for MS, Alzheimer's, cancer, epilepsy, stroke and TBI. In particular, ^{23}Na MRI can provide vital information about metabolic biomarkers, which are prevalent for all of these brain disorders. In the next chapter we will examine some of the underlying physics and principles of ^{23}Na and how these influence image acquisition with MRI.

Chapter 3

Magnetic Resonance Aspects of Sodium

3.1 Spin Physics

Spin is a fundamental quantum mechanical property of subatomic particles, in a similar manner to mass or electric charge – it can be viewed as the intrinsic angular momentum of a particle. From a classical physics view, spin is often conceived as a child's top or gyroscope – although incorrect from a quantum perspective, this analogy is useful from a visualization standpoint, and will be the vantage adopted from this point forward.

For nuclear magnetic resonance (NMR) and MRI experiments, we are only concerned with nuclei that generate a non-zero spin, since zero spin systems are invisible to NMR. Although the precise spin number, I is determined by experimentation, a few heuristics can be stated here [46]:

- Nuclei with an even number of protons and neutrons produce no net spin (i.e. ^{12}C, ^{16}O: $I = 0$)

- Nuclei with an odd number of protons and neutrons produce a net spin of whole integers (i.e. ^{14}N: $I = 1$)
- Nuclei with an even/odd or odd/even number of protons and neutrons has a net spin of half integers (i.e. ^{1}H, ^{31}P: $I = 1/2$, ^{23}Na: $I = 3/2$)

A spin of 3/2 is significantly more complicated than the more commonly seen 1/2 as seen in ^{1}H MRI.

3.2 Energy of ^{23}Na Spin Systems

The time-dependent Schrödinger wave equation includes the Hamiltonian operator and describes the interactions of all the particles in the spin system[1]:

$$\frac{d}{dt}|\psi(t)\rangle = -i\widehat{\mathcal{H}}|\psi(t)\rangle \tag{3.1}$$

This equation is complete, but not particularly useful – it includes all the interactions between nuclei and electrons. This entails information about their velocities, positions, and spin states (i.e. $|\psi(t)\rangle$), and cannot be realistically solved in any practical manner. Instead, in the remainder of this text we will use the *spin Hamiltonian hypothesis* [47], which allows us to only consider the nuclear spin states, and their associated Hamiltonian, $\widehat{\mathcal{H}}_{spin}$. This hypothesis states that electron motion is so rapid that their influences can be averaged,

---

[1] In this text, operators are denoted by a hat notation $\hat{A}$, vector quantities are denoted in boldface, ($\boldsymbol{A}$), vector operators are hat boldface ($\hat{\boldsymbol{A}}$), and scalars are in regular face (A).

and only their aggregate effect upon nuclei be considered. Moreover, this combined effect can be contained in the $\widehat{\mathcal{H}}_{spin}$ operator. In addition, the spin energy of the nuclei are too small to affect either the movement of the electrons around the molecules, or the motion of the molecules themselves. Thus, we can restate equation 3.1 as referring to only the *spin states* of the nuclei in question. Henceforth, further references to the Hamiltonians of the various subsystems are to be considered with this hypothesis and resulting simplification of equation 3.1:

$$\frac{d}{dt}|\psi_{spin}(t)\rangle = -i\widehat{\mathcal{H}}_{spin}|\psi_{spin}(t)\rangle. \tag{3.2}$$

The nucleus in an NMR experiment interacts with the surrounding electrical and magnetic fields. What follows here is the rationale for which terms of the Hamiltonian are most important for a ^{23}Na spin $I = 3/2$ system, and which terms are of "lesser" (in terms of magnitude) importance and are typically ignored. For further details of the following derivations, the reader is directed to the excellent texts by Slichter [48] and Levitt [47].

It should also be noted that the work considered in this text are ^{23}Na experiments with single quantum coherence (SQC) (i.e. a single radiofrequency (RF) pulse followed by readout). Moreover, I have avoided introducing the irreducible spherical tensor operator (ISTO) basis in an attempt to minimize overly complicated derivations. However, the ISTO notation can be highly useful, particularly when describing experiments on multiple quantum coherences (MQC). If interested, the reader is directed to texts [49–54].

3.2.1 Hamiltonian

In terms of the system energy in NMR, we can examine the total energy, or Hamiltonian, of the system as:

$$\widehat{\mathcal{H}} = \widehat{\mathcal{H}}_{mag} + \widehat{\mathcal{H}}_{elec}. \tag{3.3}$$

The magnetic dipole interacts with the surrounding magnetic field, and the electric charge interacts with the electric field – it is important to note that as the nucleus rotates in these fields, the energy from each component changes. Moreover, the electric charge is not a simple point charge, but is instead distributed, possibly unevenly, throughout the nucleus. Thus its motion is more akin to an irregular, "lumpy" magnet, than a simple dipole. Further, we can classify any influences on the nuclei through the magnetic or electrical fields as either *external* or *internal* spin interactions.

3.3 Magnetic Field Interactions

For our purposes, we consider that all the *external* spin interactions are magnetic field interactions [47], and these can be separated into those provided by the static field, RF, and gradient fields. We can thus write the Hamiltonian of the magnetic field as:

$$\widehat{\mathcal{H}}_{mag} = \widehat{\mathcal{H}}_{static} + \widehat{\mathcal{H}}_{RF} + \widehat{\mathcal{H}}_{gradient}. \tag{3.4}$$

All terms in equation 3.4 are taken as the sum for all spins in the NMR experiment – so if k is some spin in our sample, we can write:

$$\begin{aligned}
\widehat{\mathcal{H}}_{static} &= \sum_k \widehat{\mathcal{H}}_{k,static} \\
\widehat{\mathcal{H}}_{RF} &= \sum_k \widehat{\mathcal{H}}_{k,RF} \\
\widehat{\mathcal{H}}_{gradient} &= \sum_k \widehat{\mathcal{H}}_{k,gradient}
\end{aligned}$$

3.3.1 Static Field

The magnetic dipole moment of the nucleus will interact with the surrounding main magnetic field. If we define this magnetic field to be oriented along the positive z axis we can write:

$$\boldsymbol{B_z} = B_0\boldsymbol{z} \tag{3.5}$$

where B_z is the strength of the static magnetic field, and $\boldsymbol{z}$ is a unit vector along the field direction. The angular momentum ($\hat{\boldsymbol{S}}$) of the nucleus is defined as:

$$\begin{aligned}
\hat{S}_x &= -i\left(\frac{\partial y}{\partial z} - \frac{\partial z}{\partial y}\right) = -i(\hat{y}\hat{D}_z - \hat{z}\hat{D}_y) \qquad (3.6) \\
\hat{S}_y &= -i(\hat{z}\hat{D}_x - \hat{x}\hat{D}_z) \\
\hat{S}_z &= -i(\hat{x}\hat{D}_y - \hat{y}\hat{D}_x)
\end{aligned}$$

for each component along the main Cartesian axes, and where $\hat{D}_n$ is the partial derivative taken along n. The magnitude of the angular momentum is in units of the reduced Planck's constant ($\hbar\sqrt{I(I+1)}$), and is related also to the spin number. The relationship between the magnetic moment, $\boldsymbol{\mu}$ and the angular momentum is governed by:

$$\boldsymbol{\mu} = \gamma\hat{\boldsymbol{S}} \tag{3.7}$$

where γ is the gyromagnetic ratio of the nucleus, and is a numeric quantity measured by experiment. The energy for each spin as a result of its interaction with the external magnetic field is:

$$\begin{aligned} \widehat{\mathcal{H}}_{static} &= -\boldsymbol{\mu}\cdot\boldsymbol{B_z} && (3.8)\\ &= -\gamma B_0 \hat{S}_z. && (3.9) \end{aligned}$$

This is the term for the energy due to the static field, and is also called the *nuclear Zeeman interaction*, and arises out of the consequences of *Zeeman splitting* as demonstrated by the Stern and Gerlach experiments [55]. For further reading with historical context of the Stern-Gerlach experiments, the reader is directed to the article by Schmidt-Böcking [56].

The Zeeman splittings as observed in the above are quantized into distinct states based upon the angular momentum in the nuclei. Thus, the number of states is based upon the spin number, I, and is equal to $2I + 1$ possible values – enumerated as:

$$m_s = -I, -I+1, -I+2, \ldots, I-1, I. \tag{3.10}$$

If we examine the energy required for the single transition for a spin $I = 1/2$ NMR system – that is, a transition from $m_s = 1/2$ to $m_s = -1/2$ we have:

$$\begin{aligned} \Delta E &= E_{m_s=-1/2} - E_{m_s=1/2} \\ &= -\gamma B_0 \left(\frac{-1}{2} \hbar \right) - \left(-\gamma B_0 \left(\frac{1}{2} \hbar \right) \right) \\ &= \hbar \gamma B_0. \end{aligned}$$

We can then define the energy in terms of the reduced Planck's constant:

$$\frac{\Delta E}{\hbar} = \gamma B_0 = \omega_0. \tag{3.11}$$

The term ω_0 is also known as the *Larmor frequency* of the NMR system, and it is a critical component for any MRI experiment. For ^{23}Na, with a spin system of I = 3/2, there are 4 distinct energy states, and these are enumerated as spin states: $|\frac{-3}{2}\rangle, |\frac{-1}{2}\rangle, |\frac{1}{2}]\rangle$, and $|\frac{3}{2}\rangle$ (figure 3.1). Transitions between $|\frac{-3}{2}\rangle$ and $|\frac{-1}{2}\rangle$ or $|\frac{3}{2}\rangle$ and $|\frac{1}{2}\rangle$ are called *satellite* transitions, while those between $|\frac{-1}{2}\rangle$ and $|\frac{1}{2}\rangle$ are the *central* transitions.

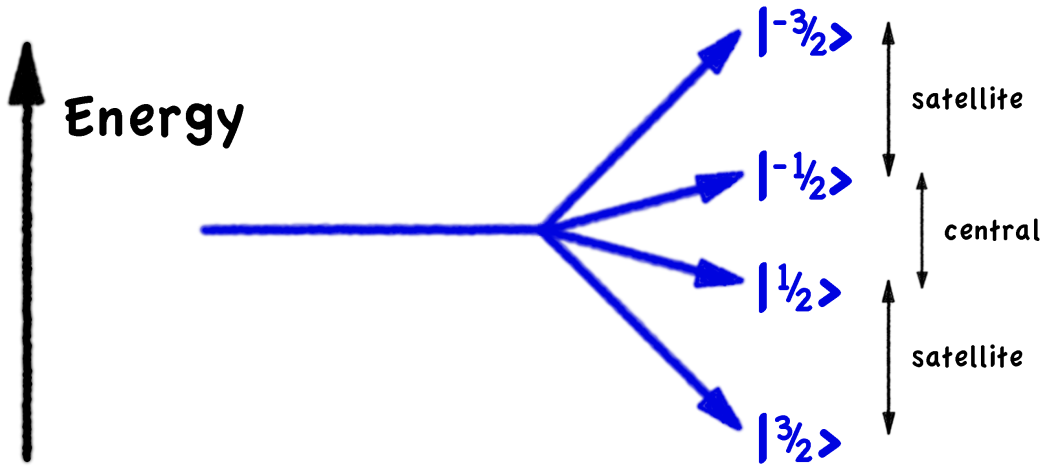

Figure 3.1: Detailing the four spin states of ^{23}Na. In a single quantum filter NMR experiment, there are two satellite transitions possible: $\frac{-3}{2} \rightleftharpoons \frac{-1}{2}$ and $\frac{3}{2} \rightleftharpoons \frac{1}{2}$, and a single central transition: $\frac{-1}{2} \rightleftharpoons \frac{1}{2}$.

3.3.2 RF Field

In an NMR experiment the spins are initially aligned along the main magnetic field parallel to the z-axis. Upon application of an RF pulse these spins are rotated into the xy-plane. If the RF pulse is applied at the Larmor frequency, the time dependent RF Hamilton in the rotating frame is:

$$\begin{aligned} \widehat{\mathcal{H}}_{RF} &= \omega_{RF}\hat{S}_r \\ &= \gamma B_1(t)\hat{S}_r \end{aligned}$$

where $B_1(t)$ is the RF envelope and $\hat{S}_r$ is the angular momentum in the rotating frame. In the reference or "laboratory" static frame, we can express this as:

$$\widehat{\mathcal{H}}_{RF} = \gamma B_1(t)\left[\cos(\omega_0 t)\hat{S}_x + \sin(\omega_0 t)\hat{S}_y\right] \tag{3.12}$$

In practice the magnitude of the $B_1(t)$ term is orders of magnitude less than B_0, and thus the ω_{RF} is considerably less than ω_0.

3.3.3 Gradient Field

The gradient field interactions of a spin j, located at position $\boldsymbol{r} = (x, y, z)$ in a molecule in the laboratory frame along the main magnetic field $\boldsymbol{B_z}$, with a field gradient magnitudes G_x, G_y, G_z, is:

$$\begin{aligned}\widehat{\mathcal{H}}_{j,grad_x}(\boldsymbol{r},t) &= -\gamma G_x(t)x\hat{S}_jz \\ \widehat{\mathcal{H}}_{j,grad_y}(\boldsymbol{r},t) &= -\gamma G_y(t)y\hat{S}_jz \\ \widehat{\mathcal{H}}_{j,grad_z}(\boldsymbol{r},t) &= -\gamma G_z(t)z\hat{S}_jz \qquad (3.13)\end{aligned}$$

for the three components of $\boldsymbol{r}$. Note the presence of $\hat{S}_jz$ for each component – this is because the gradient field magnitudes are considerably less than that of the static field B_0 in a typical NMR or MRI experiment (i.e. $G_x, G_y, G_z \ll B_0$). As a result, we can usually ignore the effects of the transverse gradient fields when considering the spin Hamiltonian.

3.4 Electric Field Interactions

Examining the electrical energy term, we can write the energy as the distribution of charge $\mathcal{Q}(\boldsymbol{r})$ interacting with the electric potential $\Psi(\boldsymbol{r})$, over some volume as:

$$E_{elec} = \int_{vol} \mathcal{Q}(\boldsymbol{r})\Psi(\boldsymbol{r})\ d\boldsymbol{r} \qquad (3.14)$$

It is convenient to break down the charge distribution into components:

$$\mathcal{Q}(\boldsymbol{r}) = \sum_{i=0}^{n} \mathcal{Q}_i(\boldsymbol{r}) \qquad (3.15)$$

where $\mathcal{Q}_0(\boldsymbol{r})$ is the spherical charge distribution, $\mathcal{Q}_1(\boldsymbol{r})$ the dipole charge distribution, $\mathcal{Q}_2(\boldsymbol{r})$ the quadrupolar, etc. In terms of the magnitudes: $|\mathcal{Q}_0(\boldsymbol{r})|$ is the total electric charge of the nucleus, $|\mathcal{Q}_1(\boldsymbol{r})|$ is the electric dipole moment, and so on.

Similarly, the electric potential can also be viewed as a superposition of terms:

$$\Psi(\boldsymbol{r}) = \sum_{i=0}^{n} \Psi_i(\boldsymbol{r}) \tag{3.16}$$

where $\Psi_0(\boldsymbol{r})$ is the electric potential at the center of the nucleus, $\Psi_1(\boldsymbol{r})$ the gradient of the electric potential at the center, $\Psi_2(\boldsymbol{r})$ the gradient of the gradient of the electric potential, etc.

We can then restate equation 3.14 in terms of the individual elements of the nucleus interacting with the field. So this becomes the energy of the spherical charge distribution interacting with the electric potential, the dipole charge with the gradient of the electric potential, the quadrupolar charge with the gradient of the gradient, etc:

$$\begin{aligned} E_{elec} &= E_{elec,0} + E_{elec,1} + E_{elec,2} + E_{elec,3} + \cdots \\ &= \int \mathcal{Q}_0(\boldsymbol{r})\Psi_0(\boldsymbol{r})\ d(\boldsymbol{r}) + \int \mathcal{Q}_1(\boldsymbol{r})\Psi_1(\boldsymbol{r})\ d(\boldsymbol{r}) + \\ &\quad \int \mathcal{Q}_2(\boldsymbol{r})\Psi_2(\boldsymbol{r})\ d(\boldsymbol{r}) + \int \mathcal{Q}_3(\boldsymbol{r})\Psi_3(\boldsymbol{r})\ d(\boldsymbol{r}) + \cdots . \end{aligned} \tag{3.17}$$

At this point, a number of simplifications can be made to equation 3.17:

1. The $E_{elec,0}$ is the energy from the point charge at the center of the nucleus. It is responsible for holding the nucleus together, but has no effect on NMR experiments.

2. Under the principle of *parity conservation*, the $E_{elec,1}, E_{elec,3}, E_{elec,5}, \ldots$ terms all vanish – in effect, there is no electric dipole moment within

experimental error.

3. A symmetric property based on the shape of the nucleus and its spin system I dictates that: $\mathcal{Q}_i(\boldsymbol{r}) = 0$, for $i > 2I$.

(For further discussion of these, refer to [48]).

With regards to point (3) above, for a spin system of $I = 1/2$, this results in terms: $E_{elec,2}, E_{elec,3}, \ldots$ also vanishing in equation 3.17, and thus the entire electrical energy portion of the Hamiltonian is 0 for spin 1/2 systems. Thus ^1H, ^{31}P, and other spin 1/2 nuclei are only under the influence of the magnetic field effects as per equation 3.3. These nuclei can be thought of as a "bar magnet" in the magnetic field, and this greatly simplifies the resulting Hamiltonian.

However, for quadrupolar nuclei like ^{23}Na, with a spin system of $I = 3/2$, the $E_{elec,2}$ term remains in equation 3.17. This is the *quadrupolar* term, and represents the interaction of the quadrupole charge distribution interacting with the gradient of the electric field. To use our previous analogy, ^{23}Na is an irregular magnet, interacting with both the electric and magnetic fields (figure 3.2). Our Hamiltonian for the electrical energy term is now reduced to that for the quadrupolar term:

$$\widehat{\mathcal{H}}_{elec} = \widehat{\mathcal{H}}_Q. \tag{3.18}$$

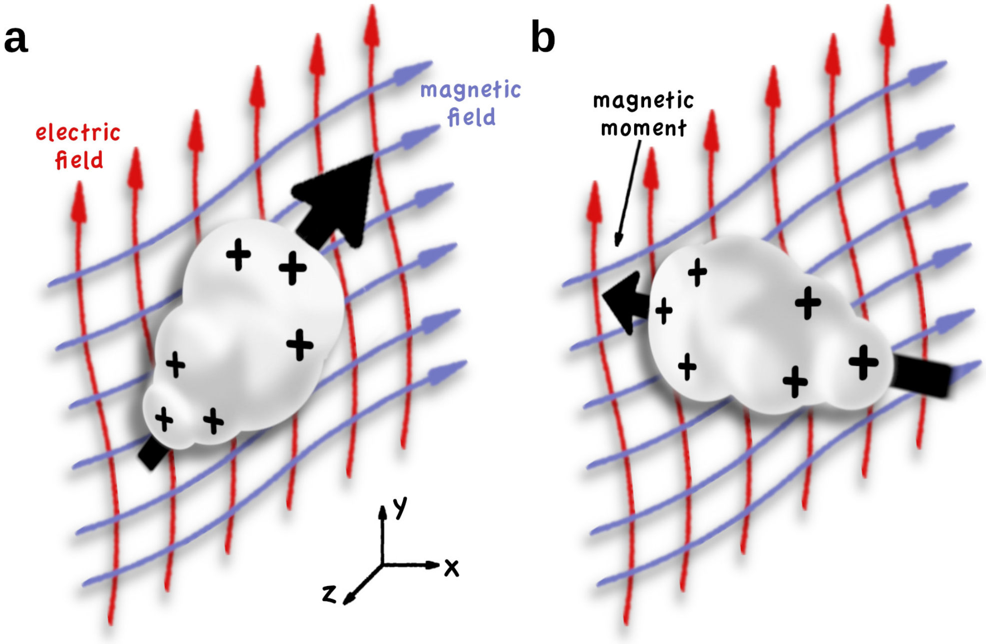

Figure 3.2: Interaction of the nucleus in the magnetic (blue) and electric (red) fields. Nucleus behaves as an irregular or "bumpy" magnet. The energy of the nucleus is dependent upon its orientation, (a) and (b), and the distribution of its electric charges (+) relative to the fields. Legend: magnetic field lines: blue; electric field lines: red; nucleus electric charges: +, magnetic moment: large black arrow.

3.4.1 Electrical Quadrupole Coupling

The electric quadrupole interaction is governed by two factors for spins $I > 1/2$ – the *quadrupole moment of the nucleus* and the *electric field gradient* created by the molecular orientation of the nucleus. The former, hereafter referred to as Q is a property of the nucleus, and a few examples are listed in table 3.1.

However, also important is the effect of the molecular properties of the nuclei – molecules with a symmetric nuclear environment, like ^{7}Li and ^{27}Al, have small local electric field gradients. Conversely, those with a small quadrupole moment like ^{14}N may have a large quadrupole interaction due to large local field gradients from covalent bonds. For ^{23}Na, these effects depend on the orientation and, when not readily mobile, the electrostatic interaction of the sodium with polar molecules in question.

Nucleus	Spin	Gyromagnetic Ratio (MHz/T)	Electric Quadrupole Moment ($\times 10^{-31}\ m^2$)
^{7}Li	3/2	16.546	-40.1
^{14}N	1	3.077	20.44
^{23}Na	3/2	11.262	104
^{27}Al	5/2	11.103	146.6

Table 3.1: Gyromagnetic ratios and electric quadrupole moments for selected quadrupolar nuclei. Data is from [57].

We can describe the electric field gradient as a tensor operating on the nucleus as $\boldsymbol{V}$. The components of $\boldsymbol{V}$ are the second derivatives of the electric potential Ψ, and along the main diagonal these are:

$$\begin{aligned} V_{xx} &= \frac{\partial^2 \Psi}{\partial x^2} \\ V_{yy} &= \frac{\partial^2 \Psi}{\partial y^2} \\ V_{zz} &= \frac{\partial^2 \Psi}{\partial z^2}. \end{aligned}$$

$\boldsymbol{V}$ is symmetric, and the off diagonal elements are then:

$$\begin{aligned} V_{xy} = V_{yx} &= \frac{\partial^2 \Psi}{\partial x \partial y} \\ V_{xz} = V_{zx} &= \frac{\partial^2 \Psi}{\partial x \partial z} \\ V_{yz} = V_{zy} &= \frac{\partial^2 \Psi}{\partial y \partial z}. \end{aligned}$$

However, $\boldsymbol{V}$ is usually stated in terms of its principle values, which we align along the coordinate axes V_{XX}, V_{YY}, V_{ZZ}, and ordered such that $|V_{ZZ}| \geq |V_{YY}| \geq |V_{XX}|$. The value of V_{ZZ} is typically specified in terms of the field per unit charge of the electron, such that $V_{ZZ} = eq$, where $e = -1.6022 \times 10^{-19}\ C$. Note that by electromagnetic theory $\boldsymbol{V}$ is traceless [47]:

$$\mathrm{Tr}(\boldsymbol{V}) = V_{XX} + V_{YY} + V_{ZZ} = 0. \tag{3.19}$$

If we define a biaxiality component, n_Q as:

$$n_Q = \frac{V_{XX} - V_{YY}}{V_{ZZ}}, \tag{3.20}$$

we can use equation 3.19 along with our definition of the principal components of $\boldsymbol{V}$ in order to define the components in terms of n_Q:

$$\begin{aligned} V_{XX} &= -eq/2\ (1 - n_Q) \\ V_{YY} &= -eq/2\ (1 + n_Q) \\ V_{ZZ} &= eq \end{aligned}$$

$\boldsymbol{V}$ is here expressed along its principle axes – if we wish to apply it instead in some molecular orientation Φ, we can apply an appropriate 3×3 rotation matrix $\mathcal{R}$, as:

$$\boldsymbol{V}(\Phi) = \mathcal{R}(\Phi) \cdot \begin{pmatrix} V_{XX} & 0 & 0 \\ 0 & V_{YY} & 0 \\ 0 & 0 & V_{ZZ} \end{pmatrix} \cdot \mathcal{R}(\Phi)^{-1} \tag{3.21}$$

where $\mathcal{R}(\Phi)$ represents the relative orientation of the principal axes system to the molecular orientation.

Finally, we can state the quadrupolar Hamiltonian from equation 3.18 as a function of its molecular orientation in terms of both the quadrupole moment, the electrical field gradients, and the spin system $\hat{\boldsymbol{S}}$ as:

$$\widehat{\mathcal{H}}_{elec}(\Phi) = \widehat{\mathcal{H}}_Q(\Phi) = \frac{eQ}{2I(2I-1)\hbar} \cdot \hat{\boldsymbol{S}} \cdot \boldsymbol{V}(\Phi) \cdot \hat{\boldsymbol{S}} \tag{3.22}$$

where the latter term is:

$$\hat{\boldsymbol{S}} \cdot \boldsymbol{V}(\Phi) \cdot \hat{\boldsymbol{S}} = \hat{S}_x V_{xx}(\Phi) \hat{S}_x + \hat{S}_x V_{xy}(\Phi) \hat{S}_y + \hat{S}_x V_{xz}(\Phi) \hat{S}_z + \cdots + \hat{S}_z V_{zz}(\Phi) \hat{S}_z. \tag{3.23}$$

The inclusion of the molecular orientation, Φ, is essential to the understanding of how ^{23}Na NMR behaves in biological tissues, as we will examine in an upcoming section.

3.4.2 First-order Approximation of $\widehat{\mathcal{H}}_Q$

A further simplification of equation 3.22 can be made for ^{23}Na NMR. If we decompose the full quadrupolar Hamiltonian into individual components of different order effects, similar to what was done for the electric potential in equation 3.16, we have:

$$\widehat{\mathcal{H}}_Q(\Phi) = \sum_{i=0}^{n} \widehat{\mathcal{H}}_{Q,i}(\Phi) \tag{3.24}$$

where $\widehat{\mathcal{H}}_{Q,1}$ is the first-order quadrular Hamiltonian, $\widehat{\mathcal{H}}_{Q,2}$ is the second-order Hamiltonian, etc. If we make the general assumption that the quadrupolar interaction is smaller than that of the static field (i.e. $\widehat{\mathcal{H}}_Q \ll \widehat{\mathcal{H}}_{static}$) we can make a first order or *secular approximation* [47, 49] and neglect all the terms of equation 3.24 greater than the first-order, or:

$$\widehat{\mathcal{H}}_Q(\Phi) \approx \widehat{\mathcal{H}}_{Q,1}(\Phi). \tag{3.25}$$

Taking this approximation into account, we can state our first order Hamiltonian in terms of its *first-order quadrupolar coupling angular frequency*, ω_Q, as:

$$\begin{aligned} \widehat{\mathcal{H}}_{Q,1} &= \frac{\omega_Q}{2}\left(3\hat{S}_z^2 - I(I+1)\hat{1}\right), \\ \textit{with}\ \ \omega_Q &= \frac{eQ\overline{V}_{zz}}{6\hbar} \end{aligned} \tag{3.26}$$

where $\hat{1}$ is the identity matrix, and $\overline{V}_{zz}$ represents the average of the electrical field gradient $V_{zz}(\Phi)$ over all its molecular motion, or:

$$\overline{V}_{zz} = \int p(\Phi) V_{zz}(\Phi)\ d\Phi \tag{3.27}$$

where $p(\Phi)$ is the probability of a particular orientation, and $\int p(\Phi)\ d\Phi = 1$.

3.5 Properties of in vivo ^{23}Na NMR

The ^{23}Na ion in an NMR experiment is subject to both magnetic and electric field effects as per equation 3.3, and by equation 3.22 we see that the molecular orientation has a significant effect on the electrical energy operator, $\widehat{\mathcal{H}}_{elec}$. But how do these effects manifest themselves with in vivo NMR?

The answer lies in the molecular composition and environment in which the ^{23}Na is involved with, and this leads to four distinct NMR spectra, depending on the motional regimes of the molecule in question [58–60]. In the following we describe the spectra, and direct the reader to also reference figure 3.3. We also make the following approximations and assumptions:

- the ^{23}Na ions are precessing at the Larmor frequency ω_0
- the ^{23}Na ions are rotating in a single compartment with rotational time constant, τ_c
- the quadrupolar Hamiltonian can be accurately simplified to the 1st order approximation by equation 3.25
- the ^{23}Na ions are (possibly) subject to an anisotropic quadrupolar interaction, w_Q
- the ^{23}Na ions are subject to a single quantum coherence NMR experiment (i.e. a single RF pulse followed by readout) unless quantum filtering is performed

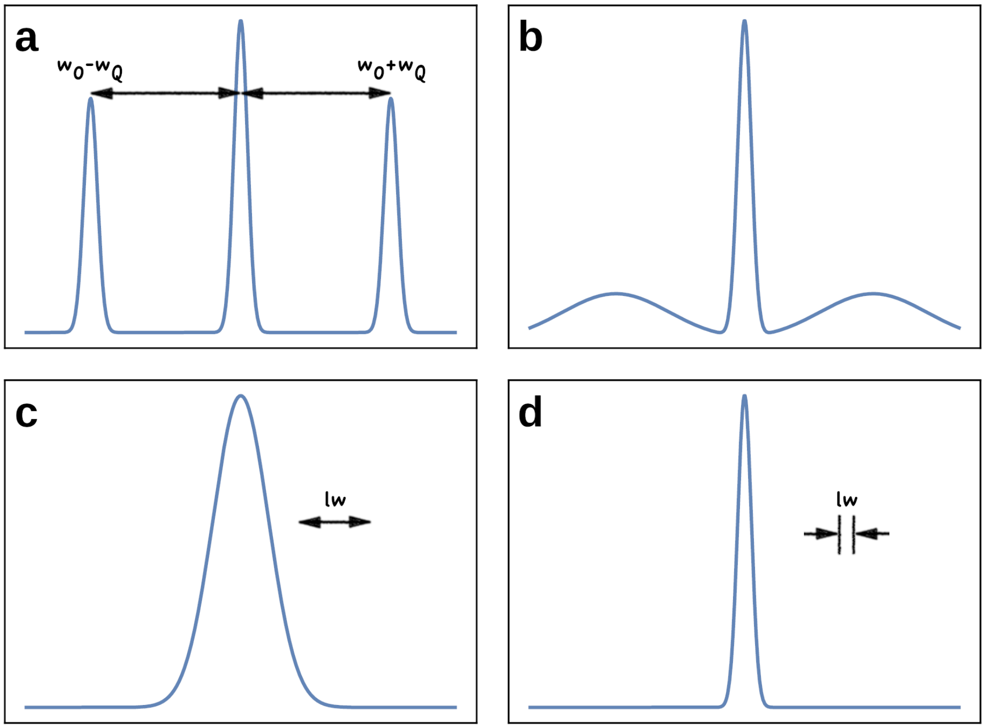

Figure 3.3: Representative NMR spectra for ${}^{23}Na$, dependent on the motional regimes based on [58–60]. (a) *type a* anisotropic 'crystal-like' spectra, characterized by a central peak, with the satellite transition at $\pm\omega_Q$. Relative intensity in the lines is 3:4:3. (b) *type b* anisotropic 'powder-like' spectrum, with central transition and inhomogeneous satellite resonances. In this example, these satellite transitions coalesce into very broad peaks. (c) *type c* isotropic slow to intermediate motion. Quadrupolar interactions act to produce dynamic shifts in the Larmor frequency – but these shifts are small and difficult to detect. The result is a broadening of the central transition, into a 'super-Lorentzian' peak shape centered at ω_0. Broad linewidth (lw) indicated. (d) *type d* fast isotropic motion where all orientations of the nuclei are equally likely and $\overline{V}_{zz} = 0$. This results in no net quadrupolar interaction. All transitions are separated by ω_0 resulting in a single NMR spectra. Longitudinal and transverse relaxation are single exponentials. Linewidth is narrow compared to *type c*. Legend: lw: linewidth.

3.5.1 Rapid Isotropic Motion

In these substances with rapid isotropic motion (i.e. liquids), all orientations of the molecule are equally possible, and this system has very rapid motion such that $\omega_0 \tau_c \ll 1$. Thus all probabilities of the orientation, $p(\Phi)$ in equation 3.27, are equal. Moreover, given the NMR experimental timescale, the average electric field gradient, $\overline{V}_{zz}$ is 0, making ω_Q in equation 3.26 also 0, so there is no residual quadrupolar interaction. The four energy levels of the spin states of ^{23}Na are separated by ω_0, and the NMR spectra is a single peak at ω_0. Longitudinal and transverse relaxation are simple exponential decays, similar to I = 1/2 systems. In terms of brain tissue, the ^{23}Na in the cerebrospinal fluid (CSF) behaves as this type, and produces a *type d* spectra as per Rooney and Springer [58] (see figure 3.3).

3.5.2 Slow to Intermediate Isotropic Motion

In these situations, the nucleus' macromolecular motion is isotropic, but of a similar order to the Larmor frequency, or $\omega_0 \tau_c \approx 1$. As such, there is a residual quadrupolar interaction, which depends upon the orientation of the nucleus in the electric and magnetic fields (figure 3.2). These interactions result in the satellite transitions having different relaxation rates from those of the central transition, and produce a dynamic shift in the Larmor frequency. However, these shifts are smaller than the linewidths, and are thus extremely difficult to detect. Their net effect upon the NMR spectra is to produce a broadening of the homogeneous peak. This bi-exponential, "super-Lorentzian" peak, a *type c* spectra, describes the behavior of WM and grey matter (GM) in the brain.

3.5.3 Anisotropic Motion

For *types b* and *a*, $\omega_0\tau_c > 1$, all possible orientations of the nucleus are *not* likely. For *type b*, the sample is inhomogeneous, with multiple quadrupolar couplings – or 'powder-like' as classified by Rooney [58]. This results in a homogeneous central resonance superimposed with inhomogeneous satellite resonances. A *type a* spectrum would be found in solid or semi-solid samples (i.e. 'crystal-like'), and its spectrum characterized by a single peak at ω_0, with the two satellite transitions represented by peaks at $\pm\overline{\omega_Q}$. The relative intensity in spec tral peaks is 3:4:3. Both anisotropic types can be observed with NMR methods, but neither are very relevant for in vivo tissue, and any further discussion is limited to *types c* and *d*.

3.6 ^{23}Na Considerations for Brain MRI

In the previous sections we have seen how the quantum properties of ^{23}Na determine its motional regimes, and how those motional regimes manifest themselves in the NMR spectra of ^{23}Na. What we outline in this section is how these NMR properties influence how we use MRI to image in vivo ^{23}Na – specifically, in vivo brain imaging.

After the application of an RF pulse at the Larmor frequency, the signal equation of the MRI experiment is proportional to the voltage in the receiver coil [61]:

$$S(t) = \gamma B_0 \Omega \int_V M_T(\boldsymbol{r}, t) \mathcal{B}_T(\boldsymbol{r}) \ d^3\boldsymbol{r} \tag{3.28}$$

where γB_0 is the Larmor frequency, Ω is a constant representing the gain from the receiver coil electronics, $M_T = M_x + iM_y$ is the transverse magnetization, $\mathcal{B}_T = \mathcal{B}_x + i\mathcal{B}_y$ the receive field in the coil, with $\boldsymbol{r} = (r_x, r_y, r_z)$ and t representing the spatial location and time respectively.

We can separate the transverse magnetization into sub-components, based on the Larmor frequency and a signal decay constant, T_2^*, as:

$$M_T(\boldsymbol{r}, t) = e^{-i(\gamma B_0 t - \phi_0)} e^{-t/T_2^*(\boldsymbol{r})} M_T(\boldsymbol{r}, 0) \tag{3.29}$$

The component introduced by the Larmor frequency is represented by $e^{-i(\gamma B_0 t - \phi_0)}$ with the ϕ_0 term representing the initial signal phase (usually assumed to be 0). The decay constant, T_2^* is spatially dependent, and is partly due to composition of the object under examination. We will examine the T_2^* component further below.

Equation 3.28 is linearly dependent on γ, and as

$$\gamma_{^{23}Na}/\gamma_{^1H} = \frac{11.262 \times 2\pi}{42.577 \times 2\pi} \approx 0.26, \tag{3.30}$$

we can expect the ^{23}Na signal to be attenuated by the same factor, other components being equal.

Three tissues are visible in MRI of the brain – CSF, WM, and GM. For ^{23}Na, CSF is a *type d* NMR spectra, while WM and GM are both *type c* (see Figure 3.3). Thus, GM and WM both have multiple transverse relaxation rates, representing the relaxation times from the satellite and central transitions respectively. The satellite transitions have a higher relaxivity than the central transition, and are so noted as T_{2f}^{*} (T_2^* 'fast') versus T_{2s}^{*} (T_2^* 'slow'). Table 3.2 indicates typical ^{23}Na and ^{1}H relaxation components for brain tissue at 3 T [62–66]. Comparison of the T_2^* components indicate the relatively rapid transverse decay of the ^{23}Na signal compared to ^{1}H MRI.

Nucleus	Tissue	T_1	T_2	T_{2f}^*	T_{2s}^*
^{23}Na	WM	15-25	–	0.8-3	15-30
	GM	15-25	–	0.8-3	15-30
	CSF	50-60	50-55	–	–
^{1}H	WM	1039-1120	52-60	–	–
	GM	1420-1520	61-81	–	–
	CSF	4400	2200	–	–

Table 3.2: Comparative relaxation times of brain tissue for ^{23}Na and ^{1}H at 3 T. All times are in ms. Values are from [62–66].

As a result of their multiple relaxation components, GM and WM display a biexponential decay. The satellite spins in the $I = 3/2$ system contain approximately 60% of the signal immediately after the application of the RF pulse. The importance of this is that 60% of the total transverse signal decays rapidly at the T_{2f}^* time constant. We can describe this signal dependence to its satellite and central transitions as:

$$S(t) \propto 0.6e^{-TE/T_{2f}^*} + 0.4e^{-TE/T_{2s}^*} \tag{3.31}$$

where TE is the echo time. The rapid decay T_{2f}^* component in 3.31 necessitates the use of ultra-short TE (UTE) pulse sequences. This will be discussed further in a later section.

One further difficulty in sodium MRI in the brain is the scarcity of ^{23}Na relative to ^{1}H. In ^{1}H MRI brain abundance of ^{1}H is approximately 88 M. A comparison of this to brain ^{23}Na “dense” tissue, such as CSF, where the concentration is only $0.14-0.16$ M, easily shows the difficulty; this represents a decrease in available signal of ≈ 600. If the interested tissue is either WM or GM, the difficulties are only exasperated.

A simple model of an imaging voxel in a ^{23}Na MRI experiment will encompass three different tissue volumes [63] – intracellular, extracellular, and a “solid” volume representing the cell membranes, proteins, etc. (see figure 2.1). We can denote these volume compartments as V_i, V_e, and V_s for intra-, extracellular and solid respectively. Their relative volumes have been found to vary depending on whether we are measuring WM or GM, but have been found to be $V_i = 0.5 - 0.6$, $V_e = 0.18 - 0.22$, and $V_s = 0.15 - 0.3$ [63, 67, 68].

The sodium concentration of the solid volume is negligible, and further, its T_2 would be even shorter than in the extra- or intracellular ^{23}Na compartments, making it almost impossible to image in vivo. This leads to the conclusion that in an imaging voxel the observable TSC is a weighted average of the relative volumes of each tissue compartment and the sodium concentrations therein, or:

$$TSC = V_i[Na]_i + V_e[Na]_e + \cancel{V_s(0)} \tag{3.32}$$

Using the above assumptions, Madelin et al. [63] found that the expected WM $[Na]_i \approx 10.6 \pm 5.3$, and GM $[Na]_i \approx 11.7 \pm 5.9$, with the measured TSC between 30 and 40 mM. This means that in the WM and GM tissues, which are typically more interesting in terms of disease states, we can expect a decrease in signal of ≈ 2500, based purely on the relative concentrations of ^{23}Na and ^{1}H in the brain.

In conclusion we can summarize the difficulties for ^{23}Na MRI compared with ^{1}H MRI for neuroimaging applications with the following:

- reduced gyromagnetic ratio leads to a reduced signal in the receiver coils (factor of ≈ 4)
- rapid T_2^* decay necessitates the use of fast acquisitions and UTE pulse sequences
- in WM and GM, the T_{2f}^* component of the signal disappears within a few milliseconds – this represents 60% of the available signal
- low apparent TSC compared with ^{1}H concentration in the brain repre-

sents a reduction in signal by ≈ 2500

The above limitations lead to long acquisition times for ^{23}Na MRI, as multiple averages are required in order to produce a reasonable signal. Averaging is typically combined with coarse resolutions in order to increase the signal to noise ratio (SNR) in the resulting images.

3.7 Extracellular versus Intracellular ^{23}Na

Instead of measuring the TSC and attempting to tease out the contributions in the total signal from the $[Na]_e$ and $[Na]_i$, efforts have been made to image the contributions from these two compartments separately using (i) multiple quantum coherences of the spin 3/2 system, (ii) shift reagents, and (iii) contrast agents. We will briefly outline these efforts here.

3.7.1 Multiple Quantum Coherences

Thus far, this dissertation has been primarily focused on SQC – transitions that are either satellite ($\frac{\pm 3}{2} \rightleftharpoons \frac{\pm 1}{2}$) or central ($\frac{-1}{2} \rightleftharpoons \frac{1}{2}$) (see figure 3.1). However, it should be noted that double and triple quantum coherences (DQC and TQC) exist, which evolve as a result of the interaction of the quadrupole charge distribution interacting with the gradient of the electric field [49]. These coherences represent transitions from $\frac{3}{2} \rightleftharpoons \frac{-1}{2}$ or $\frac{-3}{2} \rightleftharpoons \frac{1}{2}$ for DQC, or $\frac{-3}{2} \rightleftharpoons \frac{3}{2}$ for TQC as in figure 3.1. These coherences can be detected with judicious use of preparatory RF pulses before the acquisition readout in MQC pulse sequences [53,69,70]. MQCs have attracted attention previously because of reports that these can selectively attain the signal of

$[Na]_i$ [52, 70–72]; however, this is still an open question scientifically, because considerable evidence exists that the signal from the $[Na]_e$ contributes to MQC experiments [73–75]. In addition, DQC and TQC imaging has been reported to be approximately 10% of the signal obtained by a SQC experiment [49]. As such, even if they could definitively capture the signal from only the intracellular compartment, the signal loss is potentially prohibitive for in vivo imaging, especially at 3T.

3.7.2 Shift Reagents

The signal contribution from the extracellular space has been suppressed by the use of shift reagents [75, 76]. These shift reagent molecules are too large to cross the cell membrane and thus remain in the extracellular space. By shifting the Larmor frequency, shift reagents allow the extracellular spins to be separated from their intracellular counterparts – this allows the $[Na]_i$ to be imaged by a selective RF pulse. These reagents may shift the frequency either downfield (i.e. higher frequency) as in the cases of thulium-1,4,7,10-tetraazacyclododecane 1,4,7,10-tetrakis (methylene phosphonate) (TmDOTP^{5-}) [77] and dysprosium triethylenetetraminehexaacetate ($\mathrm{Dy[TTHA]}^{3-}$) [78]; or upfield as for bis(tripolyphosphate) dysprosium(III) $\mathrm{Dy(PPP}_i)_2^{7-}$ [79]. However, as these reagents are somewhat toxic [80, 81], their use for in vivo imaging is contraindicated.

3.7.3 Contrast Agents

Both Kohler [80] and Winkler [82] mention the potential use of the contrast agent dextran magnetite, which like the previously mentioned shift reagents stays in the extracellular space; however, it shortens the T_2^* of the extracellular ^{23}Na instead of shifting the Larmor frequency. Kohler postulated that sufficient concentration of the contrast agent could potentially suppress the $[Na]_e$ altogether; however, despite early efforts into their use in preclinical imaging [83, 84], there is scant evidence in the literature regarding its applicability for human ^{23}Na MRI.

Chapter 4

Acquisition and Reconstruction

4.1 MRI coils

An RF coil is a necessary hardware component for any NMR experiment. As per equation 3.28, we wish to maximize the the signal by having a large gain constant, Ω. The most common type of coil is a cylindrical "bird-cage" design, as described by Watkins and Fukushima [85]. The MRI coil has two essential purposes – RF transmission, also known as B_1^+ field, and the receiver, or B_1^- field.

In clinical ^1H MRI (i.e. most often 1.5 and 3 T superconducting magnets), typically the B_1^+ field is generated by the magnet's body coil, with an anatomy specific coil used solely for the B_1^- field. However, in non-proton MRI it is common to use a coil which acts both as a transmit and receive coil. figure 4.1 is an example of a ^{23}Na bird-cage coil, and furthermore is the coil used in the experiments detailed in the remainder of this dissertation. This design has 16 rungs, with the outer diameter measuring 320 mm, inner diameter 240 mm, with a total length of 245 mm along a direction parallel to the rungs.

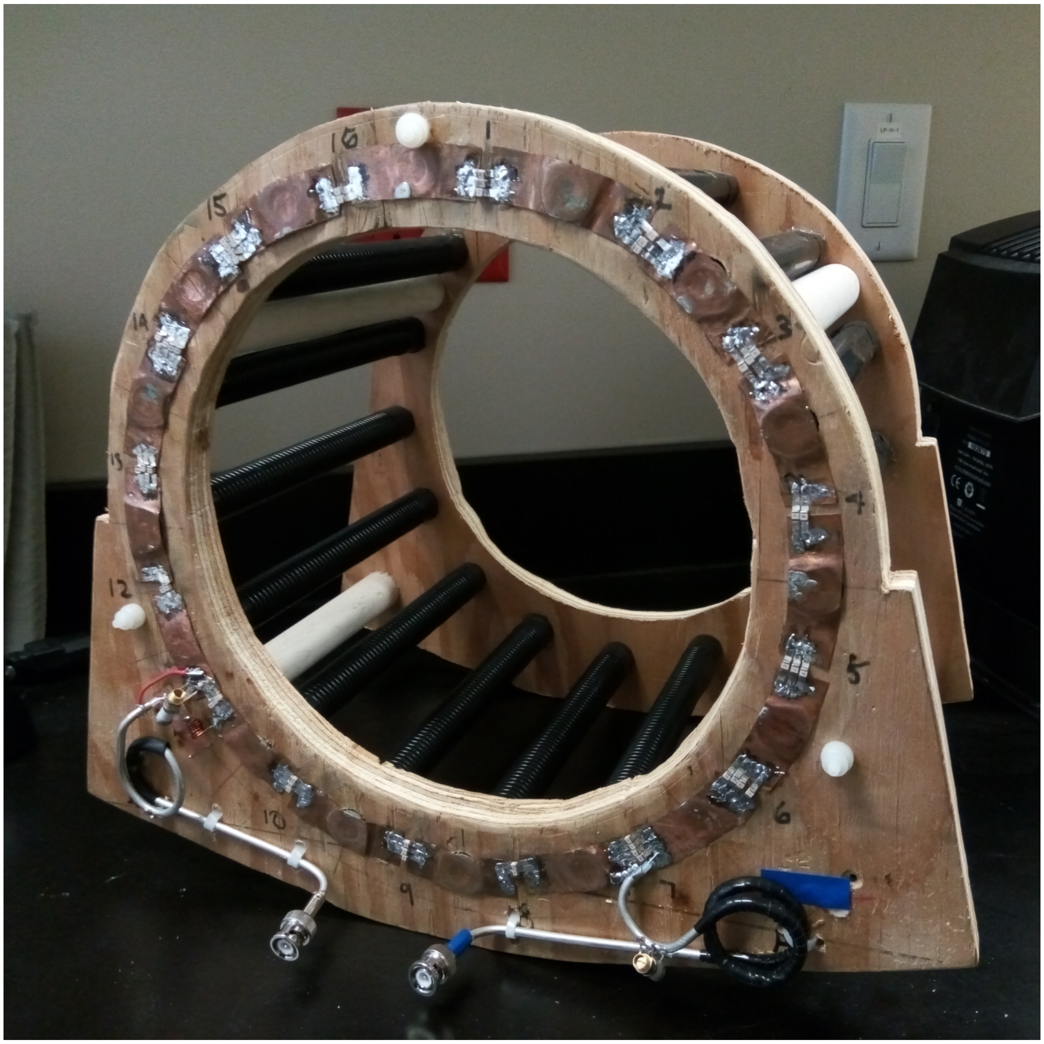

Figure 4.1: A single-channel, single-tune, transmit and receive quadrature bird-cage RF coil. This coil is tuned to 33.8 MHz, the Larmor frequency for ^{23}Na at 3 T. Its inner diameter is designed to contain an imaging field of view (FOV) of 240 mm, typically large enough for an adult human head. This is the coil which was used in the experiments detailed in the rest of this manuscript.

Ideally, the B_1^+ field is perfectly homogeneous and results in a completely uniform flip angle across the imaging field of view (FOV). In practice, perturbations exist creating a non-uniform flip angle in the FOV. Measuring and adjusting for the B_1^+ field is important for quantitative MRI, and is essential when using custom-build RF coils. Measuring and correcting for the B_1^+ field is called B_1^+ *field mapping* and B_1^+ *field map correction.*

4.2 Gradients and Spatial Encoding

The signal $S(t)$ from equation 3.28 in an NMR experiment is called the free induction decay (FID) and it is spatially independent. In effect, it is the signal from *all* of the spins in the object under consideration. In order to produce an image, we need a method to determine the spatial location of the spins, and thus derive the spin density, dependent on that location. Using equations 3.28 and 3.29, we can rewrite the signal equation as:

$$S(t) = \int_V \gamma B_0 \Omega M_T(\boldsymbol{r}, 0) B_1^-(\boldsymbol{r}) e^{-i\gamma B_0 t} e^{-t/T_2^*(\boldsymbol{r})} \; d^3\boldsymbol{r} \tag{4.1}$$

where the initial phase is 0. The other terms are the Larmor frequency γB_0, receiver coil gain Ω, transverse magnetization M_T, receiver field B_1^-, with $\boldsymbol{r}$ the spatial location and t is time.

In general, the receiver field is spatially dependent – however, in the interest of simplifying the following derivation of spatial encoding, we will assume that B_1^- is invariant with respect to position, and can be represented as a constant:

$$B_1^-(\boldsymbol{r}) \approx B_1^-. \tag{4.2}$$

If we group all of the constants together as a single factor, $A = \gamma B_0 \Omega B_1^-$, then:

$$S(t) = \int_V A M_T(\boldsymbol{r}, 0) e^{-i\gamma B_0 t} e^{-t/T_2^*(\boldsymbol{r})}\ d^3\boldsymbol{r} \tag{4.3}$$

and since the Larmor frequency term is not dependent on position,

$$S(t) = e^{-i\gamma B_0 t} \int_V A M_T(\boldsymbol{r}, 0) e^{-t/T_2^*(\boldsymbol{r})}\ d^3\boldsymbol{r}. \tag{4.4}$$

The term under the integration is the *effective spin density* of the experiment, which we define as:

$$\rho(\boldsymbol{r}) = A M_T(\boldsymbol{r}, 0) e^{-t/T_2^*(\boldsymbol{r})}. \tag{4.5}$$

In order to add spatial encoding to our signal we apply linear magnetic field gradients. These perturb the Larmor frequency experienced by the spins in a deterministic way based on the spin's position, and thus spatially encode the received signal. Mathematically, let us add gradient fields for each spatial component and apply these across the object. The effective magnetic field is then

$$B(\boldsymbol{r}) = B_0 + \boldsymbol{G}(\boldsymbol{r}) \cdot \boldsymbol{r}, \tag{4.6}$$

where $\boldsymbol{G}(\boldsymbol{r}) = (G_{r_x}, G_{r_y}, G_{r_z})$. Equation 4.6 indicates that the Larmor frequency experienced by the spins is now spatially dependent on $\boldsymbol{r}$. Note that the gradients can also vary in time, i.e. $\boldsymbol{G}(\boldsymbol{r}, t)$ – but for simplicity we will assume constant gradients for the following derivations. If we use equation 4.6

in place of the static field B_0 in 4.3, we have:

$$\begin{aligned} S(t) &= \int_V AM_T(\boldsymbol{r},0)e^{-i\gamma(B_0+\boldsymbol{G}(\boldsymbol{r})\cdot\boldsymbol{r})t}e^{-t/T_2^*(\boldsymbol{r})}\ d^3\boldsymbol{r} \\ &= \int_V AM_T(\boldsymbol{r},0)e^{-i\gamma B_0 t}e^{-i\gamma(\boldsymbol{G}(\boldsymbol{r})\cdot\boldsymbol{r})t}e^{-t/T_2^*(\boldsymbol{r})}\ d^3\boldsymbol{r} \\ &= e^{-i\gamma B_0 t}\int_V \rho(\boldsymbol{r})e^{-i\gamma(\boldsymbol{G}(\boldsymbol{r})\cdot\boldsymbol{r})t}\ d^3\boldsymbol{r} \end{aligned} \tag{4.7}$$

The NMR signal is demodulated by the Larmor frequency as part of the processing in the receiver chain, so that the baseband signal becomes

$$S_b(t) = e^{i\gamma B_0 t}S(t) = \int_V \rho(\boldsymbol{r})e^{-i\gamma(\boldsymbol{G}(\boldsymbol{r})\cdot\boldsymbol{r})t}\ d^3\boldsymbol{r}. \tag{4.8}$$

Now split the volumetric integral and spatial vectors into their separate components:

$$S_b(t) = \int_{-\infty}^{\infty}\int_{-\infty}^{\infty}\int_{-\infty}^{\infty} \rho(\boldsymbol{r})e^{-i\gamma G_{r_x} r_x t}e^{-i\gamma G_{r_y} r_y t}e^{-i\gamma G_{r_z} r_z t}\ dr_z\, dr_y\, dr_x. \tag{4.9}$$

Define a set of variables, $\boldsymbol{k}(t)$ such that:

$$\begin{aligned} \boldsymbol{k}(t) &= (\gamma G_{r_x} t, \gamma G_{r_y} t, \gamma G_{r_z} t) \\ &= (k_{r_x}, k_{r_y}, k_{r_z}), \end{aligned} \tag{4.10}$$

and substitute these back into equation 4.9 so that:

$$S_b(t) = \int_{-\infty}^{\infty}\int_{-\infty}^{\infty}\int_{-\infty}^{\infty} \rho(\boldsymbol{r})e^{-ik_{r_x} r_x}e^{-ik_{r_y} r_y}e^{-ik_{r_z} r_z}\ dr_z\, dr_y\, dr_x. \tag{4.11}$$

Recognize that equation 4.11 forms a multidimensional Fourier Transform pair between the baseband signal, $S_b(t)$, in time and the effective spin density $\rho(\boldsymbol{r})$ in space, so that

$$\begin{aligned} S_b(t) &= \mathcal{F}\left[\rho(\boldsymbol{r})\right] \\ \rho(\boldsymbol{r}) &= \mathcal{F}^{-1}\left[S_b(t)\right], \end{aligned} \tag{4.12}$$

where $\mathcal{F}$ and $\mathcal{F}^{-1}$ represent the Fourier and inverse Fourier Transforms respectively. In effect, what equation 4.12 is telling is that in our MRI experiment our image can be determined by the inverse Fourier Transform of our spatially encoded image, and in order to spatially encode our signal we apply linear magnetic field gradients during the acquisition.

Before moving on to the next section, let us examine equation 4.10 a little more. $\boldsymbol{k}(t)$ represents the range of *spatial frequencies* for each coordinate. Over an entire MRI experiment, this represents our total range of spatial frequencies sampled, or our *k-space*, which is a critical concept to understanding strategies of MRI acquisition. We will examine this concept more closely in the content of ^{23}Na MRI in the next section.

Note also that equation 4.10 only represents the specific case where we have constant gradients. In general, spatial frequencies and the gradient field are related by:

$$\boldsymbol{k}(t) = \gamma \int_0^t \boldsymbol{G}(t')\ dt' \tag{4.13}$$

4.3 Pulse Sequences for ^{23}Na MRI

From table 3.2 and our previous discussions, the T_{2f}^* signal disappears rapidly for *type c* tissues (i.e. WM and GM). Moreover, T_{2f}^* component represent $\approx$

60% of the available signal (equation 3.31). It is thus imperative to capture the MRI signal as soon as possible after application of the RF pulse, as this signal will rapidly decay into the background noise. In addition, it is important to capture the low spatial frequencies in this limited time window, as these spatial frequencies represent most of the available k-space signal and determine overall image contrast. The usual MRI convention is to arrange k-space in a 3D grid, with the low spatial frequencies (i.e. at or near 0) in the middle or center of k-space, with the "outer" frequencies arranged distally (positive or negative) away from the center. These exterior spatial frequencies have less energy than the central frequencies, and contain details about the edges in the image. For further discussions of k-space and image properties consult [61, 86–88].

The echo time (TE) of an MRI sequence is the time between the center of the RF pulse (for non-adiabatic pulses) and the center of the k-space sampling window. Pulse sequences that sample the center of k-space soon after the application of the RF pulse are termed ultra-short echo time (UTE) pulse sequences, as they begin their acquisitions soon after the end of the RF pulse ($\approx$ 1 ms or less) and sample the center of k-space first. Two common acquisition strategies in common use for ^{23}Na MRI are density adapted, 3D projection reconstruction (DA-3DPR) [89] and Fermat looped orthogonally encoded trajectories (FLORET) [90].

4.3.1 DA-3DPR

3D Projection Reconstruction (3DPR), also known as 3D Radial Projection, is a technique which has been used previously to study ^{23}Na with MRI [91,92].

In this UTE technique, the T_{2f}^{*} component of ^{23}Na is captured by beginning the acquisition at the center of k-space. The difference between this and the DA-3DPR is the spacing of the k-space sampling points – while the former technique has equidistant samples, DA-3DPR has a sparse sampling density near the center of k-space, and denser in the exterior of k-space. The gradient for the DA-3DPR technique uses a ramp and trapezoidal portion like the 3DPR – however, it then decays at a rate of $\propto t^{-2/3}$ in order to sample k-space progressively denser (see figure 4.2). Nagel et al. found that this acquisition provided an approximate increase of 40% signal in brain tissue compared to a 3DPR technique, with less blurring for longer readout windows [89].

4.3.2 FLORET

Fermat looped, orthogonally encoded trajectories (FLORET) is a center-out trajectory design based on a single Fermat spiral. Each spiral plays out in a single repetition time (TR), and multiple trajectories are stacked with each other in a conical fashion to produce a "hub" along a single axis. Multiple hubs can be created orthogonal to each other in order to sample k-space uniformly (see figure 4.3). Pipe et al. [90] found FLORET to have a superior performance over comparable trajectory designs such as stack of cones or spirals, and when FLORET is undersampled, it leads to incoherent aliasing. Because FLORET samples k-space more efficiently than DA-3DPR, multiple signal averages can be used with the former in order to bring the acquisition times (TA) approximately equal. This ensures a "fair" comparison with regards to acquisition time.

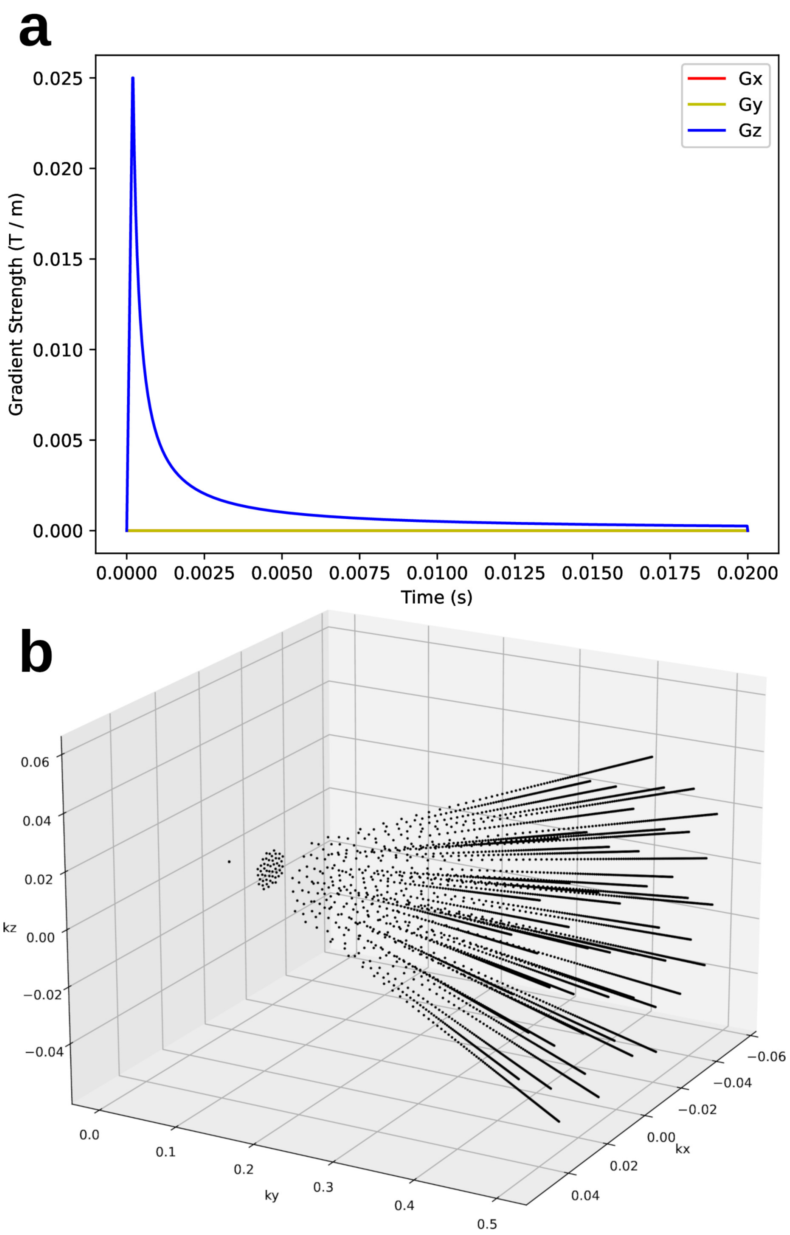

Figure 4.2: DA-3DPR acquisition. (a) Plot of magnetic field gradients (G_x, G_y, G_z) versus time for a single spoke. Gradients decay towards 0 with time. (b) Plot of 50 trajectories for a DA-3DPR acquisition in 3D k-space coordinates. Every dot represents a sampling point – for visualization purposes only every 10th point is pictured.

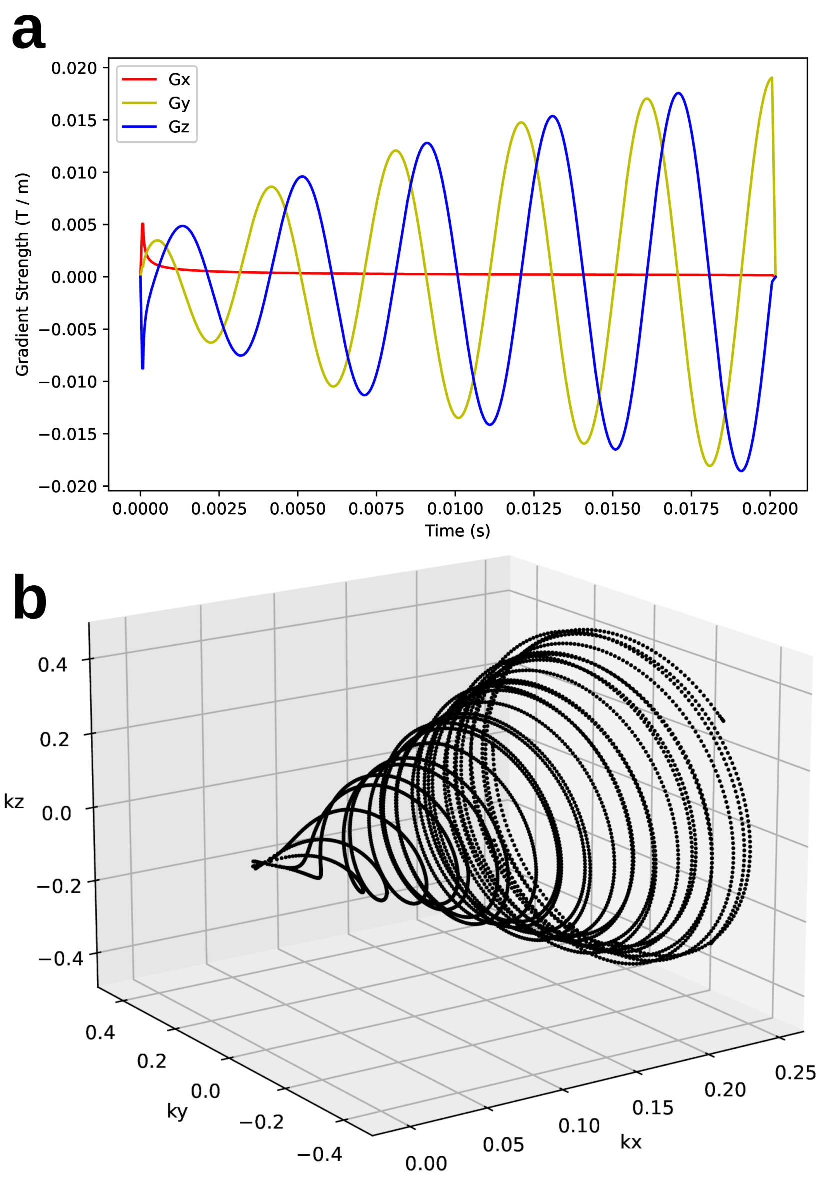

Figure 4.3: FLORET acquisition. (a) Plot of magnetic field gradients (G_x, G_y, G_z) versus time for a single trajectory. (b) 5 FLORET trajectories in 3D k-space. Each dot represents a k-space sampling point. Some sampling points omitted for visualization purposes. FLORET samples k-space more efficiently than DA-3DPR – this places greater demands on the gradient hardware than DA-3DPR as evidenced by higher absolute slew rates.

4.4 Reconstruction

As per equation 4.12 we obtain an image in MRI from the application of the inverse Fourier transform. In practice, most MRI k-space data are sampled on a Cartesian grid, making image reconstruction relatively straightforward by the application of the fast Fourier transform (FFT) directly. However, for the UTE acquisitions we have discussed previously this is problematic, since the data are *not* arranged on a grid, and are non-Cartesian acquisitions.

In order to reconstruct the imaging data the usual process is to apply a non-uniform fast Fourier transform (NUFFT) to the data. This is achieved by "gridding" the data first by convolution with a kernel, and then applying an inverse FFT.

If our k-space acquisition data is $s(\boldsymbol{k})$, where $\boldsymbol{k} = (k_{r_x}, k_{r_y}, k_{r_z})$ is our position in k-space, we can write our gridding data, $s_c(\boldsymbol{k})$, as:

$$s_c(\boldsymbol{k}) = ((s(\boldsymbol{k}) \cdot w(\boldsymbol{k})) * C(\boldsymbol{k})) \cdot g(\boldsymbol{k}) *^{-1} C(\boldsymbol{k}), \tag{4.14}$$

where $w(\boldsymbol{k})$ is our density compensation function (DCF), $C(\boldsymbol{k})$ is our convolution kernel, $g(\boldsymbol{k})$ is a function which defines our Cartesian grid, and $*^{-1}$ is the inverse convolution function [86]. The DCF factor is important to remove the effect of non-uniform sampling – this is typically expressed as a series of "weights" to the k-space data. The DCF can be obtained analytically from the acquisition trajectories (i.e. for DA-3DPR), iteratively [93], or geometrically [94].

The inverse convolution operator is awkward to evaluate, and thus the usual method is to apply this *deapodization* term in image space –

$$\begin{aligned}\rho(\boldsymbol{r}) &= \mathcal{F}^{-1}[s_c(\boldsymbol{k})] \\ &= \mathcal{F}^{-1}[((s(\boldsymbol{k}) \cdot w(\boldsymbol{k})) * C(\boldsymbol{k})) \cdot g(\boldsymbol{k})] \cdot \frac{1}{c(\boldsymbol{r})}, \end{aligned} \tag{4.15}$$

where $C(\boldsymbol{k}) = \mathcal{F}[c(\boldsymbol{r})]$ form a Fourier transform pair.

4.5 Point-Spread Function

Quantifying imaging performance is an essential task in evaluating any imaging system. In particular, the point-spread function (PSF) is a measure of the imaging performance in terms of the broadening of image structures. The PSF incorporates the cumulative effects of our scanning hardware, acquisition window, reconstruction technique, etc., and can be thought of as degrading our image quality. Qualitatively, an imaging system with a better PSF will produce images with less degradation. Mathematically, we can express the PSF as:

$$\begin{aligned}\hat{\rho}(\boldsymbol{r}) &= \mathcal{F}^{-1}[s(\boldsymbol{k})H(\boldsymbol{k})] \\ &= \rho(\boldsymbol{r}) * h(\boldsymbol{r}), \end{aligned} \tag{4.16}$$

where the resulting degraded image is $\hat{\rho}(\boldsymbol{r})$, and the PSF is expressed as $h(\boldsymbol{r})$. What the above is saying our ideal image, $\rho(\boldsymbol{r})$, is distorted by our PSF which results in our image, $\hat{\rho}(\boldsymbol{r})$, with lessened quality. The ideal PSF is a delta function such that $\hat{\rho}(\boldsymbol{r}) = \rho(\boldsymbol{r})$ – as this is practically impossible, we would like to measure how close our imaging PSF is to this theoretical ideal.

The PSF is our measure in image space, and its Fourier transform pair, $H(\boldsymbol{k})$, is called the modulation transfer function (MTF). Whereas the PSF can measure the broadening of structures in image space, the MTF captures information relating to the spatial frequencies and maximum resolution of the imaging system. If the PSF is the ideal delta function, the MTF will be a horizontal line at unity (i.e. all imaging structures, regardless of how small, are perfectly resolvable).

For a given PSF, we are usually interested in the full width at half maximum (FWHM) – that is, the width of the PSF at the height of half of the maximum value. This value represents the smallest resolution that can be discerned in the image, or, the minimum distance two structures need to be separated by in order to be visible as separate in the image. Smaller FWHM values represent a narrower PSF and thus a superior imaging system.

4.5.1 Measuring the PSF

In principle, measuring the PSF in straightforward – construct a phantom with a delta function structure, place this in the MRI scanner, and the resulting image will be the PSF. In practice, constructing a phantom like this is impractical. In lieu of this, it is generally more practical to measure the MTF at different spatial frequencies, interpolate this function, and then convert to the PSF via the Fourier transform (i.e. $PSF = \mathcal{F}^{-1}[MTF]$.

For a given frequency, f, the MTF can be calculated as:

$$MTF_f = \frac{I_{max,f} - I_{min,f}}{I_{max,f} + I_{min,f}}, \tag{4.17}$$

where $I_{max,f}$ and $I_{min,f}$ represent the maximum and minimum image intensities respectively at a particular spatial frequency. Practically, this can be measured by constructing a phantom with "combs" or alternating patterns of positive and negative signals at different frequencies. Within each comb, the "teeth" will be separated by some known distance (i.e. 5 mm, 2 mm, etc.) – the inverse of this distance will be our spatial frequency, f.

Chapter 5

Objectives and Hypotheses

The physiological and biological aspects of ^{23}Na and its relation to brain health and pathologies were outlined in a previous chapter. The main purpose of this thesis was to develop a ^{23}Na magnetic resonance imaging (MRI) apparatus in order to measure tissue sodium concentration (TSC) in the brain. Underlining this were these major objectives:

1. Build, tune, and match a radiofrequency (RF) head coil compatible with a clinical General Electric Healthcare 3 T MRI.
2. Develop an MRI pulse sequence which can capture and spatially encode the ^{23}Na signal from an MRI experiment.
3. Implement an image reconstruction pipeline for ^{23}Na.
4. Design and build a resolution phantom to allow quantification of imaging system performance.
5. Generate a TSC imaging procedure which balances the low signal of

^{23}Na MRI with acquisition times which are clinically viable.

These objectives support the following hypotheses for this dissertation:

- ^{23}Na MRI is fundamentally signal limited – as a result, imaging performance is not necessarily governed by acquisition strategy. In particular, the choice between two common UTE sequences, DA-3DPR and FLORET, matters less than the overall acquisition time. Examining the performance and image metrics from both acquisition types will be used to test this hypothesis.

- Measurement of the point-spread function (PSF) in the resolution phantom can be adversely affected by noise. This will be demonstrated by phantom experiments with different expected SNR, and PSFs determined by two methodologies.

- The combination of ^{23}Na MRI and ^{1}H DTI can provide useful complementary information for in vivo brain imaging, despite (potentially) broad PSFs with both techniques. DTI can provide information regarding the structure of brain tissue, particularly regarding WM axonal integrity. ^{23}Na can potentially provide metabolic information and the cellular health of the $Na^{+}K^{+}-ATPase$.

Expanding on the last hypothesis, there are few papers which examine the role of ^{23}Na MRI and diffusion imaging. The combination of diffusion weighted imaging has been used in breast cancer [95,96], MS [12], and uterine fibroids [97]. More recently, low resolution ^{23}Na images were combined with DTI for a study into TBI [44]; however, outside of these there is a notable "gap" in the literature regarding the use of ^{23}Na and DTI in the assessment of the healthy or diseased human brain. Combining the two techniques could add important information regarding brain health, despite the large PSF which are inherent to both types of imaging. These observations motivated the decision to combine ^{23}Na and diffusion imaging in a health cohort, with the ultimate goal of using the two methodologies to study ^{23}Na disruptions and potential diffusion correlates in brain disorders.

Chapter 6

Pilot Study: Measurement of 23Na point-spread function (PSF) in ultrashort TE (UTE) acquisitions in a 3D printed resolution phantom

Paul Polak M.A.Sc, Rolf F. Schulte Ph.D, Michael D. Noseworthy Ph.D, P.Eng

6.1 Introduction

In vivo ^{23}Na MRI is desirable due to sodium's ubiquity in human metabolism, being essential for cellular homeostasis, pH regulation, and action potentials in muscles and neurons [1, 2]. Unfortunately, ^{23}Na MRI suffers from several inherent challenges, including low gyromagnetic ratio, necessity of specialized hardware, low signal and henceforth long acquisitions due to signal averaging. Due to the rapid T_2 decay, ultrashort TE (UTE) pulse sequences are preferred, the most common of these being density-adapted 3D projection reconstruction (3DPR) [89], and Fermat looped orthogonally encoded trajectories (FLORET) [90].

This pilot study examines the PSF for sodium MRI in a 3D printed resolution phantom with both DA-3DPR and FLORET. The motivation behind this work was to demonstrate the efficacy of using a 3D printed resolution phantom to quantitatively measure PSFs. 3D printing provides a convenient and economical method to construct phantoms – this phantom was designed with a removable lid, so the contents (i.e. sodium concentration) could be easily changed and the phantom reused. The MTFs for both sequences measured with different concentrations of ^{23}Na in gelatin – the PSFs were then derived by the Fourier transform. This work directly compared DA-3DPR and FLORET acquisition strategies by examining their PSF performances.

This work was the basis for a conference proceeding that was accepted by the European Society for Magnetic Resonance in Medicine and Biology, 2020, which presented by Paul Polak.

6.2 Methods

6.2.1 Hardware

^{23}Na imaging was conducted with a GE 3T MR750 (General Electric, Milwaukee, WI) using a custom built, single tune birdcage head coil with a frequency of 33.8 MHz (see figure 6.1). A 3D printed phantom with a removable lid (figure 6.1) was filled with different concentrations (13, 23, and 60 mM) of sodium in gelatin – the latter solution was doped with additional $NaCl$ for a final concentration of 60 mM.

6.2.2 Pulse Sequences

Acquisitions used the GE MNS Research Pack (b. 2018-07-18). DA-3DPR and FLORET were both designed with custom Python software. Transmit gain and frequency calibrations were performed using the Bloch-Siegert shift [98].

DA-3DPR

DA-3DPR used a center-out trajectory design, with the following parameters – TR: 24 ms, TE: 0.5 ms, FOV: 240 mm, flip angle: 70°, 13500 spokes, 2 averages, TA: 10:48 for a (designed) voxel resolution of 3.2 mm isotropic. The acquisitions were in the coronal plane and used gradient spoiling at the end of the readout. Sampling efficiency was defined as the ratio of readout window to TR – for DA-3DPR, this was $20/24 = 0.83$.

FLORET

The FLORET acquisitions had the following parameters: TR: 24.3 ms, TE: 0.5 ms, FOV: 240 mm, flip angle: 70°, 3 hubs, 150 interleaves / hub, 64 averages, TA: 11:40 with the same designed isotropic resolution of 3.2 mm. The FLORET acquisitions were also coronal with gradient spoiling. Sampling efficiency was 0.82.

6.2.3 Reconstruction and Analysis

The non-uniform fast Fourier transform (NUFFT), as part of the Berkeley Advanced Reconstruction Toolkit (BART) [99] was used to reconstruct 1 mm isotropic images. Region of interest (ROI) analysis was conducted with the FMRIB Software Library (FSL) [100], and the data were used to create MTFs using the method described by González-López [101]. Each comb was subdivided into 5 sections, so that they each provided 5 data points for the MTF. Each ROI had a width of 20 pixels, which was averaged into a single line profile. MTFs and PSFs were assumed to be Gaussian for fitting purposes. Analyses, including SNR, R^2 values and PSF FWHMs, were performed with Python and Matplotlib [102].

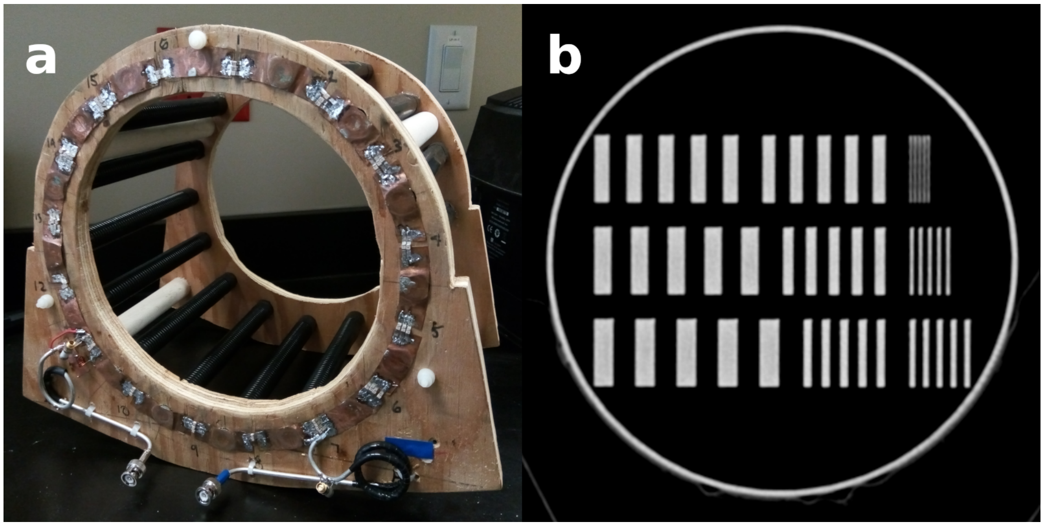

Figure 6.1: (a) single channel quadrature, transmit and receive ^{23}Na head coil used in these experiments. (b) Computed Tomography image of phantom. Resolutions are split into 9 areas with positive and negative contrasts ranging from 1 to 9 mm. Top row, left to right: 7 6 1; middle: 8 5 2; bottom: 9 4 3 (all in mm).

6.3 Results

Images from each acquisition are shown in figure 6.2, with accompanying derived MTF and PSF curves in figure 6.3. Table 6.1 has the SNR, R^2 values for the MTF fits and PSF FWHM values for each acquisition and ^{23}Na concentration.

Image quality (SNR and visual appearance), was superior for the 3DPR acquisitions. As expected, SNR increases with ^{23}Na concentration, although not in a direct linear fashion. The FWHM values were largely unchanged among the different phantoms, although quantitatively smaller for the 3DPR acquisitions – this indicates that PSF performance is largely indifferent to the inherent ^{23}Na concentration for these acquisitions and reconstructions.

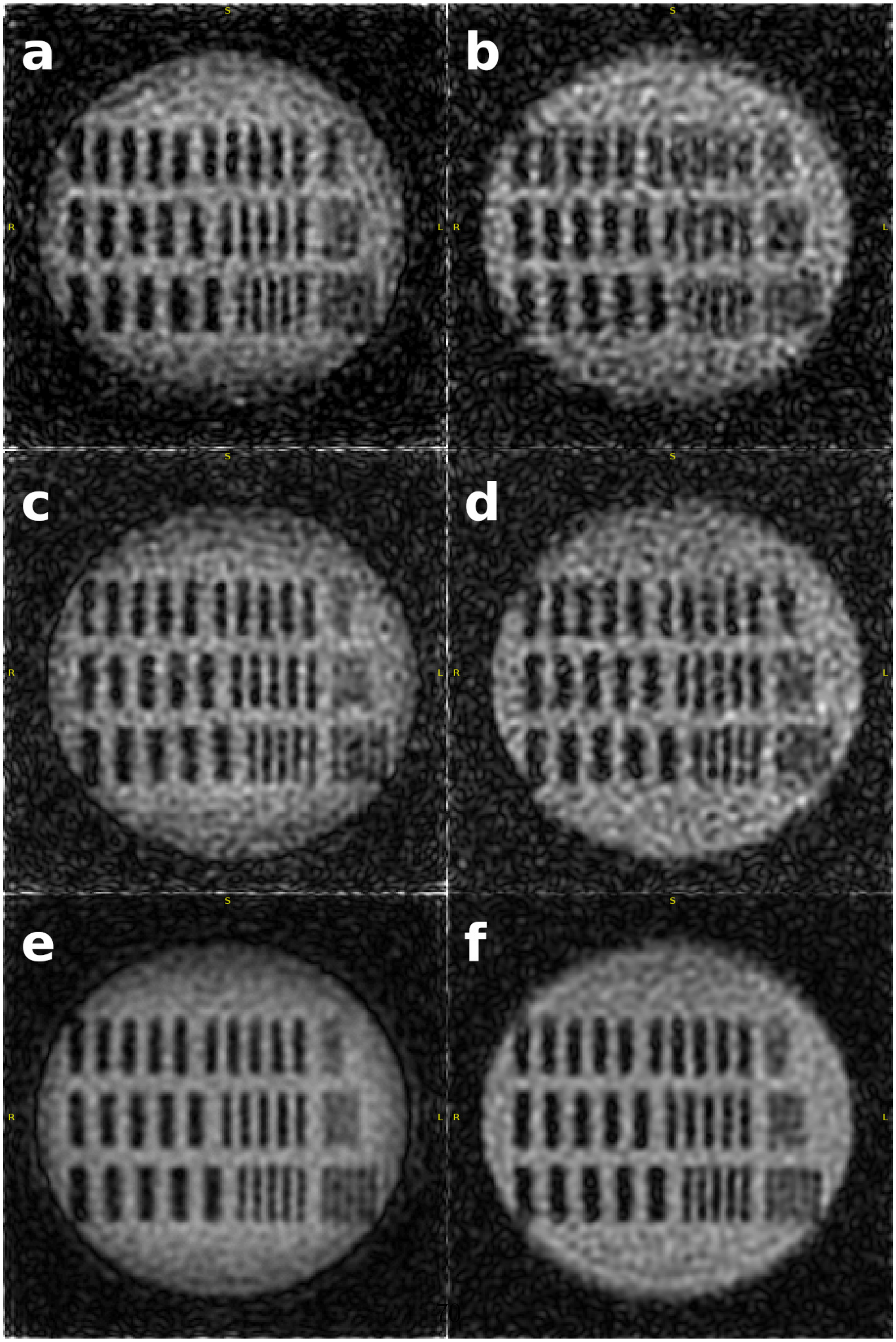

Figure 6.2: (a-f) ^{23}Na images. All images individually windowed to similar pixel intensities. (a-c) 3DPR: 13, 23, 60 mM (d-f) FLORET: 13, 23, 60 mM.

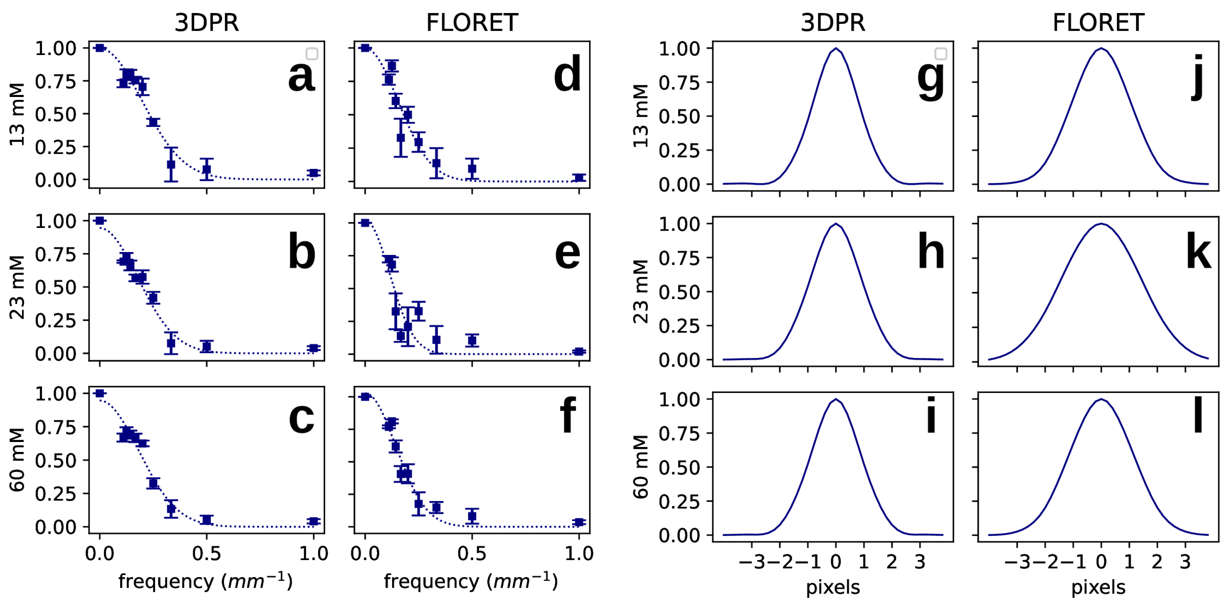

Figure 6.3: (a-f) MTFs and (g-l) PSFs. (a-c) 3DPR: 13, 23, 60 mM (d-f) FLORET: 13, 23, 60 mM. (g-i) 3DPR: 13, 23, 60 mM (j-l) FLORET: 13, 23, 60 mM.

	3DPR			FLORET		
	SNR	FWHM	R^2	SNR	FWHM	R^2
13 mM	11.7	1.92	0.95	9.5	2.47	0.91
23 mM	12.8	2.13	0.97	11.5	3.32	0.83
60 mM	16.9	2.07	0.96	12.2	2.66	0.96

Table 6.1: 3DPR: 3D projection reconstruction; FLORET: Fermat looped orthogonally encoded trajectories; FWHM: point spread function full width half maximum; R^2: modulation transfer function R-squared fit; SNR: signal to noise ratio.

6.4 Discussion

This work detailed initial efforts to measure the MTFs and related PSFs from ^{23}Na MRI in a 3D printed phantom. The experiments used sodium concentrations of 13, 23, and 60 mM, with both DA-3DPR and FLORET acquisitions. The pulse sequence parameters were kept similar between DA-3DPR and FLORET, while the image reconstruction pipelines were identical.

This work has a few limitations – the largest one being the choice of gelatin as a medium in lieu of agar. Agar is a combination of linear polysaccharide agarose and smaller molecules called agaropectin [103]. The initial assumption was that gelatin would be the superior phantom material, as its origin as animal proteins would indicate a condition closer to what is found in vivo. Gelatin also has the added benefit of being easier to prepare and dispose of. However, choosing gelatin actually turned out to be sub-optimal – gelatin actually displays a monoexponential T_2^* decay [104]. This is on account of its rotational correlation time, τ_c, being quite short (i.e. $\omega_0\tau_c \ll 1$) [105], and thus gelatin is actually a *type d* material, as shown in figure 3.3. Agar is derived from algae; ^{23}Na dissolved in this medium does display biexponential T_2^* decay, as we would expect from *type c* materials [104].

The choice to model the MTFs and PSFs with single exponential was (inadvertently) correct, as gelatin does have a monoexponential decay However, the motivation behind this work was to model imaging performance for ^{23}Na brain MRI, which has biexponential decay.

As seen in table 6.1, FLORET PSF performance is inferior to that of DA-3DPR, despite approximately equal acquisition times and readout windows. FLORET samples k-space more efficiently than DA-3DPR, and in this study an increased number of averages was used in order to create a more equal comparison. One possible explanation for the PSF disparities is the increased gradient demands, in terms of slew rate and maximum strength, that are required for the FLORET acquisition (see figures 4.2 and 4.3). An increased demand upon the gradients may introduce eddy currents, group delay, or gradient amplifier nonlinearities which can all affect image quality. Although not conducted in this pilot study, methods exist which can detect and correct for these nonlinearities [106, 107].

As noted by Nagel [89], balancing readout window length with acquisition time, Nyquist criterion for field of view coverage and sampling efficiency is a difficult problem, and is partly governed by T_2^* rates in the tissue to be imaged. The sequence parameters chosen here were governed by the desire to measure the PSF with a sequence that would be appropriate for in vivo brain imaging – thus, a FOV of 240 mm in less than 12 minutes for either acquisition. Having longer acquisition windows would increase sampling efficiency; however, as noted by Nagel [89] this can lead to increased blurring and broader PSF. Akbari [108] also investigated acquisition window length and found an increased ^{23}Na SNR in articular cartilage with increased readout windows, with only a modest widening of the PSF. These studies informed the design choices in this pilot study, particularly for the choice of a 20 ms receiver window.

This study assumed that the PSF was stationary across the field of view, and also only considered a single acquisition plane (i.e. coronal). In general this assumption may not apply, due to B_0 and B_1^+ inhomogeneities, gradient non-linearity, and the PSFs we expect from non-Cartesian acquisitions [89, 109, 110]. However, the methods employed in this study can be expanded to include more complicated studies, by altering the imaging field of view or acquisition plane in order to account for non-stationary PSFs and other orientations.

6.5 Conclusions

These experiments demonstrate the PSF performance of 3DPR and FLORET acquisitions for ^{23}Na phantoms in gelatin. The results, however, cannot indicate the performance that can be expected from in vivo applications, due to the selection of a monoexponential decay material. The methodological shortcomings discussed here were addressed and helped inform the paper detailed in the next chapter.

Chapter 7

An Approach to Evaluation of the Point Spread Function (PSF) for ^{23}Na MRI

Paul Polak M.A.Sc, Rolf F. Schulte Ph.D, Michael D. Noseworthy Ph.D, P.Eng

7.1 Context of the Paper

This paper examines the measurement of the PSF and MTF for ^{23}Na MRI. The goal of this work was an investigation into the variability in PSF measurements under the noisy conditions that are expected in ^{23}Na MRI. Two methods to measure the MTF were considered – direct modulation (DM) and the Fourier 1^{st} harmonic (FH). Simulation experiments indicated that the DM method had more variability. For the phantom experiments, both

DA-3DPR and FLORET acquisitions were considered and these confirmed the simulation results. This paper demonstrated the evaluation of the PSF for ^{23}Na MRI, and the result of image noise in the underlying derivations.

7.2 Declaration Statement

Paul Polak tuned and matched the ^{23}Na head coil, and produced the software in order to run the simulations, acquire the DA-3DPR and FLORET data, image reconstruction and data analysis. As the first author he wrote the first draft, and performed subsequent alterations based on the advice of the other authors. Rolf Schulte provided the software framework for the MRI acquisitions, and provided valuable input in drafting the manuscript. Michael D. Noseworthy provided funding from the Natural Sciences and Engineering Research Council of Canada, coil structure, and 3D phantom design. He is also the corresponding author, and provided essential editing and submission of the paper.

This paper has been published by NMR in Biomedicine. Oct 2021; doi: 10.1002/nbm.4627.

7.3 Paper

An Approach to Evaluation of the Point Spread Function (PSF) for ^{23}Na MRI

Paul Polak[1,2], Rolf F. Schulte[3], Michael D. Noseworthy[1,2,4,5]

1. *School of Biomedical Engineering, McMaster University, Hamilton, ON, Canada*
2. *Imaging Research Centre, St. Joseph's Healthcare, Hamilton, ON, Canada*
3. *GE Healthcare, Munich, Germany*
4. *Electrical and Computer Engineering, McMaster University, Hamilton, ON, Canada*
5. *Department of Radiology, McMaster University Hamilton, ON, Canada*

Corresponding Author:

Dr. Michael D. Noseworthy, PhD PEng

Department of Electrical and Computer Engineering

McMaster University

1280 Main Street West., Hamilton, Ontario, Canada. L8S 4K1

VOICE: (905) 525-9140 x23727

EMAIL: nosewor@mcmaster.ca

Running Title: PSF for 23Na MRI

Keywords: 23Na MRI, point spread function, modulation transfer function, 3D printed phantom, DA-3DRP, FLORET

7.3.1 Abbreviations

- ^{23}Na: sodium
- CT: computer tomography
- DA-3DRP: density-adapted 3D radial projections
- DM: direct modulation
- FH: Fourier harmonic
- FLORET: Fermat looped orthogonally encoded trajectories
- FOV: field of view
- FSL: FMRIB Software Library
- FWHM: full width half maximum
- MTF: modulation transfer function
- PSF: point-spread function
- ROI: region of interest
- SNR: signal to noise ratio
- SRF: spatial response function
- UTE: ultra-short TE

7.3.2 Abstract

Purpose

Despite the technical challenges which require lengthy acquisitions to overcome poor signal-to-noise ratio (SNR) sodium (^{23}Na) MRI is an intriguing area of research due to its essential role in human metabolism. Low SNR images can impact the measurement of the point-spread function (PSF) by adding uncertainty into the resulting quantities. Here we present methods to calculate the PSF by using the modulation transfer function (MTF), and a 3D-printed line-pair phantom in the context of ^{23}Na MRI.

Theory and Methods

A simulation study investigated the effect of noise on the resulting MTF curves which were derived by direct modulation (DM) and a method utilizing Fourier harmonics (FH). Experimental data utilized a line-pair phantom with 9 spatial frequencies, filled with different concentrations (15, 30, and 60 mM) of sodium in 3% agar. MTF curves were calculated using both methods from data acquired from density-adapted 3D radial projections (DA-3DRP) and Fermat looped orthogonally encoded trajectories (FLORET).

Results

Simulations indicated the DM method has increased variability in the MTF curves at all tested noise levels over the FH method. For the experimental data, the FH method resulted in PSFs with narrower full widths half maximums with reduced variability, although the improvement in variability

was not as pronounced as predicted by simulations. The DA-3DRP data indicated an improvement in the PSF over FLORET.

Conclusion

A 3D-printed line-pair phantom represents a convenient method to measure the PSF experimentally. The MTFs from the noisy images in ^{23}Na MRI have reduced variability from a Fourier harmonic method over direct modulation.

7.3.3 Introduction

In vivo sodium (^{23}Na) MRI is desirable due to its essential role in cellular homeostasis, pH regulation, and action potential propagation in neurons and muscle. However, acquiring sodium images is technically challenging [1,2]. Among the difficulties are the physical properties of ^{23}Na (low gyromagnetic ratio, short T_2 relaxation times, low concentration as compared to proton imaging), special hardware requirements (broadband RF amplifier and dedicated transmit and receiver coils), non-standard pulse sequences (ultra-short or zero TE imaging) with accompanying reconstruction approaches, and long acquisition times to account for low signal-to-noise ratio (SNR) [3-5]. Despite these problems, sodium imaging remains an attractive prospect for a variety of in vivo applications, including stroke, multiple sclerosis, Alzheimer's disease, cartilage imaging, skeletal muscle assessment (especially for channelopathies) and thoracic imaging [6-9]. Sodium MRI's difficulties result in a signal 1000 fold lower compared to proton MRI, and this has led to investigations in the use of higher strength magnetic fields for in vivo human imaging [10-12], but has been used to date in field strengths of up to 21.1 T in preclinical imaging. [13] However, research into ^{23}Na MRI at clinical field strengths (currently $B_0 \leq 3$ T) remains attractive because of the potential of translational and comparative research with more traditional clinical MRI techniques and also due to the widespread prevalence of 3T scanners now available in clinical settings.

Owing to the very short T_2^* relaxation times, ultra-short TE (UTE) acquisition techniques are preferred – among these are the density adapted 3D radial projections (DA-3DRP) [4] and Fermat looped orthogonally encoded trajectories (FLORET) [14] acquisition schema. Both have been used for ^{23}Na MRI [15-18], along with regridding or iterative methods for image reconstruction. Considerable research has focused on techniques to measure intra- and extracellular sodium concentrations [16,17,19], bound and unbound pools, relaxivity properties of the spin 3/2 system [20-24], and the effects on the quadrupolar interactions on the resulting signal [25-28]. However, there has been less focus on acquisition and reconstruction techniques, and their effect upon the resultant image point spread function (PSFs). In particular, low SNR acquisitions impact PSF quantification – noise in the input images result in a high variability in the measurement, and the result is highly dependent on the placement of regions of interest (ROIs). Together, low SNR and a PSF with a broad full width half maximum (FWHM) confound the detection of small structures and low sodium concentrations [29].

The work presented here examines the PSF, as a measure of sequence and reconstruction performance, in the context of sodium MRI. Because the PSF is difficult to measure experimentally we used the modulation transfer function (MTF) which is related to the PSF through the Fourier transform.

In particular, the various techniques were examined through simulation, a 3D-printed bar (aka line-pair) phantom, and multiple sodium concentrations.

7.3.4 Theory

A quadrature detector for MRI contains information from both the real and imaginary signals. The noise for each signal can be assumed Gaussian, with a mean of zero [30]. The result of the inverse Fourier transform of this data is complex, and magnitude reconstructions are typically performed in order to avoid problems with artifacts from phase; the resulting noise in the background of the magnitude image is then best described as a Rayleigh distribution [31]. However, the noise in magnitude images is typically expressed as Gaussian, since the Rayleigh distribution begins to be accurately approximated by a Gaussian at an SNR > 3 [30-32].

The PSF can be calculated from the MTF from the inverse Fourier transform, as:

$$PSF = \mathcal{F}^{-1}(MTF) \tag{7.1}$$

where the inverse Fourier transform, $\mathcal{F}^{-1}$, can be multi-dimensional. In order to compute the MTF with a comb or bar phantom, we can use direct modulation (DM) as the following:

$$MTF_f = \frac{I_{max,f} - I_{min,f}}{I_{max,f} + I_{min,f}} \tag{7.2}$$

where f is the particular frequency measured in line pairs mm^{-1}, and $I_{max,f}$ and $I_{min,f}$ are the maximum and minimum intensities for f across the profile. If we consider the hypothetical case with normally distributed noise function

N, with mean 0 and variance σ_{n^2} (i.e. homoscedastic) then the MTF with noise, denoted $MTF_{f,N}$, becomes:

$$MTF_{f,N} = \frac{\mu_1 + N(0, 2\sigma_n^2)}{\mu_2 + N(0, 2\sigma_n^2)} \tag{7.3}$$

This expression is the ratio of two correlated Gaussian random variables, with means $\mu_1 = I_{max,f} - I_{min,f}$, and $\mu_2 = I_{max,f} + I_{min,f}$. The variance of this expression is non-trivial to evaluate, and as demonstrated by Geary, [33] leads to instabilities in the expression if μ_1 and μ_2 are both zero, or near zero. However, as long as $\mu_2 \geq 6\sigma_{n^2}$, the expression is well behaved and normally distributed [33].

An alternative method to evaluate the MTF was proposed by González-López et al. [34], which we denote as the Fourier 1st harmonic (FH) and present here for reference:

$$MTF_f = \left| \frac{F_{1,f}}{G_1} \right| \tag{7.4}$$

Where $F_{1,f}$ and G_1 denote the first odd harmonics of the Fourier transforms of the system output for a given frequency and the ideal output. As demonstrated by González-López [35], the variance for the noisy MTF has a linear dependence on noise and frequency.

$$\sigma^2_{MTF}(f) \propto f\sigma_n^2 \tag{7.5}$$

As the noise characteristics of the FH method is correlated with frequency, we expect better performance in terms of MTF stability at low frequencies.

MTF performance of both methods under noisy conditions were measured by simulations and experiments.

7.3.5 Methods

Simulations

A simulated bar phantom was created with 25 combs of differing resolutions, with teeth widths measuring from 200 to 10 pixels. The phantom was created with two values, 1 and 0, representing signal and the lack thereof respectively, and the size of the created phantom was 3360 x 3360 pixels (Figure 7.1). The phantom was then downsampled by a factor of 4, and was then convolved with a point-spread function derived from the theoretical biexponential T_2^* decay for ^{23}Na MRI ($S(t) \approx c_f e^{-t/T^*_{2f}} + c_s e^{-tT^*_{2s}}$) with a 20 ms readout, where T^*_{2f} / T^*_{2s} = 4/30 ms represent the fast and slow T_2^* decay in tissue, and c_f/c_s = 0.6/0.4 are the relative contributions from each component) [3,36]. This final phantom had 25 ROIs created to measure the data for each comb in the phantom. Each ROI spanned one period for each comb, and were created with a width of 28 pixels. The mean data across the 28 pixels were used in the MTF and contrast calculations described below.

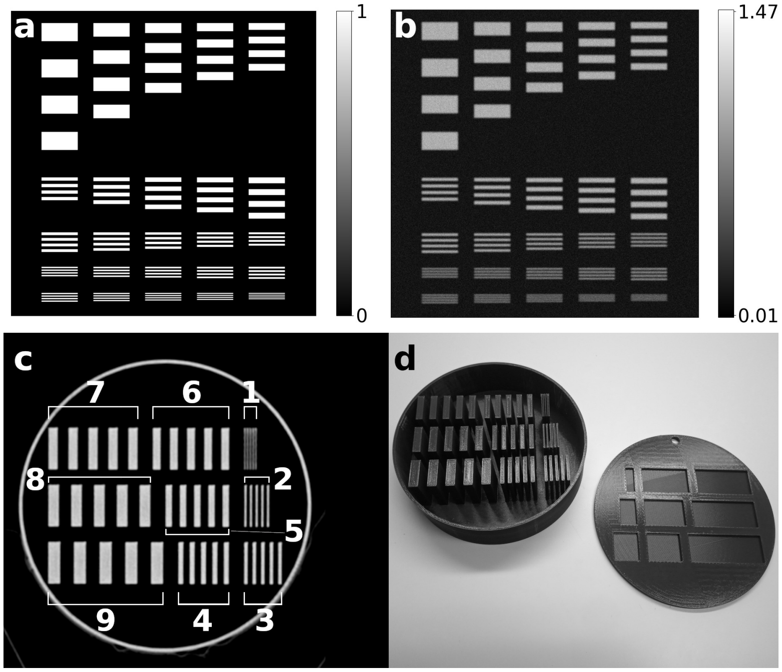

Figure 7.1: Simulated and phantom images. Greyscale bars representing maximum and minimum values are shown on the right for (a) and (b). (a) Simulated noise-free phantom image, measuring 3360 x 3360 pixels. There are 25 different comb widths, organized from the upper left, left to right, and then down, as: 200, 150, 110, 90, 75, 36, 42, 50, 55, 65, 31, 29, 26, 23, 21, 15, 16, 17, 18, 19, 14, 13, 12, 11, and 10 pixels, respectively. Values are binary, with 0 being black and 1 white. (b) Simulated magnitude image phantom data after downsampling and application of a ^{23}Na point-spread function (PSF) and the addition of normally distributed complex noise. The given image had a noise level of $\sigma_n = 0.1$. (d) Computed tomography (CT) image of the 3D-printed phantom showing the consistency of the 3D-printed line pairs. Resolutions are split into nine areas of positive and negative contrast, with line-pair groups annotated as indicated, with the numbers 1 to 9 indicating 1- to 9-mm groups, respectively. The CT imaging system was a Siemens Biograph 16, with the following parameters: peak tube voltage, 120 kV; tube current, 52 mA; field of view (FOV), 292 mm; 512 x 512 resolution; 0.57 x 0.57 mm2 in-plane resolution; and slice thickness, 1 mm. (d) Photograph of (empty) 3D-printed phantom with the cover removed. The phantom is disk-shaped, with a diameter of 205 mm and height of 60 mm with the cover. Note that the .stl 3D printer files are available in the supporting information.

Complex noise was added to the final phantom by creating individual real and imaginary noise centered at 0, with standard deviation values of 0.05, 0.1, 0.15, 0.2, 0.3, and 0.4. The noise was added to the noise-free phantom data before the magnitude of the combined phantom and noise was calculated (Figure 7.1). Monte-Carlo simulations were performed for 2500 trials at each noise level – the data from each ROI was sampled and MTF were created using both the DM and FH methods, and then plotted. Means and variances were calculated across the trials for each noise level and comb frequency. For the purposes of the simulations, TE was set to 0, while T_1 effects and remaining residual T_2^* signal following the readout were ignored.

Experiments

All experiments were conducted using a GE 3T MR750 (General Electric Healthcare, Waukesha, WI), with maximum gradient amplitude and slew rate of 50 mT/m and 200 T/m/s respectively. A custom designed and built single-tune quadrature birdcage head coil with resonant frequency of 33.8 MHz was used. The coil was cylindrical, measuring 245 mm in length, outer diameter of 320 mm, with a maximum imaging diameter of 240 mm. A phantom was designed and 3D-printed to have 9 bar phantom regions, or "combs" (1-9 mm) of positive and negative contrast in order to create the MTFs (Figure 7.1). The phantom was 205 mm in diameter with a height of 56 mm (without cover). A computed tomography (CT) dataset (Siemens Biograph 16, tube current 52 mA, peak tube voltage 120 kV, in-plane resolution 0.57 x 0.57 mm2, slice thickness 1 mm) was also acquired as the "gold standard" compared to MRI, and demonstrates both the geometric truth and high resolution desired in a phantom experiment. The phantom was designed with a removable lid such that the phantom could be imaged with different sodium concentrations. For these experiments three concentrations were used: 15, 30 and 60 mM NaCl in 3% agar (Sigma-Aldrich https://www.sigmaaldrich.com/CA/en. A-7002).

MR Imaging was conducted using the GE MNS Research Pack (v. 2018-11-13) for all acquisition schemes. The field of view (FOV) for all acquisitions was set to 240 mm as this is a likely target for neuroimaging. Matlab (The Mathworks Inc., Natick, MA) scripts were used to calibrate the transmit gain and imaging frequency prior to imaging [37]. Two common ^{23}Na imaging strategies were compared: DA-3DRP and FLORET. Both acquisitions were used for each phantom concentration. Acquisition times were set to be approximately equal, and represent a length of time which would be considered reasonable for an in vivo subject. Readout window lengths were determined based on observations made by Nagel et al. [4]. Residual T_2^* signal at the end of the readout was eliminated with crusher gradients for both acquisition types.

DA-3DRP DA-3DRP UTE trajectories were density-adapted and designed to sample at 1/r with 13500 spokes, at polar angles calculated from points equally distributed on a sphere, and with an isotropic resolution of 3.2 mm at a FOV of 240 mm. A steady-state acquisition scheme was used in order to minimize acquisition time (TA) at the expense of incomplete T1 relaxation. Imaging parameters were: TR: 24 ms, TE: 0.2 ms, flip angle: 70°, RF pulse length: 0.6 ms, receiver bandwidth: 50 kHz, with a receiver window of 20 ms. TA was 10:48 minutes for 2 averages.

FLORET FLORET trajectories were designed with 3 orthogonal hubs, 150 interleaves / hub. Other parameters were: FOV: 240 mm, isotropic acquisition of 3.2 mm, TR: 24.3 ms, TE: 0.2 ms, flip angle: 70°, RF pulse length: 0.6 ms, receiver bandwidth: 50 kHz, and receiver window: 20 ms. TA was 11:40 minutes for 64 signal averages. FLORET samples k-space more efficiently than DA-3DRP, and hence averaging was used in order to provide a similar TA to the DA-3DRP experiments.

Reconstruction and Analysis

All ^{23}Na MR images were reconstructed via density-compensation and 3D gridding as provided by the Berkeley Advanced Reconstruction Toolbox [38]. Files were reconstructed into NIFTI format, with dimensions 240 x 240 x 240. Example magnitude images for each concentration and acquisition are shown in Figure 7.2.

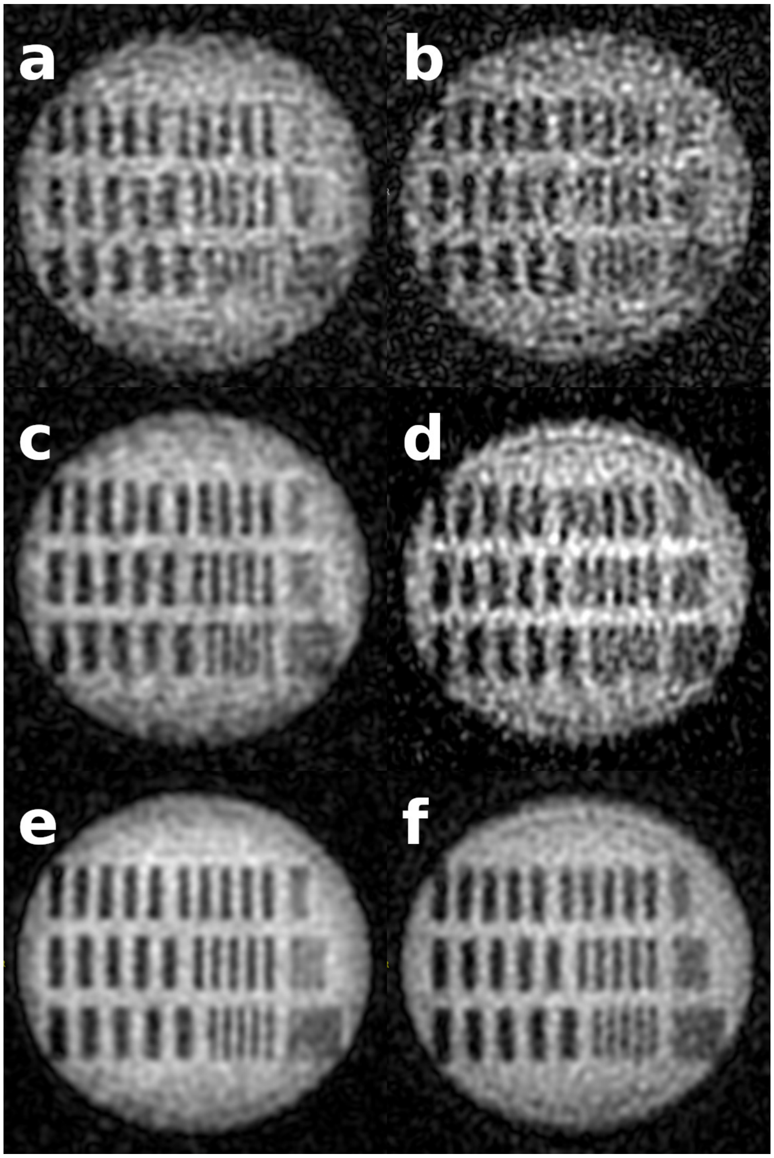

Figure 7.2: Sample ^{23}Na magnitude images. Left column, DA-3DRP; right column, FLORET. (a) and (b) 15 mM; (c) and (d) 30 mM; and (e) and (f) 60 mM. DA-3DRP images: TR, 24.0 ms; TE, 0.5 ms; flip angle, 70^o, acquisition time, 10 min 48 s (two averages). FLORET images: TR, 24.3 ms; TE, 0.5 ms; flip angle, 70^o; acquisition time, 11 min 40 s (64 averages). Both acquisitions have an isotropic resolution of 3.2 mm, and were acquired at a field of view (FOV) of 240 mm, and a reconstruction size of 240 x 240 x 240. The images have been windowed individually.

Cross-section ROIs were created with FMRIB Software Library (FSL) [39] v6.0 for the 9 different bar phantom regions on the magnitude images. ROIs were created to span each comb, with depths and widths of 20 pixels respectively. Mean line profiles were taken along both depth and width by 4 pixels each. As each bar region has 5 periods, this leads to a total of 125 samples for each spatial frequency. An analysis of the CT and MRI (DA-3DRP and FLORET, 60 mM concentration) images in terms of geometric truth, as compared to the measured phantom dimensions, was performed with FSL. Geometric truth was assessed using two perpendicular diameter measurements (in plane, left / right and inferior / superior), in addition to the 9 bar phantom regions used in evaluation of the MTF. Zero frequency data was constructed from the average signal in ROIs taken in homogeneous appearing regions inside and outside the phantom, and then using the DM or FH method respectively.

Sodium images are expected to be noisy, with resultant effects upon the efficacy of MTF calculations. Both DM and FH methods were used to calculate the MTFs. The data from both methods were fit to a function in the form $a_1e^{\sigma_1} + a_2e^{\sigma_2}$ in order to reproduce the expected biexponential decay for ^{23}Na MRI, with a_1/σ_1 and a_2/σ_2 representing the fractions / T_2^* decays for the fast and slow components respectively. PSFs were calculated from the fitted data by the inverse Fourier transform. Python and Matplotlib [40] were used to visualize the data, and FSL was used for SNR calculations. Chi-squared (χ^2) and mean squared residuals were calculated to evaluate the quality of each biexponential fit.

7.3.6 Results

Simulations

MTF curves for the DM and FH methods are shown in Figure ref3a. The DM method consistently over-estimates the MTF performance in regards to the noise-free simulation, while the FH method is much more consistent with the noise-free curve at all noise levels. The DM is more susceptible to noise, and has a much larger variance as compared to the FH method seen in Figure ref3b. Comparatively, the FH method demonstrates the behavior as dictated by equation 7.5, where the variances increase with frequency, but remained fairly low at low frequencies. Although both methods have increased variance as the noise level increases, the FH method demonstrates superior performance in terms of reduced variance from the noise-free MTF – i.e. at the lowest frequencies the variance of the FH method is approximately 10% of the DM method.

Experiments

The CT images were used to judge whether the geometric truth in the sodium MR images was appropriately preserved and also to judge whether the distance between combs at different spatial frequencies was consistent in the 3D printing. Geometric analysis of the CT and MRI images can be found in Table 7.1. The MR images were consistent with the manufactured design when accounting for the PSF of the sodium acquisitions and reconstructions. There were slight deviations ($< 3\%$) between the left / right and inferior / superior diameter measurements which were deemed acceptable.

Figures 7.4 exhibit the MTF curves and variances for the experimentally acquired MRI data. The FH method indicates superior FWHMs (Table 7.2) for each of the 6 reconstructions (i.e. DA-3DRP and FLORET acquisitions for 15, 30, and 60 mM concentrations). In addition, the variance in the FH method was lower at the lower spatial frequencies, although the effect was not as pronounced as demonstrated by the simulation data. For higher spatial frequencies, particularly the data from bar regions of 1-3 mm, the variances were markedly lower for both methods.

	Phantom	CT	DA-3DPR MRI	FLORET MRI
LR diameter	205.0	205.8	203	203
IS diameter	205.0	205.8	197	198
9 mm	81.0	81.6	83	82
8 mm	72.0	73.0	74	74
7 mm	63.0	63.3	65	63
6 mm	54.0	54.7	55	54
5 mm	45.0	45.6	46	46
4 mm	36.0	36.5	37	37
3 mm	27.0	27.4	32	32
2 mm	18.0	18.2	21	20
1 mm	9.0	10.2	12	12

Table 7.1: Geometric analysis of CT and 23Na MRI images (acquisition parameters as specified in Methods section). The diameter measurements were taken in the direction indicated (LR or IS) on the image. Bar region measurements (9 mm, etc.) taken across the entire comb (9 positive and negative contrasts). Abbreviations – CT: computed tomographic image; DA-3DPR MRI: ^{23}Na MRI density-adapted 3D radial projection image; FLORET MRI: ^{23}Na MRI Fermat looped orthogonally encoded trajectories image; IS: inferior / superior; LR: left / right.

Acquisition	[^{23}Na] (mM)	SNR	DM			FH		
			MSR (× 1e-4)	χ^2 (p-value)	FWHM	MSR (× 1e-4)	χ^2 (p-value)	FWHM
DA-3DRP	15	10.4	1.02	0.34 (> 0.99)	2.67	2.09	0.09 (> 0.99)	1.91
	30	16.5	4.09	1.79 (> 0.99)	2.78	1.84	0.37 (> 0.99)	2.10
	60	26.9	4.78	0.89 (> 0.99)	2.85	1.78	0.16 (> 0.99)	2.09
FLORET	15	7.7	1.23	0.02 (> 0.99)	2.16	1.72	0.02 (> 0.99)	1.91
	30	11.2	2.26	1.19 (> 0.99)	3.11	0.92	0.38 (> 0.99)	2.60
	60	24.1	4.47	2.93 (> 0.96)	3.26	0.93	0.61 (> 0.99)	2.59

Table 7.2: SNR for images, and χ^2 values and FWHM for MTF Gaussian fits in Figure 7.4, organized by acquisition and sodium concentration. Abbreviations – DA-3DRP: density adapted 3D radial projection; DM: direct modulation; FH: Fourier harmonic; FLORET: Fermat looped orthogonally encoded trajectories; FWHM: full-width, half maximum of point-spread function; MSR: mean squared residuals for biexponential fit; SNR: signal to noise ratio; χ^2: Chi-Squared values for fit.

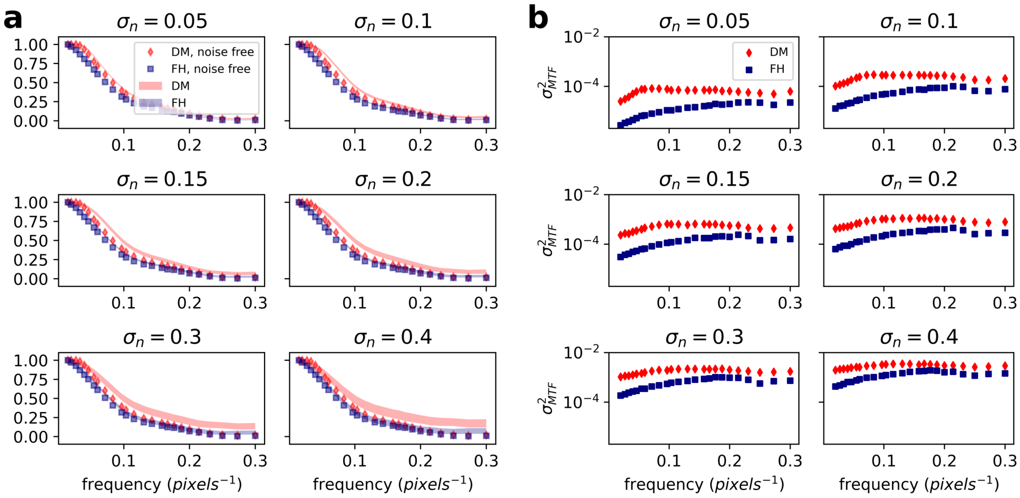

Figure 7.3: (a) Simulation modulation transfer function (MTF) curves for the direct modulation (DM; red diamonds) and Fourier harmonic (FH; blue squares) methods for all indicated noise levels. Data points are the noise-free MTFs, and solid fills represent the mean ± standard deviation across all trials for each noise level and frequency. (b) Simulated MTF variances (log) versus frequency data for the DM (red diamonds) and FH (blue squares) methods for all simulated noise levels.

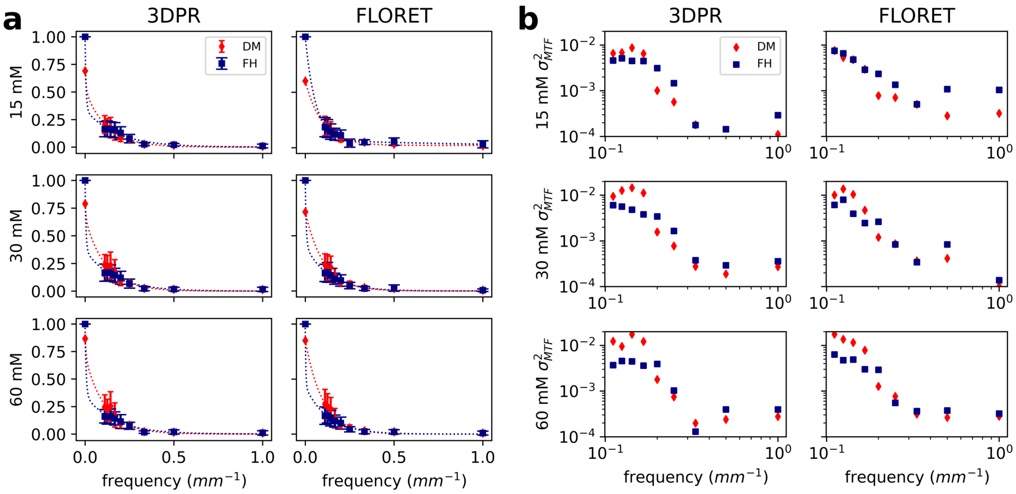

Figure 7.4: (a) Modulation transfer function (MTF) curves for the direct modulation (DM) and Fourier harmonic (FH) methods, with sodium concentrations of 15, 30, and 60 mM (rows) and DA-3DRP and FLORET acquisitions (columns). DM data are indicated as red diamonds, and FH data as blue squares. Biexponential fits to the MTF curves are indicated by dashed lines (Table 7.2 gives the χ^2 and mean squared residuals values). (b) MTF variances (log) versus frequency (log) for the same concentrations and acquisitions.

7.3.7 Discussion

Image resolvability is important, especially when delineating the boundary between, for example, white and grey matter in brain imaging. The ability to resolve fine structures in images is commonly measured through the PSF or MTF. Thus, the purpose of this work was to examine the robustness of MTF and PSF calculations, in the context of noisy acquisitions which are common in ^{23}Na MRI. In particular, two methods for calculating the MTF from a bar phantom were examined – DM, from the maximum and minimum intensities from a profile, and the FH method utilizing the 1st Fourier harmonic. From the simulations, both methods' performance degrades with increasing noise levels, but is particularly magnified for the DM method. Two observations can be obtained from Figure 7.3: (i) an over-estimation of the MTF at high noise levels, and (ii) the standard deviation of the MTF calculation drastically increases with increasing noise. By contrast, the FH method was more robust under the same experiments, with the noisy MTF estimations more closely aligned with the noise-free calculation with a smaller standard deviation. The variances "level off" at the spatial frequencies for all noise levels. One possible explanation is that the assumption that the noise being accurately modeled by a Gaussian distribution is no longer correct at the higher spatial frequencies and noise levels.

From the experimental data, the FH method indicated a superior FWHM for all concentrations and acquisitions which in general agrees with simulations: at the increased noise levels the DM method tends to underestimate the MTF performance compared to noise-free calculations. The variances for the FH method were less than those calculated by the DM method (Figure 7.4) for the bar regions 6 to 9 mm. Nonetheless, at higher spatial frequencies the variances for both methods were reduced.

The method proposed by González-López et al. [34] is demonstrated to be more robust in noisy conditions as might be expected for ^{23}Na MRI. The PSF and related MTF are fundamental quantitative measurements of imaging performance. While an improvement in this performance might be expected by running experiments in higher SNR conditions (i.e. higher magnetic field strength, more signal averaging), two caveats exist: (i) the improvement in FWHM for the higher sodium concentrations is not evident (Table 7.1), and (ii) SNR improvement by signal averaging results in longer acquisition times. The experiments conducted here were guided by acquisition times which are clinically viable, and thus reflect imaging performance which might be expected for an in vivo subject. With regards to resolution, a FWHM of 2.0 (Table 7.2) for the DA-3DRP (designed for 3.2 mm resolution) sequence results in an effective resolution of approximately 6.4 mm, which compares favorably to recent efforts (5.2 mm) at 7 T [41].

Gibbs ringing artifacts are problematic for ^{23}Na MRI because of the large acquisition voxels and low resolution, relative to proton MRI, which are required to achieve adequate SNR. Methods to reduce this artifact include alterations in acquisition and post-filtering [42-44]. The authors indicate that SNR also increased versus a DA-3DRP acquisition – however, both of these techniques also broaden the PSF. The choice to use either method is dependent on readout duration and T_2^* decay, with longer readout favoring a post-filtered technique.

^{23}Na MRI has been demonstrated to be useful in assessing stroke [45,46], although the long acquisition times have hampered its adoption in acute cases. Adlung et al. [47] have implemented a neural network approach in an effort to mitigate the increased artifacts and noise which come with accelerated acquisitions. They found that these deep learning approaches can increase SNR with some loss of structural similarity compared to a fully sampled dataset, with the latter implying some broadening of the underlying PSF. Measurement of the PSF with these nascent reconstruction techniques is a potential avenue for future research.

This study has focused attention on the MTF and its associated 1D PSF, and assumed it to be stationary across the field of view. This assumption in general may not apply, due to inhomogeneities in the B0 and B1 fields, transverse relaxation effects during readout, and the more complicated PSFs we expect from non-Cartesian acquisitions and reconstructions [4,14,48]. Other studies have examined the spatial response function (SRF) [49] in the context of spectroscopic and imaging studies. The SRF can be derived from the PSF, and vice versa, with a complete set of PSF data [50]. Ideally, a bar phantom is designed with the projected application known a priori, which would influence FOV, number of bars, bar widths, etc. The use of a 3D printed phantom allows multiple strategies to be created and tested economically. Potential future studies could involve the investigation of a non-stationary PSF, and possible corrective measures involving the B0 and B1 fields, and partial volume correction [29,51,52].

7.3.8 Conclusions

The goal of this work was to examine ^{23}Na MRI MTF measurements in a bar phantom under noisy conditions, with the results indicating its viability despite the inherent variability. The techniques investigated here have the advantage that they do not require any specialized pulse sequence or reconstruction methodology other than what would already be required for ^{23}Na MRI. While the DM method is valid under low or noise-free conditions, the FH method is more robust for the higher noise situations expected with ^{23}Na MRI. The PSF can be difficult to measure experimentally with MRI, but the MTF and 3D printed line-pair phantoms provide one such viable methodology.

7.3.9 Acknowledgments

This work was funded through a Natural Sciences and Engineering Research Council of Canada (NSERC) grant to MDN (grant # RGPIN-17-06318).

7.3.10 References

1. Rose AM, Valdes R. Understanding the sodium pump and its relevance to disease. Clinical Chemistry. 1994;40(9):1674-1685.

2. Skou JC, Esmann M. The Na, K-ATPase. Journal of Bioenergetics and Biomembranes. 1992;24(3):249-261. doi:10.1007/BF00768846

3. Madelin G, Regatte RR. Biomedical applications of sodium MRI in vivo. Journal of magnetic resonance imaging : JMRI. 2013;38(3):511-

529. doi:10.1002/jmri.24168

4. Nagel AM, Laun FB, Weber M-A, Matthies C, Semmler W, Schad LR. Sodium MRI using a density-adapted 3D radial acquisition technique. Magnetic Resonance in Medicine. 2009;62(6):1565-1573. doi: 10.1002/mrm.22157

5. Thulborn KR. Quantitative Sodium MR Imaging: A Review of its Evolving Role in Medicine. NeuroImage. 2016;(November):1-19. doi: 10.1016/j.neuroimage.2016.11.056

6. Madelin G, Lee JS, Regatte RR, Jerschow A. Sodium MRI: Methods and applications. Progress in Nuclear Magnetic Resonance Spectroscopy. 2014;79:14-47. doi: 10.1016/j.pnmrs.2014.02.001

7. Staroswiecki E, Bangerter NK, Gurney PT, Grafendorfer T, Gold GE, Hargreaves BA. In vivo sodium imaging of human patellar cartilage with a 3D cones sequence at 3 T and 7 T. Journal of Magnetic Resonance Imaging. 2010;32(2):446-451. doi: 10.1002/jmri.22191

8. Waxman SG. Mechanisms of disease: sodium channels and neuroprotection in multiple sclerosis-current status. Nature clinical practice Neurology. 2008;4(3):159-169. doi: 10.1038/ncpneuro0735

9. Thulborn KR, Davis D, Snyder J, Yonas H, Kassam A. Sodium MR Imaging of Acute and Subacute Stroke for Assessment of Tissue Viability. Neuroimaging Clinics of North America. 2005;15(3):639-653. doi: 10.1016/j.nic.2005.08.003

10. Juras V, Zbyn S, Pressl C, et al. Sodium MR Imaging of Achilles Tendinopathy at 7 T: Preliminary Results. Radiology. 2012;262(1):199-205. doi: 10.1148/radiol.11110897

11. Madelin G, Lee J-S, Inati S, Jerschow A, Regatte RR. Sodium inversion recovery MRI of the knee joint in vivo at 7T. Journal of Magnetic Resonance. 2010;207(1):42-52. doi: 10.1016/j.jmr.2010.08.003

12. Zaric O, Pinker K, Zbyn S, et al. Quantitative Sodium MR Imaging at 7 T: Initial Results and Comparison with Diffusion-weighted Imaging in Patients with Breast Tumors. Radiology. 2016;280(1):39-48. doi: 10.1148/radiol.2016151304

13. Schepkin VD, Bejarano FC, Morgan T, Gower-Winter S, Ozambela M, Levenson CW. In vivo magnetic resonance imaging of sodium and diffusion in rat glioma at 21.1 T. Magnetic Resonance in Medicine. 2012;67(4):1159-1166. doi: https://doi.org/10.1002/mrm.23077

14. Pipe JG, Zwart NR, Aboussouan EA, Robison RK, Devaraj A, Johnson KO. A new design and rationale for 3D orthogonally oversampled k-space trajectories. Magnetic Resonance in Medicine. 2011;66(5):1303-1311. doi: 10.1002/mrm.22918

15. Boada FE, Gillen JS, Shen GX, Chang SY, Thulborn KR. Fast three dimensional sodium imaging. Magnetic Resonance in Medicine. 1997;37(5):706-715. doi: 10.1002/mrm.1910370512

16. Gilles A, Nagel AM, Madelin G. Multipulse sodium magnetic resonance imaging for multicompartment quantification: Proof-of-concept.

Scientific Reports. 2017;7(1):17435. doi: 10.1038/s41598-017-17582-w

17. Madelin G, Kline R, Walvick R, Regatte RR. A method for estimating intracellular sodium concentration and extracellular volume fraction in brain in vivo using sodium magnetic resonance imaging. Scientific Reports. 2014;4:1-7. doi: 10.1038/srep04763

18. Nielles-Vallespin S, Weber MA, Bock M, et al. 3D radial projection technique with ultrashort echo times for sodium MRI: Clinical applications in human brain and skeletal muscle. Magnetic Resonance in Medicine. 2007;57(1):74-81. doi: 10.1002/mrm.21104

19. Inglese M, Madelin G, Oesingmann N, et al. Brain tissue sodium concentration in multiple sclerosis: A sodium imaging study at 3 tesla. Brain. 2010;133(3):847-857. doi: 10.1093/brain/awp334

20. Worthoff WA, Shymanskaya A, Shah NJ. Relaxometry and quantification in simultaneously acquired single and triple quantum filtered sodium MRI. Magnetic resonance in medicine. 2018;(August 2017). doi: 10.1002/mrm.27387

21. Lommen JM, Flassbeck S, Behl NGR, et al. Probing the microscopic environment of 23Na ions in brain tissue by MRI: On the accuracy of different sampling schemes for the determination of rapid, biexponential T2* decay at low signal-to-noise ratio. Magnetic Resonance in Medicine. 2018;00:1-14. doi: 10.1002/mrm.27059

22. Riemer F, Solanky BS, Clemence M, Wheeler-Kingshott C, Golay X. Bi-exponential 23Na T2* components analysis in the human brain.

Proc Intl Soc Mag Reson Med 20. 2012;20(133).

23. Blunck Y, Josan S, Taqdees SW, et al. 3D-multi-echo radial imaging of 23 Na (3D-MERINA) for time-efficient multi-parameter tissue compartment mapping. Magnetic resonance in medicine. 2018;79(4):1950-1961. doi: 10.1002/mrm.26848

24. Syeda W, Blunck Y, Kolbe S, Cleary JO, Johnston LA. A continuum of components: Flexible fast fraction mapping in sodium MRI. Magnetic Resonance in Medicine. 2019;81(6):3854-3864. doi: 10.1002/mrm.27659

25. Jaccard G, Wimperis S, Bodenhausen G. Multiple-quantum NMR spectroscopy of S=3/2 spins in isotropic phase: A new probe for multiexponential relaxation. The Journal of Chemical Physics. 1986;85(11):6282. doi: 10.1063/1.451458

26. Tanase C, Boada FE. Algebraic description of spin 3/2 dynamics in NMR experiments. Journal of Magnetic Resonance. 2005;173(2):236-253. doi: 10.1016/j.jmr.2004.12.009

27. Maarel JRC van der. Thermal relaxation and coherence dynamics of spin 3/2. I. Static and fluctuating quadrupolar interactions in the multipole basis. Concepts in Magnetic Resonance Part A. doi: 10.1002/cmr.a.10087

28. Stobbe RW, Beaulieu C. Residual quadrupole interaction in brain and its effect on quantitative sodium imaging: Residual Quadrupole Interactions Affect Sodium MRI of the Human Brain. NMR in Biomedicine. 2016;29(2):119-128. doi: 10.1002/nbm.3376

29. Niesporek SC, Hoffmann SH, Berger MC, et al. Partial volume correction for in vivo 23 Na-MRI data of the human brain. NeuroImage. 2015;112:353-363. doi: 10.1016/j.neuroimage.2015.03.025
30. Rice SO. Mathematical Analysis of Random Noise. Bell System Technical Journal. 1944;23(3):282-332. doi: 10.1002/j.1538-7305.1944.tb00874.x
31. Gudbjartsson H, Patz S. The rician distribution of noisy mri data. Magnetic Resonance in Medicine. 1995;34(6):910-914. doi: 10.1002/mrm.1910340618
32. Bernstein MA, Thomasson DM, Perman WH. Improved detectability in low signal-to-noise ratio magnetic resonance images by means of a phase-corrected real reconstruction: Technical Reports: Low SNR MR images. Med Phys. 1989;16(5):813-817. doi: 10.1118/1.596304
33. Geary RC. The Frequency Distribution of the Quotient of Two Normal Variates. Journal of the Royal Statistical Society. 1930;93(3):442. doi: 10.2307/2342070
34. González-López A, Campos-Morcillo PA, Lago-Martín JD. Technical Note: An oversampling procedure to calculate the MTF of an imaging system from a bar-pattern image. Medical physics. 2016;43(10):5653. doi: 10.1118/1.4963211
35. González-López A. Effect of noise on MTF calculations using different phantoms. Medical Physics. 2018;45(5):1889-1898. doi: 10.1002/mp.12847

36. Atkinson IC, Lu A, Thulborn KR. Clinically constrained optimization of flexTPI acquisition parameters for the tissue sodium concentration bioscale. Magnetic Resonance in Medicine. 2011;66(4):1089-1099. doi: https://doi.org/10.1002/mrm.22908

37. Schulte RF, Sacolick L, Deppe MH, et al. Transmit gain calibration for nonproton MR using the Bloch-Siegert shift. NMR in Biomedicine. 2011;24(9):1068-1072. doi: 10.1002/nbm.1657

38. Uecker M, Ong F, Tamir JI, et al. Berkeley Advanced Reconstruction Toolbox. In: Proc Intl Soc Mag Reson Med. ; 2015.

39. Smith SM, Jenkinson M, Woolrich MW, et al. Advances in functional and structural MR image analysis and implementation as FSL. NeuroImage. 2004;23 Suppl 1:S208-19.
doi: 10.1016/j.neuroimage.2004.07.051

40. Hunter J. Matplotlib: A 2D graphics environment. Computing in Science & Engineering. 2007;9(3):90-95. doi: 10.1109/MCSE.2007.55

41. Ianniello C, Madelin G, Moy L, Brown R. A dual-tuned multichannel bilateral RF coil for 1H/23Na breast MRI at 7 T. Magnetic Resonance in Medicine. 2019;82(4):1566-1575.
doi: https://doi.org/10.1002/mrm.27829

42. Konstandin S, Nagel AM. Performance of sampling density-weighted and postfiltered density-adapted projection reconstruction in sodium magnetic resonance imaging. Magnetic Resonance in Medicine. 2013; 69(2):495-502. doi: 10.1002/mrm.24255

43. Konstandin S, Nagel AM. Measurement techniques for magnetic resonance imaging of fast relaxing nuclei. Magn Reson Mater Phy. 2014;27(1):5-19. doi: 10.1007/s10334-013-0394-3

44. Konstandin S, Krämer P, Günther M, Schad LR. Sodium magnetic resonance imaging using ultra-short echo time sequences with anisotropic resolution and uniform k-space sampling. Magnetic Resonance Imaging. 2015;33(3):319-327. doi: 10.1016/j.mri.2014.12.007

45. Boada FE, Qian Y, Nemoto E, et al. Sodium MRI and the Assessment of Irreversible Tissue Damage During Hyper-Acute Stroke. Translational Stroke Research. 2012;3(2):236-245. doi: 10.1007/s12975-012-0168-7

46. Tsang A, Stobbe RW, Asdaghi N, et al. Relationship between sodium intensity and perfusion deficits in acute ischemic stroke. Journal of Magnetic Resonance Imaging. 2011;33(1):41-47. doi: 10.1002/jmri.22299

47. Adlung A, Paschke NK, Golla A-K, et al. 23Na MRI in ischemic stroke: Acquisition time reduction using postprocessing with convolutional neural networks. NMR in Biomedicine. 2021;34(4):e4474. doi: 10.1002/nbm.4474

48. Wright KL, Hamilton JI, Griswold MA, Gulani V, Seiberlich N. Non-Cartesian parallel imaging reconstruction. Journal of Magnetic Resonance Imaging. 2014;40(5):1022-1040. doi: https://doi.org/10.1002/jmri.24521

49. Dydak U, Weiger M, Pruessmann KP, Meier D, Boesiger P. Sensitivity-encoded spectroscopic imaging. Magnetic Resonance in Medicine. 2001;46(4):713-722. doi: https://doi.org/10.1002/mrm.1250

50. Kirchner T, Fillmer A, Tsao J, Pruessmann KP, Henning A. Reduction of voxel bleeding in highly accelerated parallel 1 H MRSI by direct control of the spatial response function: Reduction of Voxel Bleeding in Highly Accelerated MRSI. Magn Reson Med. 2015;73(2):469-480. doi: 10.1002/mrm.25185

51. Lott J, Platt T, Niesporek SC, et al. Corrections of myocardial tissue sodium concentration measurements in human cardiac 23Na MRI at 7 Tesla. Magnetic Resonance in Medicine. 2019;82(1):159-173. doi: https://doi.org/10.1002/mrm.27703

52. Sled JG, Pike GB. Correction for B1 and B0 variations in quantitative T2 measurements using MRI. Magnetic Resonance in Medicine. 2000;43(4):589-593. doi: https://10.1002/(sici)1522-2594 (200004)43: 4<589::aid-mrm14>3.0.co;2-2

Chapter 8

Brain White Matter Fractional Anisotropy and ^{23}Na Concentration: an (Artifactually) Inverse Relationship

Paul Polak M.A.Sc, Michael D. Noseworthy Ph.D, P.Eng

8.1 Context of the Paper

This paper examines the in vivo measurement of TSC in a comparison study with diffusion tensor imaging (DTI). The goal of the study was to examine brain ^{23}Na MRI with ^{1}H DTI, and investigate if there are any correlations between the measurements. Spin-density ^{23}Na would require an excessive long scan time, so a variable flip angle technique is employed to generate spin-density weighted TSC maps from two sodium scans. Regional WM and GM TSC were assessed and compared to FA and CSF proximity. Results indicated that TSC values were increased in voxels proximal areas of CSF, which was likely the result of the broad PSF of ^{23}Na MRI. This is potentially problematic in examining WM pathology, since the densest WM is located proximal to the lateral ventricles. This paper investigated DTI and ^{23}Na MRI correlations, and demonstrated the potential confounding effects of the ^{23}Na PSF.

8.2 Declaration Statement

Paul Polak tuned and matched the RF coil used for the acquisitions, and developed the software for data acquisition, image reconstruction and data analysis. As the first author he wrote the first draft and performed the subsequent corrections and alterations. Michael D. Noseworthy provided the RF coil structure, funding, and is the corresponding author. He also provided essential editing in order to prepare the manuscript for submission.

This work is now prepared and in a final form in order to be submitted as a manuscript for potential publication.

8.3 Paper

Brain White Matter Fractional Anisotropy and ^{23}Na Concentration: an (Artifactually) Inverse Relationship

Paul Polak[1,2], Michael D. Noseworthy[1,2,3,4]

1. *School of Biomedical Engineering, McMaster University, Hamilton, ON, Canada*
2. *Imaging Research Centre, St. Joseph's Healthcare, Hamilton, ON, Canada*
3. *Electrical and Computer Engineering, McMaster University, Hamilton, ON, Canada*
4. *Department of Radiology, McMaster University Hamilton, ON, Canada*

Corresponding Author:
Dr. Michael D. Noseworthy, PhD PEng
Department of Electrical and Computer Engineering
McMaster University
1280 Main Street West., Hamilton, Ontario, Canada. L8S 4K1
VOICE: (905) 525-9140 x23727
EMAIL: nosewor@mcmaster.ca

Running Title: DTI and 23Na MRI

Keywords: 23Na MRI, diffusion imaging, fractional anisotropy, point-spread function

8.3.1 Abbreviations

- ^{23}Na: sodium
- CSF: cerebrospinal fluid
- DA-3DRP: density-adapted 3D radial projections
- DTI: diffusion tensor imaging
- DWI: diffusion weighted imaging
- FA: fractional anisotropy item FOV: field of view
- GM: gray matter
- LR: left and right
- PSF: point-spread function
- ROI: region of interest
- SAR: specific absorption rate
- SNR: signal to noise ratio
- TSC: tissue sodium concentration
- UTE: ultra-short TE
- WM: white matter

8.3.2 Abstract

Purpose

Recognizing sodium's (^{23}Na) indispensable role in human metabolism, ^{23}Na MRI seeks to illuminate its role in pathology. Among the challenges in ^{23}Na MRI is poor signal, often partially mitigated by large voxel sizes and long acquisition times. Diffusion tensor imaging (DTI) is an MRI technique which has been widely adopted, particularly for neurological purposes, and provides a measure of myelin health through the measurement of fractional anisotropy (FA). The techniques provide both structural (DTI) and physiological (^{23}Na) information, which could provide valuable insight into pathology – but only if comparisons to the healthy brain exist. Here we investigate ^{23}Na and diffusion images in a healthy cohort in order to gain insight into their correlates.

Theory and Methods

15 healthy subjects were scanned with a 3 T MRI in accordance with our research ethics board. Tissue sodium concentration (TSC) was determined via a variable flip angle technique, and these were compared to fractional anisotropy (FA) measures from DTI. Images from both techniques were co-registered to the proton T_1 anatomical subject space by a custom methodology. Regional gray and white TSC was assessed in an analysis which compared FA, TSC and cerebrospinal fluid (CSF) proximity.

Results

In corpus callosum regions (body and genu), voxels exhibiting lower FA values displayed higher measured TSC – this effect was most evident in voxels near the lateral ventricles. In gray matter regions distal to CSF this effect was diminished or not apparent. The data indicates partial voluming and sodium point-spread function (PSF) as the potential causes.

Conclusion

A broad point-spread function is common in ^{23}Na MRI and represents a confounding effect when interpreting sodium concentrations. Care must be taken in studies combining suspected pathology and ^{23}Na MRI in areas proximal to sources of dense sodium concentrations.

8.3.3 Introduction

Sodium (^{23}Na) is an essential ion in cellular metabolism, due to its critical role in pH regulation, the Na+K+ ATPase pump, and propagation of action potentials in neurons and muscles [1-4]. For these reasons, in vivo ^{23}Na MRI is intriguing for its potential role in elucidating sodium's role in a variety of neurological conditions, such as multiple sclerosis (MS) [5,6], Alzheimer's disease [7], stroke [8-10], and cancer [11,12]. Unfortunately, ^{23}Na MRI is hampered by many technical challenges, including the requirement of special RF hardware, non-standard (generally ultra-short TE (UTE)) pulse sequences and computationally intensive offline reconstructions. In addition, the low ^{23}Na concentration, compared to proton (^{1}H MRI), a low gyromagnetic ratio and short T_2^* relaxation times result in images with poor signal-to-noise ratios (SNR). The most common remedies (multiple averages, large acquisition voxels) result in long acquisition times and coarse image resolutions. High-field MRI (i.e. ≥ 7 T) has also been used for ^{23}Na MRI, with the associated risk of increased patient heating due to specific absorption rate (SAR) [13].

Diffusion imaging is an established ^{1}H MRI technique used to assess water diffusivity, and has numerous clinical applications in stroke [14], traumatic brain injury [15-17], and multiple sclerosis [18-20]. Diffusion weighted imaging (DWI) requires the acquisition of three orthogonal diffusion directions in order to produce apparent diffusion coefficient maps. The more advanced technique of diffusion tensor imaging (DTI), a rotationally invariant representation of diffusivity, uses a minimum of six directions and can further assess white matter integrity. More recent studies investigated the use of multiple gradient directions and b-values, in order to perform white matter tractography, and assess diffusion kurtosis [21,22]. The applications for brain DTI are too numerous to list, and its efficacy has been detailed across numerous clinical and research studies [23,24].

Combining ^{23}Na MRI and DWI have been used in a limited number of investigations, notably for breast cancer [25,26], uterine fibroids [27] and multiple sclerosis [6]. Recently, DTI and low resolution ^{23}Na images were combined in a traumatic brain injury study [28]. But otherwise there are few studies combining ^{23}Na and DTI for in vivo assessment of human brain, healthy or diseased. Combining both DTI and ^{23}Na MRI could provide valuable insight into brain pathology as they provide quantitative means to assess both structure and physiology. However, to benefit from a combined approach an evaluation of healthy brains is required. In particular an understanding as to how DTI metrics correlate with healthy brain sodium is necessary. In this work we present ^{23}Na and diffusion images and then evaluate the sodium concentrations in relation to DTI measures in the healthy brain.

8.3.4 Methods

In a study approved by our local research board, and in accordance with the Declaration of Helsinki, 15 healthy volunteers (9 male, 6 female, mean age: 33.3yrs, standard deviation: 11.8) were assessed. Following initial screening subjects were instructed to change into a cotton hospital gown in preparation for scanning. Subject weight and height were also recorded.

Imaging was conducted using a 60 cm bore GE 3T MR750 (General Electric Healthcare, Waukesha, WI), having a maximum gradient amplitude and slew rate of 50 mT/m and 200 T/m/s respectively. For ^{23}Na imaging a custom built 16-rung single-tune high-pass quadrature birdcage head coil with resonant frequency of 33.8 MHz was used. Shimming and localization was performed using the proton-tuned body coil. Proton imaging for DTI and 3D T_1 imaging (details below) were performed using a 32 channel head coil from GE Healthcare. Each subject was removed from the scanner between ^{23}Na and ^{1}H imaging components as the hardware was swapped.

Acquisition

The ^{23}Na imaging used the GE MNS Research Pack (v. 2018-07-18) and a 3D density-adapted radial projection (DA-3DRP) sequence [29]. Projections were designed with a 3.2 mm isotropic resolution at a field of view (FOV) of

240 mm [30]. Transmit gain and center frequency calculations were derived semi-automatically from the Bloch-Siegert shift [31]. As a by-product of this process the SNR and ^{23}Na linewidth (in Hz) were calculated. ^{23}Na RF pulse lengths were 600 μs for a volumetric excitation (i.e. hard pulse) and TE was 0.2 ms (UTE sequence). A B_1^+ map sequence was acquired and used to correct the TSC [32], after first being smoothed with a Gaussian filter (width = 6 mm).

TSC spin density and T_1 maps were derived from dual sodium sequences using a variable flip angle technique [33]. Chosen flip angles of 30 and 70 based on the error in the spin density map, while remaining within SAR limits (i.e. $<$ 3 W/kg). Figure 8.1 shows the spin density error versus flip angles.

^1H imaging used a DTI sequence (b=1000 $\mathrm{s \cdot mm^{-2}}$) with 60 directions and 6 b=0 $\mathrm{s \cdot mm^{-2}}$ images. Other sequences included a 3D T_1 weighted, 3D T_2 weighted, and a 6 direction DTI (same acquisition parameters as 60 direction DTI) with reverse phase encoding polarity needed for eddy current corrections (described below). Total MRI acquisition time was approximately 60 minutes, which included overhead for localizer scans, ^{23}Na transmit gain calculations, and proton parallel imaging (i.e. ASSET) calibrations. Acquisition protocol parameters are listed in table 8.1.

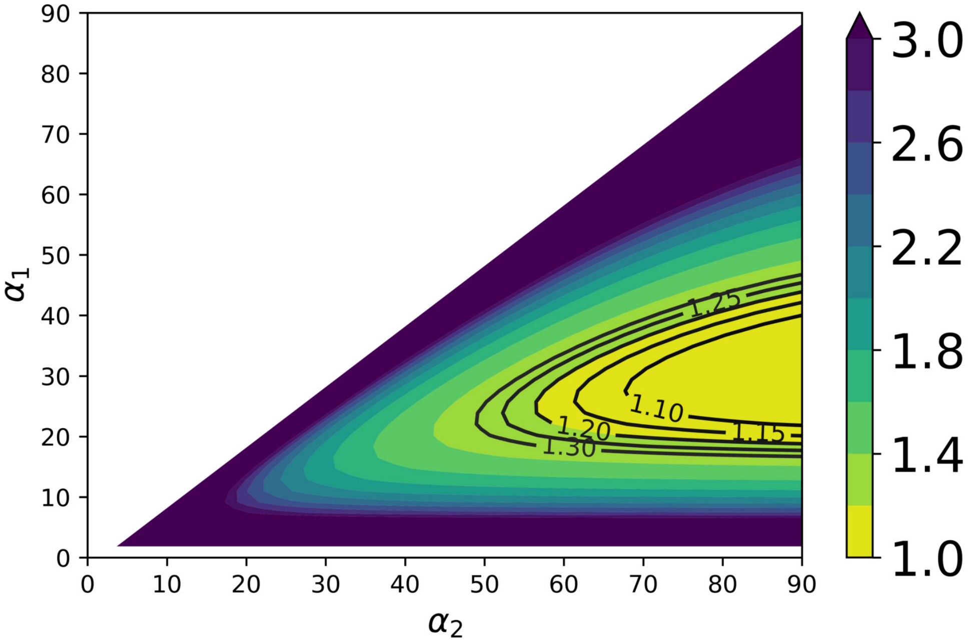

Figure 8.1: Expected noise in the derivation of the spin density TSC in terms of the system noise, σ_S. Choice of flip angles in the range of 0 to 90 degrees. Plot has been normalized to the minimum error. From Sabati et al. [33]:

$$\sigma_{SD} = \frac{A\sqrt{B^2 S_2^4 + C^2 S_1^4}}{KE^*(BS_2 - CS_1)^2}\text{, where}$$

$$\begin{aligned} A &= \sin(\alpha_2)\tan(\alpha_1) - \sin(\alpha_1)tan(\alpha_2) \\ B &= \tan(\alpha_1)\sin(\alpha_1)(\sin(\alpha_2) - tan(\alpha_2)) \\ C &= \tan(\alpha_2)\sin(\alpha_2)(\sin(\alpha_1) - tan(\alpha_1)) \end{aligned}$$

K is a system constant, E* represents the T_2^* decay, α_1 and α_2 the flip angles, and S$_1$ and S$_2$ the signals from the spoiled gradient echo equations for sodium MRI. For this simulation, E* $\approx$ 1 for a UTE pulse sequence, K is set to 1, and S$_1$ and S$_2$ calculated with TR: 24 ms, T_1: 35 ms. The minimum σ_{SD} on this range is for $\alpha_1 = 33$ and $\alpha_2 = 90$.

Sequence	TR (ms)	TE (ms)	TI (ms)	TA (min:sec)	Flip Angle	FOV (mm)	Acquisition Voxel (mm^3)	Notes
^{23}Na								
DA-3DPR	24	0.2	–	10:48	70	240	3.2 × 3.2 × 3.2	13500 projections 2 averages
DA-3DPR	24	0.2	–	10:48	30	240	3.2 × 3.2 × 3.2	13500 projections 2 averages
B_1^+Map	160	0.2	–	3:50	90	240	6.2 × 6.2 × 6.2	FLORET, 3 hubs 120 interleaves / hub
^{1}H								
2D Axial DTI	12000	78	–	13:30	–	240	2.5 × 2.5 × 2.5	60 directions, b = 1000 s·mm^{-2}, 6 b=0 images
2D Axial DTI – reverse polarity	12000	78	–	2:30	–	240	2.5 × 2.5 × 2.5	6 directions, 6 b=0 images
3D sagittal T_1	1200	4.25	450	5:30	12	240	0.47 × 0.94 × 2.0	–
3D sagittal T_2	3000	149	–	7:30	–	240	0.47 × 0.94 × 2.0	–

Table 8.1: MRI protocol details. 2D Axial DTI – reverse polarity has opposite phase encoding to 2D Axial DTI. Abbreviations – DA-3DPR: density-adapted, 3D projection reconstruction; DTI: diffusion tensor imaging; FLORET: Fermat looped orthogonally encoded trajectories; FOV: field of view.

Reconstruction

^{23}Na images were reconstructed from k-space data using the Berkeley Advanced Reconstruction Toolkit [34], with density compensation and regridding, and zerofilled to a resolution of 1 mm (isotropic). An $\ell 1$ wavelet transform was used for noise reduction, before the ^{23}Na and B1+ map images were converted using Python into NIfTI format. Proton images from DTI, 3D T_1 and T_2 weighted scans were converted from DICOM to NIfTI format using dcm2niix (https://github.com/rordenlab/dcm2niix). Eddy current corrections [35] and subsequent DTI processing were conducted using the FSL library [36]. Specifically, the FDT toolbox of FSL was used for DTI processing – this toolbox does not enforce eigenvalue positivity. As a result of image noise or subject motion this can result in calculated eigenvalues < 0, which result in voxel fractional anisotropy (FA) > 1.0, which is not possible. Hence, a minimum eigenvalue constraint of 0 was enforced on all voxels before calculating the FA maps.

Registration

The image processing pipeline for registration of NIfTI images into anatomical T_1 image space is shown in Figure 8.2. All operations used the FSL library except for gradient unwarping of ^{23}Na images [37]. An anatomical 3D T_2 image registered to the 3D T_1 was created in step 1. This co-registered T_2 (labeled 'coreg T2' in figure 8.2) then becomes the reference target for future registrations of the ^{23}Na and DTI images. Susceptibility distortions from the skull / tissue interface produce unwanted effects on the surrounding voxels in the DTI and ^{23}Na data – these effects are mitigated by erosion of the brain mask in step 3 (figure 8.2) such that subsequent analysis excludes these distorted voxels. Brain extractions, registrations, and gradient unwarping operations were verified visually for each subject.

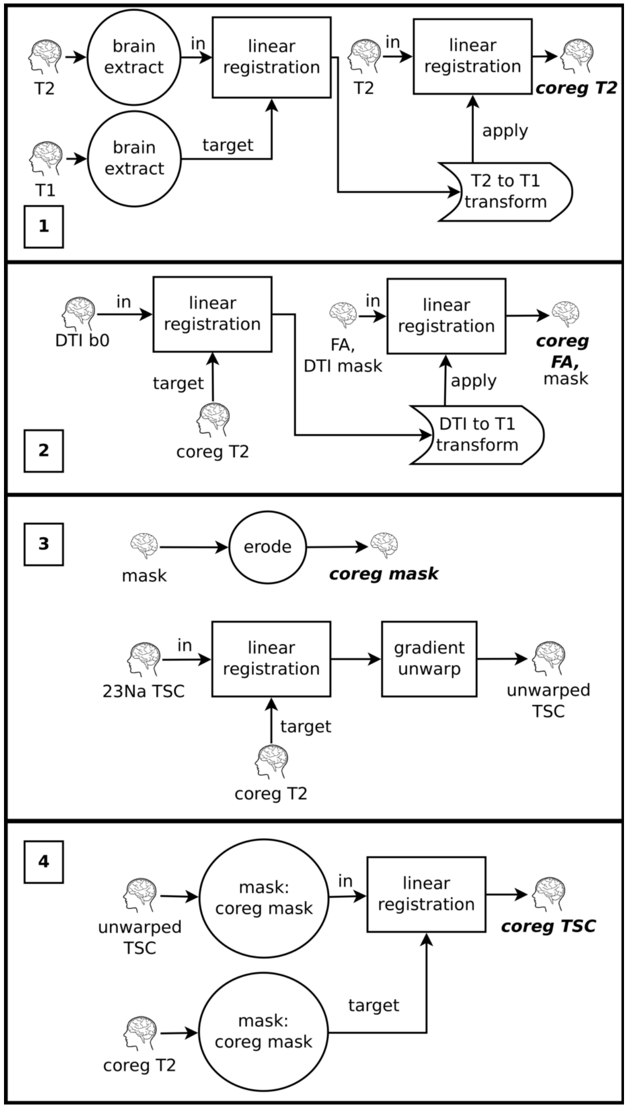

Figure 8.2: Co-registration pipeline of ^{23}Na, DTI and anatomical T_2 images into a common T_1 space. Steps proceeded in order (1-4). DTI processing (eddy correction, reconstruction of FA, and brain mask) and conversion of images into NifTI format are not shown. All processing used the FSL library tools (*bet*, *fslmaths*, *flirt*), except for gradient unwarping. Linear registrations with flirt used rotation and translations only (i.e. six degrees of freedom). Only linear registrations were performed to eliminate potentially erroneous voxel distortions as a consequence of performing registrations with noisy images. ^{23}Na images registered initially (3) before gradient unwarping and then final registration in (4). bet used for brain extraction in step (1). Erosion of the brain mask in (3) conducted to negate effects of local susceptibility artifacts from the skull which produce distortions in the DTI and ^{23}Na data. Images with the brain without surrounding skull represent NIfTI files that have been skull stripped, either through brain extraction, application of a brain mask, or a previous processing step.
Terminology: in: source image; target: reference for the registration; apply: applies a previously calculated registration matrix; coreg: implies a NIfTI file which is registered into common (anatomical T_1) space. Output images are denoted in bold italics.
Abbreviations: DTI: diffusion tensor imaging; FA: fractional anisotropy. Brain graphics in the public domain courtesy of https://clipartix.com.

Analysis

TSC maps in mM were derived from the TSC spin density maps using a two point fit. Regions of interest were drawn on the ^{23}Na images in the vitreus humor and corona radiata. The mean value of each region of interest (ROI) was set to values from the literature (vitreus humor: 140 mM [38,39], corona radiata: 38 mM [40-42]) – these were used to determine the linear fit parameters for the remaining voxels for each subject. FSL, Python, and Matplotlib [43] were used for the analysis and plots.

A brain atlas combining white and gray matter (WM, GM) regions from the Talairach Daemon [44], JHU ICBM-DTI-81 White-Matter [45], and Harvard-Oxford Subcortical Structural [46] atlases was constructed from regions on the Montreal Neurological Institute (MNI) standard brain template. GM regions examined were the left and right (LR) thalami, LR caudates, LR putamen, and LR palladium. WM regions analyzed were the corpus callosum (body and genu), middle cerebellar peduncle, and LR anterior corona radiata. The atlas was warped into the anatomical T_1 space of each subject by the following method: (1) create a warpfield of T_1 to MNI by using a non-linear registration of each subject's T_1 into MNI space, (2) reverse the warpfield to produce an MNI to T_1 space warp, and (3) apply this warping matrix to the atlas. Each binary region of the atlas was slightly eroded (2 voxels) after warping to each subject's space in order to preclude contamination from neighboring regions. This erosion can be justified by taking into consideration the relatively broad point-spread function (PSF) of ^{23}Na imaging and its underlying effects on the effective resolution [47].

In order to analyze any correlation between DTI and ^{23}Na MRI, binary masks were created from the FA maps. These masks subdivided each atlas region into "bins" based on their FA values. Reflecting that WM is expected to be more anisotropic than GM, different ranges were used for the masks. WM regions used bins of FA ≤ 0.2, $0.2 <$ FA ≤ 0.3, $0.3 <$ FA ≤ 0.4 ... FA $>$ 0.8. GM regions used FA ≤ 0.1, $0.1 <$ FA ≤ 0.2 ... FA > 0.4. WM regions with low FA values are due to the effects of partial voluming or crossing fibers [48,49]. Means and standard deviations for TSC were calculated in each atlas region and appropriate (i.e. GM or WM) range of FA masks. In addition, absolute and relative volumes were also calculated.

In an effort to examine the effects stemming from partial voluming and the ^{23}Na PSF, the distance to the nearest cerebrospinal fluid (CSF) voxel was calculated for each voxel in the atlas. CSF voxels determined from tissue segmentation (FSL program fast) of the T_1 images into probabilistic maps of WM, GM and CSF. CSF binary masks were created from the CSF map where the probability of the voxel being CSF was > 0.5.

8.3.5 Results

Figure 8.3 displays representative images from a single subject's 3D T_1, FA, and TSC. Figure 8.4 shows plots of the means and standard deviations of the TSC in mM versus FA bins for GM (a) and WM (b). Relative volumes for each FA bin are indicated by the blue bars. GM TSC is nearly unchanged with respect to FA value – the possible exception in the thalami explained by low voxel counts for FA < 0.2. In the WM regions of the corpus callosum (body and genu), higher TSC values are correlated with lower FA values.

Figure 8.5 indicates the TSC versus both distance to CSF, and FA in the LR thalami (a) and genus of the corpus callosum (b) across all subjects. The lower left corner (i.e. voxels nearest to CSF and having lower FA) of both plots display the highest sodium concentrations. As the voxel distance away from CSF increases, the apparent sodium concentrations decrease to the levels expected in WM and GM. Histograms (FA: above; distance: right) indicate the voxel counts associated with each region. Distance to CSF is quantized, and is evident for short distances – this is visualized as empty lines or "gaps" in the data where acquisition geometry prohibits some values from being possible.

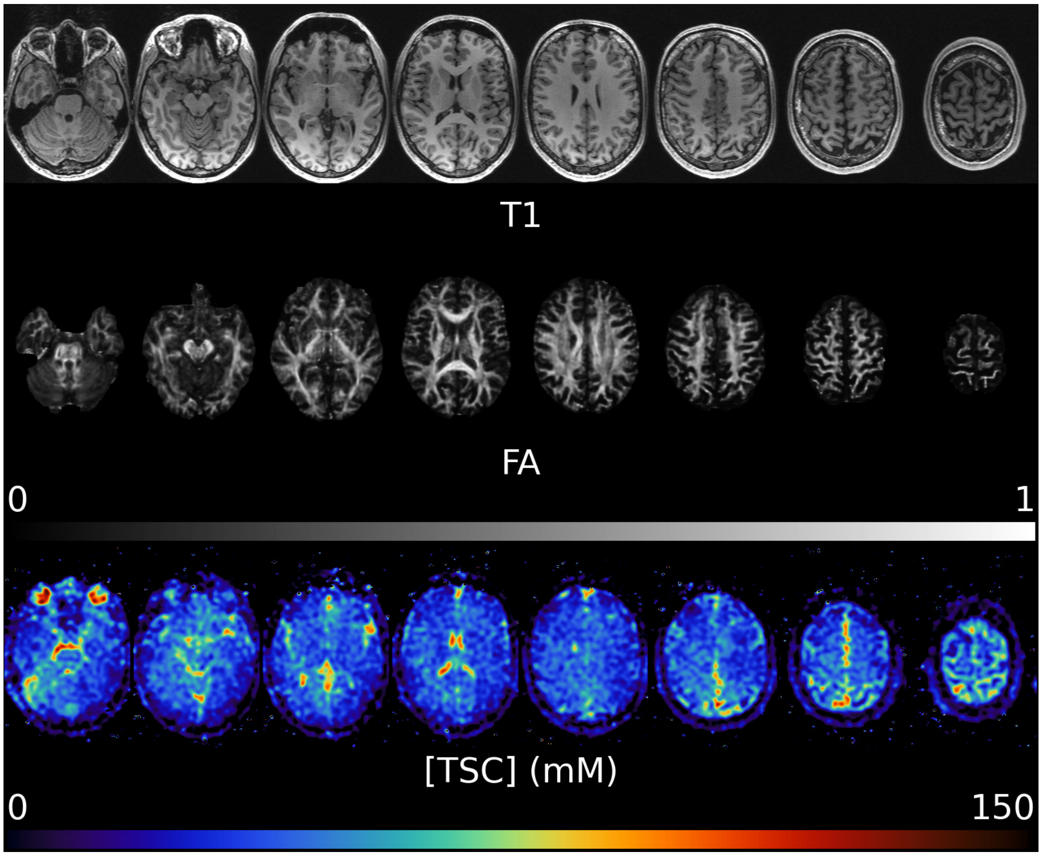

Figure 8.3: Representative slices from one subject with 3D T_1 (top row), FA map (middle row) and ^{23}Na TSC (bottom row). FA range of 0 to 1. TSC range 0 to 150 in mM.
Abbreviations: FA: fractional anisotropy; TSC: tissue sodium concentration.

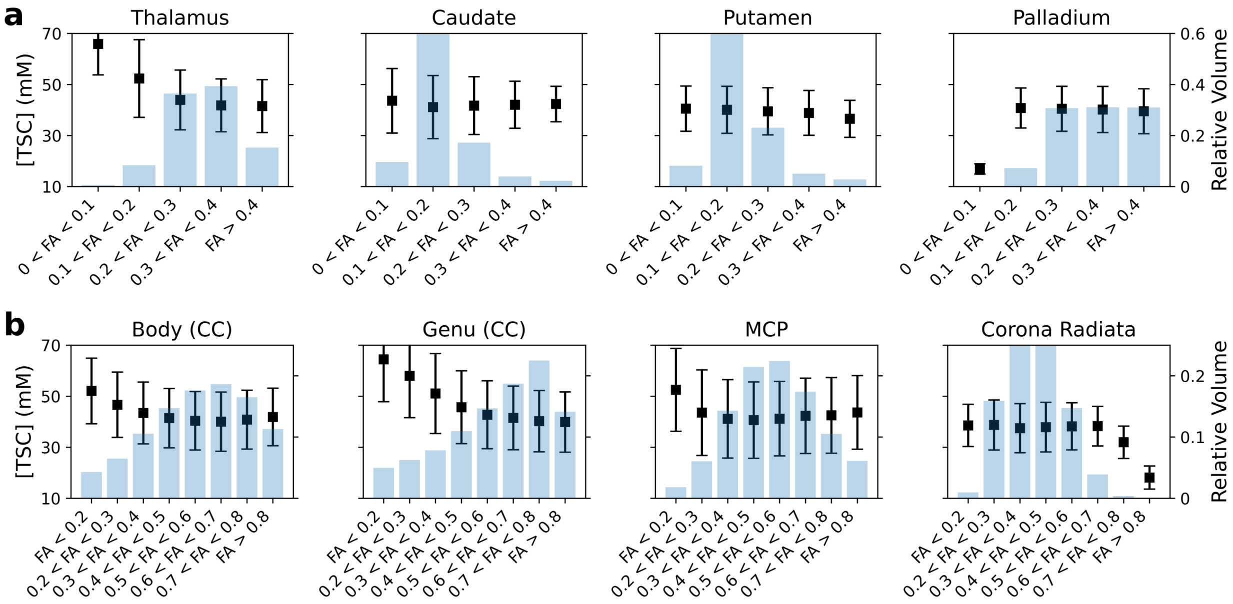

Figure 8.4: Means and standard deviations of TSC (black) in GM (a) and WM (b) regions versus FA for the atlas across all subjects. Relative volumes for each FA bin indicated by blue bar. For the left and right paired structures (thalami, caudates, etc.) the TSC was combined based on the relative volumes in each segment.
Abbreviations: CC: corpus callosum; FA: fractional anisotropy; GM: gray matter; MCP: middle cerebellar peduncle; TSC: tissue sodium concentration; WM: white matter.

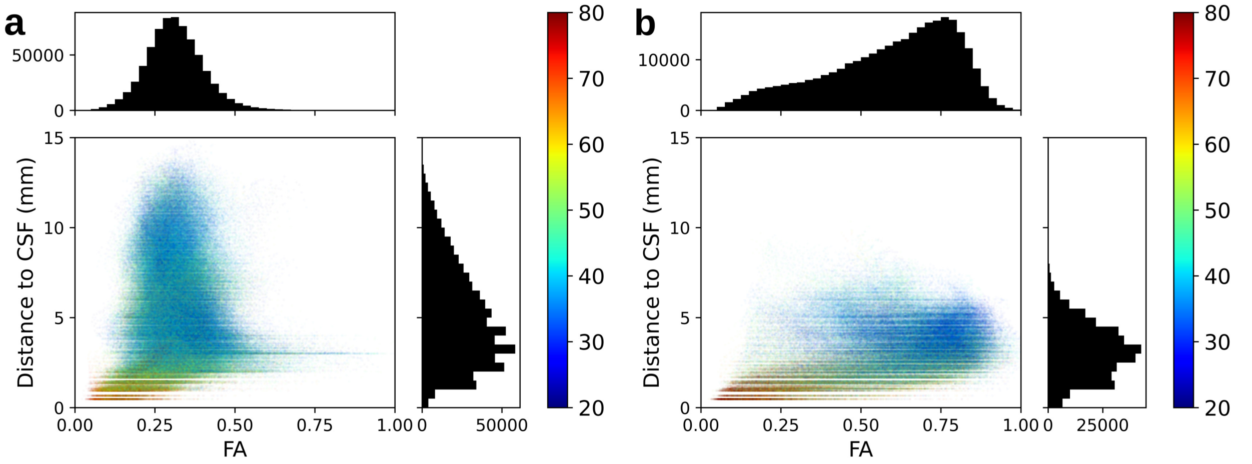

Figure 8.5: TSC versus measured FA and Cartesian distance (mm) to the nearest CSF voxel for all 15 subjects merged. Each point represents a single voxel in subject space for the atlas regions of the (a) left and right thalami and (b) genus of the corpus callosum. TSC colorbar range from 20 to 80 mM. Histograms indicate voxel counts for FA (above) and distance to CSF (right).
Abbreviations: CSF: cerebrospinal fluid; FA: fractional anisotropy; TSC: tissue sodium concentration.

8.3.6 Discussion

^{23}Na MRI remains an enticing prospect for neuroimaging applications; however, the low SNR images can impair their utility. In particular, correlations to other MRI techniques, such as DTI or T_1 tissue segmentation, rely upon accurate co-registrations. Coarse resolutions and poor SNR can impede registrations [48,49], and this necessitated our image processing pipeline as described in figure 8.2. Brain extractions are usually conducted prior to registration to remove the effects of the skull, eyes, etc. from the underlying algorithm in order to concentrate these efforts on the tissue of interest (i.e. brain). Unfortunately, in practice the brain extraction algorithm performed poorly on the ^{23}Na images which led to the methodology adopted here. Other ^{23}Na studies have utilized different methods [6,50,51] to co-register coarse sodium images to higher resolution anatomical images – the ideal method remains an open question for further inquiry, but likely will be tied to the individual study and underlying quality of the ^{23}Na images.

The finding that some voxels show a higher TSC with proximity to CSF corroborates ^{1}H MRI DTI results [52]. DTI measures make the inherent assumption that individual voxels contain only a single tissue type – the partial voluming effects from the CSF in the lateral ventricles result in a mixing of tissue types, and a weighted average of the FA measures [52,53]. A similar effect is likely occurring here with TSC measures where high ^{23}Na concentration is from CSF, combined with the broad point-spread function inherent to ^{23}Na MRI, results in increased measured concentrations around the ventricles. Intuitively this effect is most clearly observed in the body and genu of the corpus callosum. This confounding effect is problematic especially with regards to correlations between ^{23}Na MRI and certain WM pathologies, such as multiple sclerosis and traumatic brain injury. Further, the geometry of the brain structures is critical – large parts of the thalami are located distal to the ventricles (figure 8.5), and these voxels are thus unlikely to be perturbed by the high ^{23}Na concentration in the ventricles. Conversely, corpus callosum structures are more compact and arranged proximal to the lateral ventricles. Once the confounding effects of CSF are taken into account, the TSC values are comparable to those found in the literature.

There is also a PSF associated with the FLORET B_1^+ map, and in our previous work we demonstrated that this PSF was slightly worse than for DA-3DPR [30]; however, as the B_1^+ map is smoothed with a Gaussian filter before its application, the consequences of its broader imaging PSF are minimal. The RF subsystem is independent of the gradients, and thus while the FLORET B1+ sequence samples k-space more efficiently [54], it is assumed that this will have little or no effect upon the resulting B_1^+ map.

The DA-3DPR acquisition was designed to have a 3.2 mm isotropic resolution, which when factored in with the measured point-spread function [30] results in an effective voxel resolution of approximately 6 mm. As the WM corpus callosum structures are within this distance to CSF (figure 8.5), this effect particularly affects these regions. Attempts to increase voxel size in an attempt to alleviate low SNR in ^{23}Na MRI will absolutely exacerbate this effect [47,52,54].

In order to quantify and calibrate the TSC map in units of $mmol/L$, there are two main experimental approaches: external calibration tubes [40,55], and internal references [50]. This study used the latter technique, with the vitreus humor (140 mM) and anterior corona radiata (38 mM) being used as calibration points for the linear ^{23}Na fit. The use of a deep WM structure to use for the calibration was intentional, so as to remove any effects from proximity to the lateral ventricles (figure 8.5). Calibration tubes remain a viable option for these operations, although their placement, usually around the exterior of the subject's head, introduce a dependence upon B1+ homogeneity. Regardless of the calibration method used, correlations between spin density TSC and proximity to CSF remain. However, the reporting of ^{23}Na concentrations in terms of mM in this study are useful for comparisons to other ^{23}Na MRI studies.

This study used two T_1-weighted ^{23}Na acquisition sequences each with a different flip angle in order to reconstruct a ^{23}Na TSC map. To negate the effects of T_1 relaxation using a single sequence would require an increase in TR to 150 ms (or more) in order to remove the T_1 weighting from CSF. This increase in TR would represent a prohibitive increase in ^{23}Na acquisition time for this study (approximately 68 minutes at the same resolution). The trade-off for the multiple flip angle technique is an increase in the noise in the resulting spin density image, with the choice of flip angles (30° and 70°) in this study represented a value for $\sigma_{SD} \approx 1.09$ (figure 8.1). Increasing the flip angle in an attempt to decrease the noise [33] in the spin density image results in an increase in SAR [13]. Coste et al. [40] reported the use of angles of 25° and 55° because of SAR considerations for their study. The choice of 30° and 70° in this study resulted in a scanner reported SAR $< 1.1\ W/kg$ for all subjects – well within clinical limits. None of the subjects reported any adverse effects or experienced noteworthy heating. Increasing the larger flip angle to values > 90° would reduce σ_{SD} further [40]; however, flip angles $\geq$ 90° have been shown to be problematic for ^{23}Na imaging, as residual quadrupolar interactions can act to confound quantification [56]. From the same work Stobbe and Beaulieu indicate that these residual interactions are particularly troublesome in WM regions where the tracts are primarily superior to inferior (i.e. parallel to the main magnetic field). These observations, when added to the observations from this work, act to further complicate ^{23}Na brain quantification, and warrant careful design in future studies.

8.3.7 Conclusions

This study examined the correlations between DTI and ^{23}Na MRI in a healthy population. A method to co-register to the subject T_1 anatomical data was presented and then applied in the analysis of correlation between FA and TSC in gray and white matter tissues. An increased TSC was found for voxels with a low FA and nearest proximity to CSF – as such, this effect was particularly evident in regions nearest the lateral ventricles, such as the corpus callosum. This confounding effect, likely as a result of the broad point-spread function inherent to ^{23}Na MRI, is important to consider when evaluating sodium in brain pathology.

8.3.8 References

1. Rose AM, Valdes R. Understanding the sodium pump and its relevance to disease. Clinical Chemistry. 1994;40(9):1674-1685.

2. Skou JC, Esmann M. The Na, K-ATPase. Journal of Bioenergetics and

Biomembranes. 1992;24(3):249-261. doi:10.1007/BF00768846

3. Rolfe DF, Brown GC. Cellular energy utilization and molecular origin of standard metabolic rate in mammals. Physiological Reviews. 1997;77(3):731-758. doi:10.1152/physrev.1997.77.3.731

4. Koltzenburg M, Yousry T. Magnetic resonance imaging of skeletal muscle. Current Opinion in Neurology. 2007;20(5):595-599. doi: 10.1097/WCO.0b013e3282efc322

5. Waxman SG. Mechanisms of disease: sodium channels and neuroprotection in multiple sclerosis-current status. Nature clinical practice Neurology. 2008;4(3):159-169. doi:10.1038/ncpneuro0735

6. Eisele P, Konstandin S, Szabo K, Ebert A, Roβmanith C, Paschke N, Kerschensteiner M, Platten M, Schoenberg SO, Schad LR, Gass A. Temporal evolution of acute multiple sclerosis lesions on serial sodium (23Na) MRI. Multiple Sclerosis and Related Disorders. 2019;29:48-54. doi:10.1016/j.msard.2019.01.027

7. Mellon EA, Pilkinton DT, Clark CM, Elliott MA, Witschey WR, Borthakur A, Reddy R. Sodium MR Imaging Detection of Mild Alzheimer Disease: Preliminary Study. American Journal of Neuroradiology. 2009;30(5):978-984. doi:10.3174/ajnr.A1495

8. Thulborn KR, Davis D, Snyder J, Yonas H, Kassam A. Sodium MR Imaging of Acute and Subacute Stroke for Assessment of Tissue Viability. Neuroimaging Clinics of North America. 2005;15(3):639-653. doi:10.1016/j.nic.2005.08.003

9. Tsang A, Stobbe RW, Asdaghi N, Hussain MS, Bhagat YA, Beaulieu C, Emery D, Butcher KS. Relationship between sodium intensity and perfusion deficits in acute ischemic stroke. Journal of Magnetic Resonance Imaging. 2011;33(1):41-47. doi:10.1002/jmri.22299

10. Boada FE, Qian Y, Nemoto E, Jovin T, Jungreis C, Jones SC, Weimer J, Lee V. Sodium MRI and the Assessment of Irreversible Tissue Damage During Hyper-Acute Stroke. Translational Stroke Research. 2012;3(2):236-245. doi:10.1007/s12975-012-0168-7

11. Ouwerkerk R, Bleich KB, Gillen JS, Pomper MG, Bottomley PA. Tissue sodium concentration in human brain tumors as measured with 23Na MR imaging. Radiology. 2003;227(2):529-537. doi:10.1148/radiol.2272020483

12. Nagel AM, Bock M, Hartmann C, Gerigk L, Neumann J-O, Weber M-A, Bendszus M, Radbruch A, Wick W, Schlemmer H-P, Semmler W, Biller A. The Potential of Relaxation-Weighted Sodium Magnetic Resonance Imaging as Demonstrated on Brain Tumors. Investigative Radiology. 2011;46(9):539-547. doi:10.1097/RLI.0b013e31821ae918

13. Stobbe R, Beaulieu C. Sodium imaging optimization under specific absorption rate constraint. Magnetic Resonance in Medicine. 2008;59(2):345-355. doi:10.1002/mrm.21468

14. Beauchamp NJ, Ulug AM, Passe TJ, van Zijl PC. MR diffusion imaging in stroke: review and controversies. RadioGraphics. 1998;18(5):1269-1283. doi:10.1148/radiographics.18.5.9747619

15. Sasaki T, Pasternak O, Mayinger M, Muehlmann M, Savadjiev P, Bouix S, Kubicki M, Fredman E, Dahlben B, Helmer KG, Johnson AM, Holmes JD, Forwell L a, Skopelja EN, Shenton ME, Echlin PS, Koerte IK. Hockey Concussion Education Project, Part 3. White matter microstructure in ice hockey players with a history of concussion: a diffusion tensor imaging study. Journal of neurosurgery. 2014;120(4):882-890. doi:10.3171/2013.12.JNS132092

16. Polak P, Leddy JJ, Dwyer MG, Willer B, Zivadinov R. Diffusion Tensor Imaging Alterations in Patients With Postconcussion Syndrome Undergoing Exercise Treatment. Journal of Head Trauma Rehabilitation. 2015;30(2):E32-E42. doi:10.1097/HTR.0000000000000037

17. Stillo D, Danielli E, Ho RA, DeMatteo C, Hall GB, Bock NA, Connolly JF, Noseworthy MD. Localization and Identification of Brain Microstructural Abnormalities in Paediatric Concussion. Front Hum Neurosci. 2021;15. doi:10.3389/fnhum.2021.657374

18. Filippi M, Rocca M. MR imaging of multiple sclerosis. Radiology. 2011;259(3):659-681.

19. Aliotta R, Cox JL, Donohue K, Weinstock-Guttman B, Yeh EA, Polak P, Dwyer MG, Zivadinov R. Tract-based spatial statistics analysis of diffusion-tensor imaging data in pediatric- and adult-onset multiple sclerosis. Human brain mapping. 2012;000. doi:10.1002/hbm.22148

20. Klistorner A, Wang C, Yiannikas C, Graham SL, Parratt J, Barnett MH. Progressive Injury in Chronic Multiple Sclerosis Lesions Is Gender-

Specific: A DTI Study. PLOS ONE. 2016;11(2):e0149245. doi:10.1371/journal.pone.0149245

21. Essayed WI, Zhang F, Unadkat P, Cosgrove GR, Golby AJ, O'Donnell LJ. White matter tractography for neurosurgical planning: A topography-based review of the current state of the art. NeuroImage: Clinical. 2017;15:659-672. doi:10.1016/j.nicl.2017.06.011

22. Wu EX, Cheung MM. MR diffusion kurtosis imaging for neural tissue characterization. NMR in Biomedicine. 2010;23(7):836-848. doi: https://doi.org/10.1002/nbm.1506

23. Raja R, Rosenberg G, Caprihan A. Review of diffusion MRI studies in chronic white matter diseases. Neuroscience Letters. 2019;694:198-207. doi:10.1016/j.neulet.2018.12.007

24. Asken BM, DeKosky ST, Clugston JR, Jaffee MS, Bauer RM. Diffusion tensor imaging (DTI) findings in adult civilian, military, and sport-related mild traumatic brain injury (mTBI): a systematic critical review. Brain Imaging and Behavior. 2018;12(2):585-612. doi:10.1007/s11682-017-9708-9

25. Zaric O, Pinker K, Zbyn S, Strasser B, Robinson S, Minarikova L, Gruber S, Farr A, Singer C, Helbich TH, Trattnig S, Bogner W. Quantitative Sodium MR Imaging at 7 T: Initial Results and Comparison with Diffusion-weighted Imaging in Patients with Breast Tumors. Radiology. 2016;280(1):39-48. doi:10.1148/radiol.2016151304

26. Jacobs MA. Multiparametric Magnetic Resonance Imaging of Breast Cancer. Journal of the American College of Radiology. 2009;6(7):523-526. doi:10.1016/j.jacr.2009.04.006

27. Jacobs MA, Ouwerkerk R, Kamel I, Bottomley PA, Bluemke DA, Kim HS. Proton, diffusion-weighted imaging, and sodium (23Na) MRI of uterine leiomyomata after MR-guided high-intensity focused ultrasound: A preliminary study. Journal of Magnetic Resonance Imaging. 2009;29(3):649-656. doi:https://doi.org/10.1002/jmri.21677

28. Chen, AM, Gerhalter, T, Dehkharghani, S, Peralta, R, Adiparvar, F, Babb, JS, Bushnik, T, Silver, JM, Im, BS, Wall, SP, Brown, R, Baete, S, Kirov, II, Madelin, G. Quantitative sodium and diffusion imaging of mild traumatic brain injury: regional analysis ndings. In: Proceedings of the 2021 ISMRM & SMRT Annual Meeting Exhibition. ; 2021.

29. Nagel AM, Laun FB, Weber M-A, Matthies C, Semmler W, Schad LR. Sodium MRI using a density-adapted 3D radial acquisition technique. Magnetic Resonance in Medicine. 2009;62(6):1565-1573. doi:10.1002/mrm.22157

30. Polak P, Schulte RF, Noseworthy MD. An approach to evaluation of the point-spread function for 23Na magnetic resonance imaging. NMR in Biomedicine. 2022;35(2):e4627. doi:10.1002/nbm.4627

31. Schulte RF, Sacolick L, Deppe MH, Janich MA, Schwaiger M, Wild JM, Wiesinger F. Transmit gain calibration for nonproton MR using the Bloch–Siegert shift. NMR in Biomedicine. 2011;24(9):1068-1072.

doi:10.1002/nbm.1657

32. Wang HZ, Riederer SJ, Lee JN. Optimizing the precision in T1 relaxation estimation using limited flip angles. Magnetic Resonance in Medicine. 1987;5(5):399-416.
doi: https://doi.org/10.1002/mrm.1910050502

33. Sabati M, Maudsley AA. Fast and high-resolution quantitative mapping of tissue water content with full brain coverage for clinically-driven studies. Magnetic Resonance Imaging. 2013;31(10):1752-1759. doi:10.1016/j.mri.2013.08.001

34. Uecker M, Ong F, Tamir JI, Bahri D, Virtue P, Cheng JY, Zhang T, Lustig M. Berkeley Advanced Reconstruction Toolbox. In: Proc Intl Soc Mag Reson Med. ; 2015:2486.

35. Andersson JLR, Sotiropoulos SN. An integrated approach to correction for off-resonance effects and subject movement in diffusion MR imaging. NeuroImage. 2016;125:1063-1078.
doi:10.1016/j.neuroimage.2015.10.019

36. Smith SM, Jenkinson M, Woolrich MW, Beckmann CF, Behrens TEJ, Johansen-berg H, Bannister PR, Luca MD, Drobnjak I, Flitney DE, Niazy RK, Saunders J, Vickers J, Zhang Y, Stefano ND, Brady JM, Matthews PM, De Luca M, De Stefano N. Advances in functional and structural MR image analysis and implementation as FSL. NeuroImage. 2004;23 Suppl 1:S208-19. doi:10.1016/j.neuroimage.2004.07.051

37. Polak P, Zivadinov R, Schweser F. Gradient Unwarping for Phase Imaging and QSM. In: Quantitative Susceptibility Mapping (2015). ; 2015:1.

38. Garner WH, Hilal SK, Lee SW, Spector A. Sodium-23 magnetic resonance imaging of the eye and lens. Proceedings of the National Academy of Sciences. 1986;83(6):1901-1905. doi:10.1073/pnas.83.6.1901

39. Boicelli CA, Giuliani AM. Sodium ion distribution in the vitreous body. MAGMA. 1996;4(3-4):241-245. doi:10.1007/BF01772012

40. Coste A, Boumezbeur F, Vignaud A, Madelin G, Reetz K, Le Bihan D, Rabrait-Lerman C, Romanzetti S. Tissue sodium concentration and sodium T1 mapping of the human brain at 3 T using a Variable Flip Angle method. Magnetic Resonance Imaging. 2019;58:116-124. doi:10.1016/j.mri.2019.01.015

41. Madelin G, Kline R, Walvick R, Regatte RR. A method for estimating intracellular sodium concentration and extracellular volume fraction in brain in vivo using sodium magnetic resonance imaging. Scientific Reports. 2014;4:1-7. doi:10.1038/srep04763

42. Thulborn K, Lui E, Guntin J, Jamil S, Sun Z, Claiborne TC, Atkinson IC. Quantitative sodium MRI of the human brain at 9.4 T provides assessment of tissue sodium concentration and cell volume fraction during normal aging. NMR in Biomedicine. 2016;29(2):137-143. doi:10.1002/nbm.3312

43. Hunter J. Matplotlib: A 2D graphics environment. Computing in Science & Engineering. 2007;9(3):90-95. doi:10.1109/MCSE.2007.55

44. Lancaster JL, Tordesillas-Gutiérrez D, Martinez M, Salinas F, Evans A, Zilles K, Mazziotta JC, Fox PT. Bias between MNI and Talairach coordinates analyzed using the ICBM-152 brain template. Human Brain Mapping. 2007;28(11):1194-1205. doi:https://doi.org/10.1002/hbm.20345

45. Mori S, Wakana S, Nagae-Poetscher LM, van Zijl PCM, eds. MRI Atlas of Human White Matter. 1. ed. Elsevier; 2005.

46. Frazier JA, Chiu S, Breeze JL, Makris N, Lange N, Kennedy DN, Herbert MR, Bent EK, Koneru VK, Dieterich ME, Hodge SM, Rauch SL, Grant PE, Cohen BM, Seidman LJ, Caviness VS, Biederman J. Structural Brain Magnetic Resonance Imaging of Limbic and Thalamic Volumes in Pediatric Bipolar Disorder. AJP. 2005;162(7):1256-1265. doi:10.1176/appi.ajp.162.7.1256

47. Niesporek SC, Hoffmann SH, Berger MC, Benkhedah N, Kujawa A, Bachert P, Nagel AM. Partial volume correction for in vivo 23 Na-MRI data of the human brain. NeuroImage. 2015;112:353-363. doi:10.1016/j.neuroimage.2015.03.025

48. Alexander AL, Hasan KM, Lazar M, Tsuruda JS, Parker DL. Analysis of partial volume effects in diffusion-tensor MRI. Magnetic Resonance in Medicine. 2001;45(5):770-780. doi:https://doi.org/10.1002/mrm.1105

49. Metzler-Baddeley C, O'Sullivan MJ, Bells S, Pasternak O, Jones DK. How and how not to correct for CSF-contamination in diffusion MRI. NeuroImage. 2011;59(2):1394-1403. doi:10.1016/j.neuroimage.2011.08.043

50. Robinson D, Milanfar P. Fundamental performance limits in image registration. IEEE Transactions on Image Processing. 2004;13(9).

51. Ou Y, Akbari H, Bilello M, Da X, Davatzikos C. Comparative Evaluation of Registration Algorithms in Different Brain Databases With Varying Difficulty: Results and Insights. IEEE Transactions on Medical Imaging. 2014;33(10):2039-2065. doi:10.1109/TMI.2014.2330355

52. Gerhalter T, Chen AM, Dehkharghani S, Peralta R, Adlparvar F, Babb JS, Bushnik T, Silver JM, Im BS, Wall SP, Brown R, Baete SH, Kirov II, Madelin G. Global decrease in brain sodium concentration after mild traumatic brain injury. Brain Communications. 2021;3(fcab051). doi:10.1093/braincomms/fcab051

53. Syeda W, Blunck Y, Kolbe S, Cleary JO, Johnston LA. A continuum of components: Flexible fast fraction mapping in sodium MRI. Magnetic Resonance in Medicine. 2019;81(6):3854-3864. doi:10.1002/mrm.27659

54. Pipe JG, Zwart NR, Aboussouan EA, Robison RK, Devaraj A, Johnson KO. A new design and rationale for 3D orthogonally oversampled k-space trajectories. Magnetic Resonance in Medicine. 2011;66(5):1303-1311. doi: 10.1002/mrm.22918

55. Atkinson IC, Lu A, Thulborn KR. Preserving the accuracy and resolution of the sodium bioscale from quantitative sodium MRI during intra-subject alignment across longitudinal studies. Magnetic Resonance in Medicine. 2012;68(3):751-761. doi:https://doi.org/10.1002/mrm.23285

56. Inglese M, Madelin G, Oesingmann N, Babb JS, Wu W, Stoeckel B, Herbert J, Johnson G. Brain tissue sodium concentration in multiple sclerosis: A sodium imaging study at 3 tesla. Brain. 2010;133(3):847-857. doi:10.1093/brain/awp334

57. Stobbe RW, Beaulieu C. Residual quadrupole interaction in brain and its effect on quantitative sodium imaging: Residual Quadrupole Interactions Affect Sodium MRI of the Human Brain. NMR in Biomedicine. 2016;29(2):119-128. doi:10.1002/nbm.3376

Chapter 9

Summary and Conclusions

Despite the challenges surrounding ^{23}Na MRI, it remains an enticing area for research, because of its potential applicability in a variety of pathologies [49]. Approximately 50% of the brain's oxygen use is for non-service purposes [3] – that is, energy use for the purpose of maintaining brain tissue, rather than in service to the entire body. Given the importance of the $Na^{+}K^{+}{-}ATPase$ in healthy cellular metabolism [1, 2], this only underlines the desirability of ^{23}Na brain MRI as an interesting technique, and highlights the need for robust methods in this area. This chapter summarizes the contributions made in this dissertation, and suggests research into new areas in order to further the development of ^{23}Na MRI towards clinical use.

9.1 Contributions

- ^{23}Na MRI is SNR limited – This can be significantly modulated by going to a higher magnetic field, B_0. This is a very costly, and in many cases impractical solution. Thus, in order to rectify this, either larger voxels or longer acquisition times are employed. In terms of k-space sampling efficiency, FLORET sequences are superior to projection methods such as DA-3DPR. This efficiency can be exploited to reduce scan times in ^{1}H MRI because signal is plentiful; however, ^{23}Na MRI is signal deficient. Thus, in terms of total acquisition time the choice between DA-3DPR and FLORET matters less because the latter may need high signal averaging in order to recover SNR. In fact, DA-3DPR could be considered superior for ^{23}Na MRI, because the hardware gradient demands (i.e. maximum gradient and slew rate) are less than for FLORET.

- The PSF is an important metric for any imaging system. The underlying PSF of an imaging system is "fixed", although measurement of that PSF can be complicated by the noise we expect to have in ^{23}Na MRI. Of the two methodologies tested, the Fourier harmonic method proved less susceptible to error in the MTF calculations. This work also demonstrated the usefulness and convenience of a 3D-printed phantom in the evaluation of the PSF, and also demonstrates the effective resolution the system will have for in vivo brain MRI.

- DTI can provide information regarding brain tissue structure, and in particular has been used to assess axonal integrity in WM. ^{23}Na MRI provides complementary information; however, care must be taken when measuring ^{23}Na proximal to CSF, as the latter may be confounding the measurement of TSC. This is particularly troublesome in the corpus callosum, as this dense WM tissue is near the lateral ventricles.

9.2 Future Research

In terms of future research into brain ^{23}Na MRI methods, there are a number of areas of promise. While pulse sequence selection is unlikely to be fruitful, the use of a multi-channel receive array could provide great benefit for ^{23}Na acquisitions [111,112]. Lakshmanan et al. [113] reported an increase in signal from 1.6 (center of the head) to 2.3 (periphery) – a significant improvement over a single-channel transmit/receive birdcage design. In addition, using a multi-channel array would have added benefits especially in regards to image reconstruction and the use of compressed sensing techniques [114–116]. This work used compressed sensing techniques to eliminate some noise in the in vivo brain images, but the limitations of a single-channel RF coil (figure 4.1) made these efforts fairly rudimentary. A more sophisticated receiver array could provide a great benefit to ^{23}Na image quality.

In the process of obtaining in vivo brain images in chapter 8, the Bloch-Siegert shift [98] was exploited in order to tune the RF transmit gains and center frequencies. Part of this calibration included the calculation of the SNR – iterations were completed when the SNR reached a maximum for the current subject. Plotting the resulting SNR versus body mass index (BMI) (see figure 9.1) revealed an interesting trend of decreasing SNR with increased BMI, to the extent that a decrease of $\approx 33\%$ was noted between the best and worst cases. The coil used for these studies was tuned and matched at 50 Ω to a single subject, but coil loading can have a significant effect on the resultant SNR. Tuning and matching the coil to individual subjects is rarely performed for human ^{1}H or X-nuclei MRI, but is regularly practiced with preclinical animal work [117, 118]. A mechanism to automatically or semi-automatically tune the ^{23}Na RF coil to the individual subject would provide a great boost in SNR [119, 120].

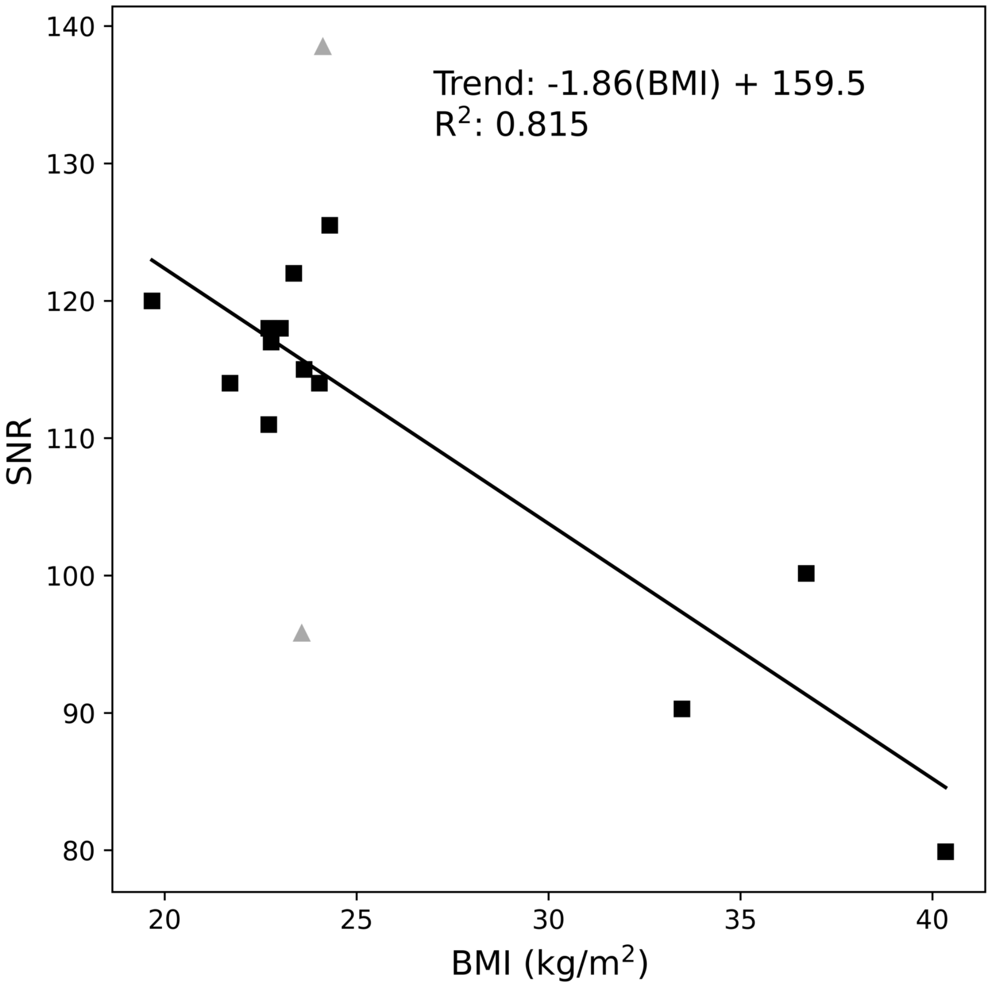

Figure 9.1: Measured prescan SNR versus BMI (in kg/m^2) for all subjects. Two subjects (gray triangles) were excluded as outliers in a Bonferroni test. Linear trend line calculated from remaining data with R^2: 0.815.

9.3 Conclusions

This work demonstrated methods to obtain brain images for ^{23}Na MRI. Sodium plays an integral role in brain metabolism, and ^{23}Na MRI would be an invaluable tool in the diagnosis and prognosis of various pathologies, including MS, stroke, epilepsy and cancer. Translation of ^{23}Na MRI into clinical routine has thus far been impeded by hardware and software requirements, low SNR and the resulting long acquisition times. The potential of using higher strength magnets (i.e. 7 T), and more sophisticated RF receiver circuitry could help allay these problems, and finally bring the potential of ^{23}Na into clinical practice.

Appendix A

Appendix

This appendix to the dissertation outlines the image reconstruction processes used for the data, and will include the raw ^{23}Na images, generation of the B_1^+ maps, and the final ^{23}Na TSC images.

We will use the following example files in the following sections to illustrate the ^{23}Na TSC reconstruction procedure:

- The GE raw data file (i.e. "p-file") for the DA-3DPR acquisition is `43008`.
- The p-file for the B_1^+ acquisition is `43520`.
- DA-3DPR trajectory is in the BART format, and is: `3DPR-13500`.
- FLORET trajectory, also in BART format is: `FLORET-B1MAP`.
- The density compensation functions for the above trajectories are: `3DPR-13500-DCF` and `FLORET-B1MAP-DCF` respectively.

- The MRI acquisition has two ^{23}Na acquisitions (see table 8.1) – the NIFTI files relating to the two flip angles will be called `70.nii.gz` and `30.nii.gz` for angles 70° and 30° respectively.

A.1 ^{23}Na TSC image reconstruction process

1. Extract k-space data from GE raw data format (i.e. p-file) and put into BART format – the output is named: `43008-data`.

   ```
   python readpfiles.py --npts 1000 --average 2 43008
   ```

   The author has found better results with computing signal averaging post-acquisition, rather than letting the system do it at acquisition time – the latter can result in receiver gain overflow.

2. Use the BART toolbox to reconstruct the data using the NUFFT. We first correct for off-isocenter delay times, then weight the data using the density compensation function, before feeding this data into the NUFFT. We reconstruct the image to 240 × 240 × 240 voxels.

   ```
   python shiftkspace.py 43008-data 3DPR-13500 0 -0.1 0
   bart fmac 3DPR-13500-DCF 43008-data-shift 43008-shift_w
   bart nufft -d 240:240:240 3DPR-13500 43008-shift_w 43008-adj
   ```

3. Use a simple compressed sensing thresholding technique in the wavelet domain to reduce image noise.

   ```
   bart cdf97 7 43008-adj 43008-wave
   bart threshold 2e8 43008-wave 43008-wave_thr
   bart cdf97 -i 8 43008-wave_thr 43008-cs
   ```

4. Convert the BART imaging data to NIFTI file format with a resolution of 1.0 mm and an axial acquisition plane.

```
python cfl2nifti.py new -r 1 -p ax 43008-cs 43008-adj.nii.gz
```

5. First co-registering the 70° image to the 30° image using FSL, and then create the TSC using the two flip angles and the TR of 24 ms. The output of the final command creates a TSC NIFTI image: `TSC.nii.gz` and a T_1 map: `T1Map.nii.gz` in ms. The TSC map is proton density weighted, and can be scaled appropriately to a value in mM if desired.

```
flirt -in 70.nii.gz -ref 30.nii.gz S70_30.nii.gz
python makeTSC.py S70_30.nii.gz 70 30.nii.gz 30 24
```

A.2 ^{23}Na B_1^+ map reconstruction process

1. Extract data from p-file with extra argument for processing the Bloch-Siegert (BLOSI) pulses. This creates three output files: `43520-data+` and `43520-data-` respectively for the positive and negative BLOSI arms respectively, and a Python "pickle" file which contains the details of the acquisition.

```
python readpfiles.py --blosi --npts 5032 --average 4 43520
```

2. Shift k-space, multiply by the density compensation function, and reconstruct into complex images.

```
python shiftkspace.py --blosi 43520-data FLORET-B1MAP 0 -0.1 0
bart fmac FLORET-B1MAP-DCF+ 43520-data-shift+ 43520-shift_w+
```

```
bart fmac FLORET-B1MAP-DCF- 43520-data-shift- 43520-shift_w-
bart nufft -a -d 240:240:240 FLORET-B1MAP+
  43520-shift_w+ 43520-adj+
bart nufft -a -d 240:240:240 FLORET-B1MAP-
  43520-shift_w- 43520-adj-
```

3. Create the B_1^+ map and convert to NIFTI format.

```
python createB1Map.py --phasecor . 43520-adj+ 43520-adj-
  blosi.pickle
python cfl2nifti.py new -r 1 -r ax B1Map-smooth B1Map.nii.gz
```

4. `B1Map.nii.gz` can now be co-registered to the same image space as the TSC map, and is called: `coreg_B1+_uT.nii.gz` since it is scaled in units of μT. We can normalize this map by calculating the average value in some region (i.e. binary mask of the brain) and then scaling this appropriately with FSL.

```
mean=‘fslstats coreg_B1+_uT -k mask -M‘
fslmaths coreg_B1+_uT -div ${mean} coreg_B1+_norm
```

5. This normalized B_1^+ map can now be used to correct the ^{23}Na TSC and T_1 map images as per [121].

A.3 Exemplary ^{23}Na images

The following figures display exemplary images from one subject from the data in Chapter 8. Figures include raw ^{23}Na images (70° and 30° flip angles),

B_1^+ map in μT, T_1 map in ms, and TSC map in mM. Images are from the same locations in the brain.

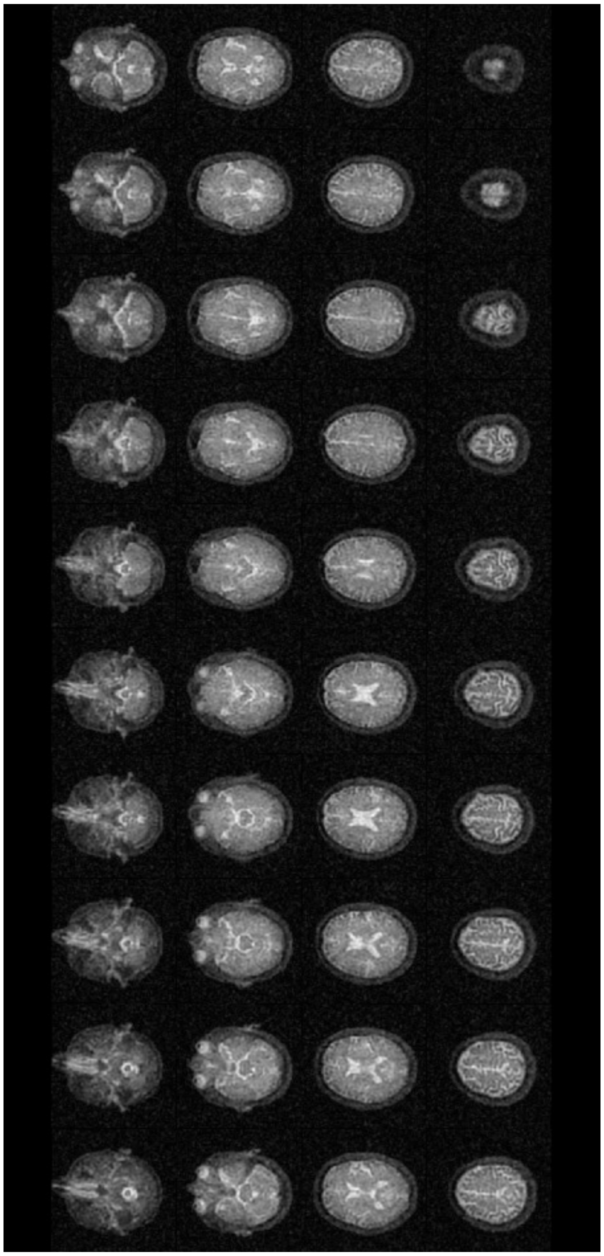

Figure A.1: ^{23}Na raw images from a 70°flip angle.

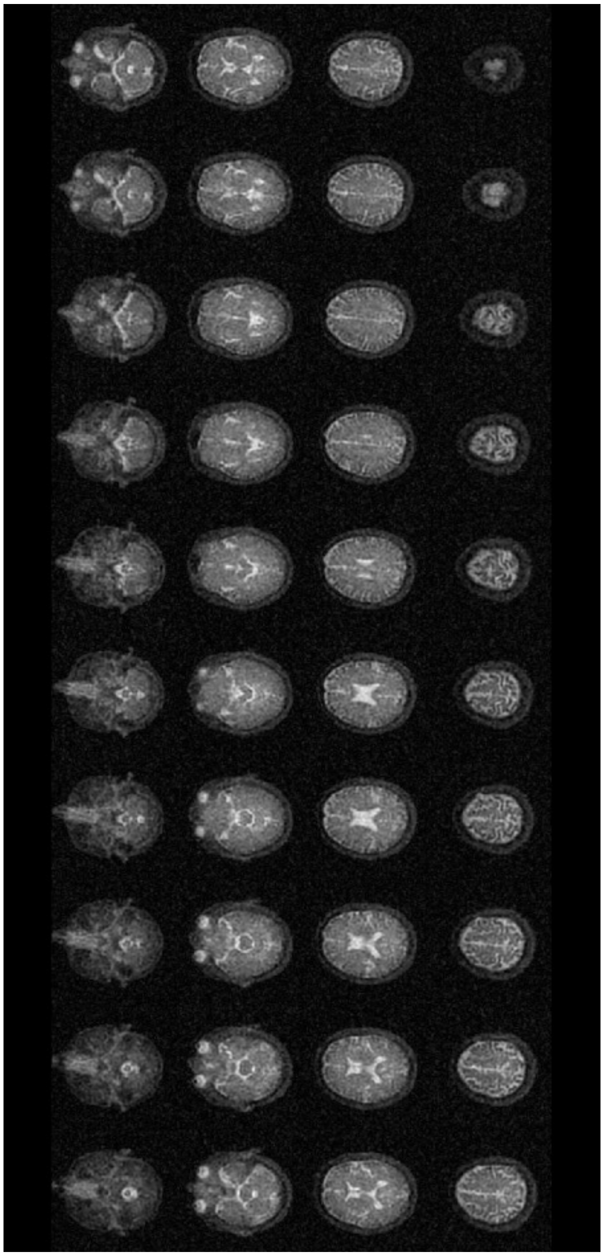

Figure A.2: ^{23}Na raw images from a 30°flip angle.

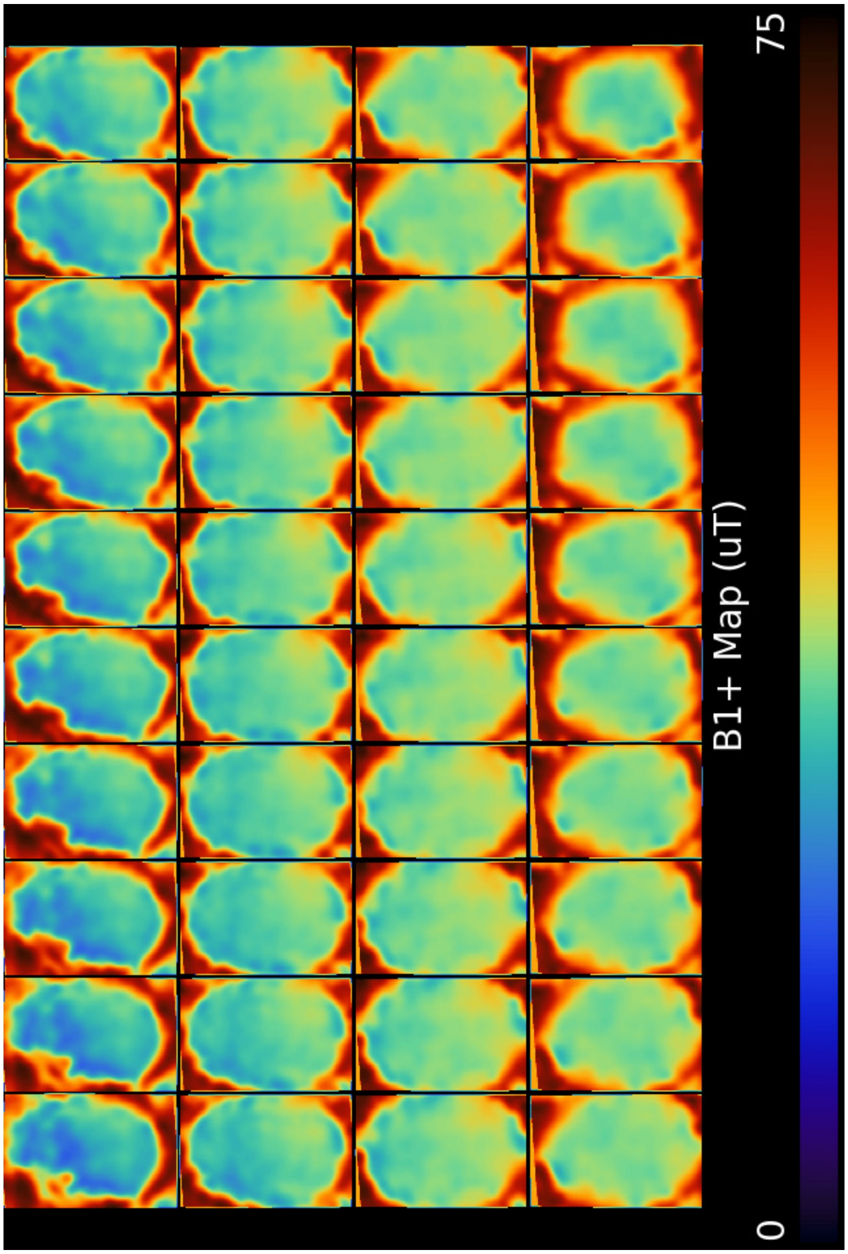

Figure A.3: ^{23}Na B_1^+ map in μT calculated from Bloch-Siegert pulses.

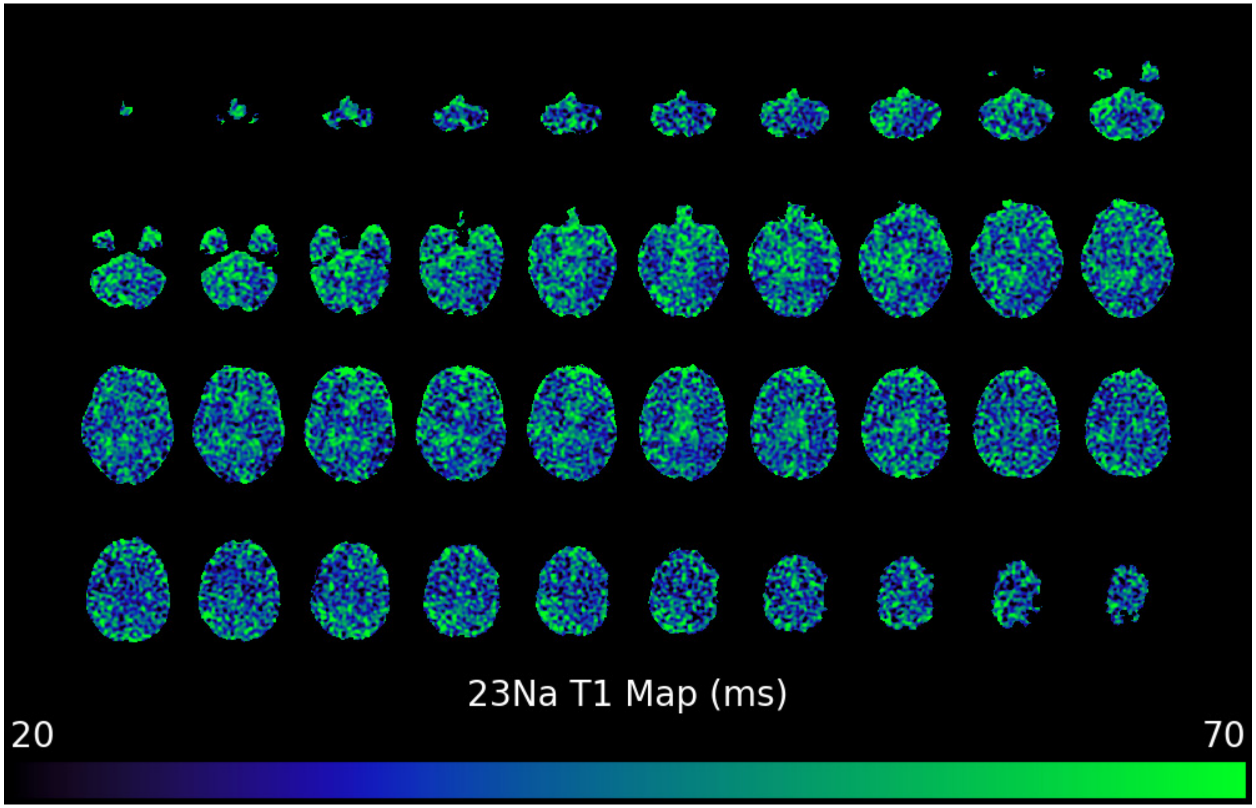

Figure A.4: ${}^{23}Na$ T_1 map, measured in ms.

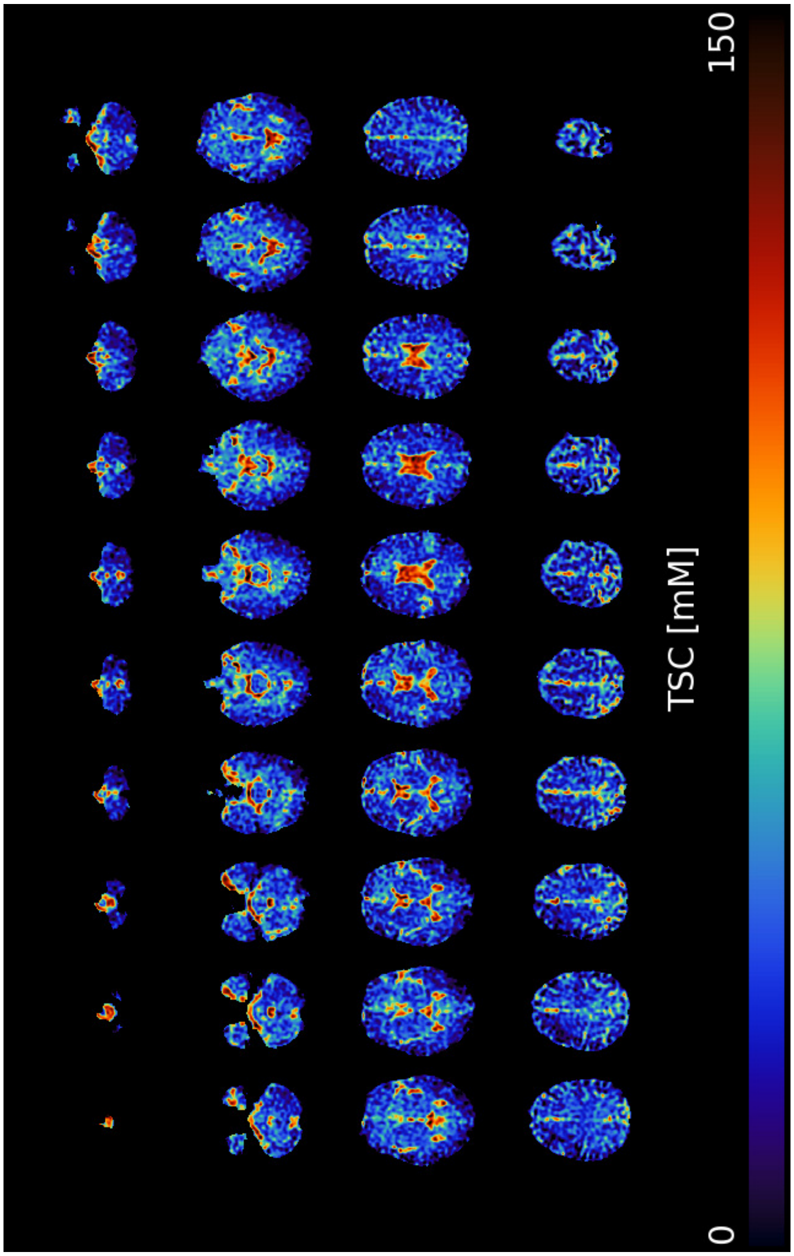

Figure A.5: TSC map from internal brain calibrations in mM.

Bibliography

[1] Andrea M. Rose and Roland Valdes. Understanding the sodium pump and its relevance to disease. *Clinical Chemistry*, 40(9):1674–1685, 1994. ISBN: 0009-9147.

[2] Jens Christian Skou and Mikael Esmann. The Na, K-ATPase. *Journal of Bioenergetics and Biomembranes*, 24(3):249–261, 1992.

[3] D. F. Rolfe and G. C. Brown. Cellular energy utilization and molecular origin of standard metabolic rate in mammals. *Physiological Reviews*, 77(3):731–758, July 1997.

[4] Martin Koltzenburg and Tarek Yousry. Magnetic resonance imaging of skeletal muscle. *Current Opinion in Neurology*, 20(5):595–599, October 2007.

[5] Meng Law, Peter M Som, and Thomas P Naidich. *Problem solving in neuroradiology*. Elsevier/Saunders, Philadelphia, Pa., 2011. OCLC: 848064721.

[6] Jeroen J. Geurts and Frederik Barkhof. Grey matter pathology in multiple sclerosis. *The Lancet Neurology*, 7:841–851, 2008. ISBN: 1474-4422.

[7] Wafaa Zaaraoui, Simon Konstandin, Bertrand Audoin, Armin M Nagel, Audrey Rico, Irina Malikova, Elisabeth Soulier, Patrick Viout, Sylviane Confort-Gouny, Patrick J. Cozzone, Jean Pelletier, Lothar R. Schad, and Jean-Philippe Ranjeva. Distribution of brain sodium accumulation correlates with disability in multiple sclerosis: a cross-sectional 23Na MR imaging study. *Radiology*, 264(3):859–67, September 2012.

[8] Stephen G. Waxman, Matthew J. Craner, and Joel A. Black. Na + channel expression along axons in multiple sclerosis and its models. *Trends in Pharmacological Sciences*, 25(11):584–591, 2004. ISBN: 0165-6147.

[9] Stephen G Waxman. Mechanisms of disease: sodium channels and neuroprotection in multiple sclerosis-current status. *Nature clinical practice. Neurology*, 4(3):159–169, 2008. ISBN: 1745-8358 (Electronic).

[10] Kenneth J. Smith. Sodium channels and multiple sclerosis: Roles in symptom production, damage and therapy. *Brain Pathology*, 17(2):230–242, 2007. ISBN: 1015-6305 (Print).

[11] P K Stys, S G Waxman, and B R Ransom. Ionic mechanisms of anoxic injury in mammalian CNS white matter: role of Na+ channels and Na(+)-Ca2+ exchanger. *The Journal of neuroscience : the official*

journal of the Society for Neuroscience, 12(2):430–9, 1992. ISBN: 0270-6474 (Print) 0270-6474 (Linking).

[12] Philipp Eisele, Simon Konstandin, Kristina Szabo, Anne Ebert, Christina Roßmanith, Nadia Paschke, Martin Kerschensteiner, Michael Platten, Stefan O. Schoenberg, Lothar R. Schad, and Achim Gass. Temporal evolution of acute multiple sclerosis lesions on serial sodium (23Na) MRI. *Multiple Sclerosis and Related Disorders*, 29:48–54, April 2019.

[13] Grazia Daniela Femminella, Tony Thayanandan, Valeria Calsolaro, Klara Komici, Giuseppe Rengo, Graziamaria Corbi, and Nicola Ferrara. Imaging and Molecular Mechanisms of Alzheimer's Disease: A Review. *International Journal of Molecular Sciences*, 19(12):3702, December 2018. Number: 12 Publisher: Multidisciplinary Digital Publishing Institute.

[14] Grazia D. Femminella and Paul Edison. Evaluation of neuroprotective effect of glucagon-like peptide 1 analogs using neuroimaging. *Alzheimer's & Dementia*, 10(1S):S55–S61, 2014. _eprint: https://alz-journals.onlinelibrary.wiley.com/doi/pdf/10.1016/j.jalz.2013.12.012.

[15] Clifford R Jack, David S Knopman, William J Jagust, Leslie M Shaw, Paul S Aisen, Michael W Weiner, Ronald C Petersen, and John Q Trojanowski. Hypothetical model of dynamic biomarkers of the Alzheimer's pathological cascade. *Lancet neurology*, 9(1):119, January 2010.

[16] E. A. Mellon, D. T. Pilkinton, C. M. Clark, M. A. Elliott, W. R. Witschey, A. Borthakur, and R. Reddy. Sodium MR Imaging Detection of Mild Alzheimer Disease: Preliminary Study. *American Journal of Neuroradiology*, 30(5):978–984, May 2009. Publisher: American Journal of Neuroradiology Section: FUNCTIONAL.

[17] Sherif A. Mohamed, Katrin Herrmann, Anne Adlung, Nadia Paschke, Lucrezia Hausner, Lutz Frölich, Lothar Schad, Christoph Groden, and Hans Ulrich Kerl. Evaluation of Sodium (23Na) MR-imaging as a Biomarker and Predictor for Neurodegenerative Changes in Patients With Alzheimer's Disease. *In Vivo*, 35(1):429–435, January 2021. Publisher: International Institute of Anticancer Research Section: Clinical Studies.

[18] L M DeAngelis. Brain tumors. *The New England journal of medicine*, 344(2):114–23, January 2001.

[19] Quinn T Ostrom, Haley Gittleman, Peter Liao, Toni Vecchione-Koval, Yingli Wolinsky, Carol Kruchko, and Jill S Barnholtz-Sloan. CBTRUS Statistical Report: Primary brain and other central nervous system tumors diagnosed in the United States in 2010–2014. *Neuro-Oncology*, 19(suppl_5):v1–v88, November 2017.

[20] G Thompson, S J Mills, David J. Coope, J P B O'Connor, and Alan Jackson. Imaging biomarkers of angiogenesis and the microvascular environment in cerebral tumours. *The British journal of radiology*, 84 Spec No:S127–44, December 2011. ISBN: 9781461490296.

[21] Balveen Kaur, Fatima W Khwaja, Eric A Severson, Shannon L Matheny, Daniel J Brat, and Erwin G Van Meir. Hypoxia and the hypoxia-inducible-factor pathway in glioma growth and angiogenesis. *Neuro-oncology*, 7(2):134–53, April 2005. ISBN: 1522-8517.

[22] Ronald Ouwerkerk, Karen B Bleich, Joseph S Gillen, Martin G Pomper, and Paul A Bottomley. Tissue sodium concentration in human brain tumors as measured with 23Na MR imaging. *Radiology*, 227(2):529–37, May 2003.

[23] Armin Michael Nagel, Michael Bock, Christian Hartmann, Lars Gerigk, Jan-Oliver Neumann, Marc-André Weber, Martin Bendszus, Alexander Radbruch, Wolfgang Wick, Heinz-Peter Schlemmer, Wolfhard Semmler, and Armin Biller. The Potential of Relaxation-Weighted Sodium Magnetic Resonance Imaging as Demonstrated on Brain Tumors. *Investigative Radiology*, 46(9):539–547, 2011.

[24] N Weidner. Tumor angiogenesis: review of current applications in tumor prognostication. *Seminars in diagnostic pathology*, 10(4):302–13, November 1993.

[25] David I. Kaplan, Lori L. Isom, and Steven Petrou. Role of Sodium Channels in Epilepsy. *Cold Spring Harbor Perspectives in Medicine*, 6(6):a022814, January 2016. Publisher: Cold Spring Harbor Laboratory Press.

[26] John R. Cressman, Ghanim Ullah, Jokubas Ziburkus, Steven J. Schiff, and Ernest Barreto. The influence of sodium and potassium dynamics

on excitability, seizures, and the stability of persistent states: I. Single neuron dynamics. *Journal of Computational Neuroscience*, 26(2):159–170, April 2009.

[27] Dipan C. Patel, Bhanu P. Tewari, Lata Chaunsali, and Harald Sontheimer. Neuron–glia interactions in the pathophysiology of epilepsy. *Nature Reviews Neuroscience*, 20(5):282–297, May 2019. Number: 5 Publisher: Nature Publishing Group.

[28] Yang Wang, Anthony Majors, Imad Najm, Min Xue, Youssef Comair, Michael Modic, and Thian C. Ng. Postictal Alteration of Sodium Content and Apparent Diffusion Coefficient in Epileptic Rat Brain Induced by Kainic Acid. *Epilepsia*, 37(10):1000–1006, 1996. Publisher: Blackwell Publishing Ltd.

[29] Ben Ridley, Angela Marchi, Jonathan Wirsich, Elisabeth Soulier, Sylviane Confort-Gouny, Lothar Schad, Fabrice Bartolomei, Jean-Philippe Ranjeva, Maxime Guye, and Wafaa Zaaraoui. Brain sodium MRI in human epilepsy: Disturbances of ionic homeostasis reflect the organization of pathological regions. *NeuroImage*, 157(Complete):173–183, 2017. Publisher: Elsevier.

[30] A. Hagiwara, M. Bydder, T.C. Oughourlian, J. Yao, N. Salamon, R. Jahan, J.P. Villablanca, D.R. Enzmann, and B.M. Ellingson. Sodium MR Neuroimaging. *American Journal of Neuroradiology*, 42(11):1920–1926, November 2021.

[31] G. Schlaug, A. Benfield, A. E. Baird, B. Siewert, K. O. Lövblad, R. A. Parker, R. R. Edelman, and S. Warach. The ischemic penumbra Operationally defined by diffusion and perfusion MRI. *Neurology*, 53(7):1528–1537, 1999. ISBN: 0028-3878.

[32] Adrian Tsang, Robert W. Stobbe, Negar Asdaghi, Muhammad S. Hussain, Yusuf A. Bhagat, Christian Beaulieu, Derek Emery, and Ken S. Butcher. Relationship between sodium intensity and perfusion deficits in acute ischemic stroke. *Journal of Magnetic Resonance Imaging*, 33(1):41–47, 2011. ISBN: 1522-2586.

[33] Keith R. Thulborn, Denise Davis, James Snyder, Howard Yonas, and Amin Kassam. Sodium MR Imaging of Acute and Subacute Stroke for Assessment of Tissue Viability. *Neuroimaging Clinics of North America*, 15(3):639–653, 2005.

[34] AHS Holbourn. The mechanics of brain injuries. *British medical bulletin*, 3(6):147–149, 1945.

[35] AK Ommaya, RL Grubb, and RA Naumann. Coup and contre-coup injury: observations on the mechanics of visible brain injuries in the rhesus monkey. *Journal of neurosurgery*, 35(5):503–16, November 1971. ISBN: 0022-3085.

[36] Christopher C. Giza and David A. Hovda. The new neurometabolic cascade of concussion. *Neurosurgery*, 75 Suppl 4(6228):S24–33, October 2014. ISBN: 6314442508.

[37] Michael L Lipton, Namhee Kim, Young K Park, Miriam B Hulkower, Tova M Gardin, Keivan Shifteh, Mimi Kim, Molly E Zimmerman, Richard B Lipton, and Craig a Branch. Robust detection of traumatic axonal injury in individual mild traumatic brain injury patients: intersubject variation, change over time and bidirectional changes in anisotropy. *Brain imaging and behavior*, 6(2):329–42, June 2012.

[38] Jeffrey J Bazarian, Jianhui Zhong, Brian Blyth, Tong Zhu, Voyko Kavcic, and Derick Peterson. Diffusion tensor imaging detects clinically important axonal damage after mild traumatic brain injury: a pilot study. *Journal of neurotrauma*, 24(9):1447–59, September 2007.

[39] Paul Polak, John J. Leddy, Michael G. Dwyer, Barry Willer, and Robert Zivadinov. Diffusion Tensor Imaging Alterations in Patients With Postconcussion Syndrome Undergoing Exercise Treatment. *Journal of Head Trauma Rehabilitation*, 30(2):E32–E42, April 2015.

[40] M Reinert, A Khaldi, A Zauner, E Doppenberg, S Choi, and R Bullock. High level of extracellular potassium and its correlates after severe head injury: relationship to high intracranial pressure. *Journal of neurosurgery*, 93(5):800–807, 2000. ISBN: 0022-3085.

[41] Matthew P MacFarlane and Thomas C Glenn. Neurochemical cascade of concussion. *Brain injury*, 29(2):139–153, 2015. ISBN: 10.3109/02699052.2014.965208.

[42] Meeryo C. Choe. The Pathophysiology of Concussion. *Current Pain and Headache Reports*, 20(6):42, June 2016. Publisher: Current Pain and Headache Reports ISBN: 1934-1563.

[43] John T Povlishock and Douglas I Katz. Update of neuropathology and neurological recovery after traumatic brain injury. *The Journal of head trauma rehabilitation*, 20(1):76–94, 2005.

[44] Chen, AM, Gerhalter, T, Dehkharghani, S, Peralta, R, Adiparvar, F, Babb, JS, Bushnik, T, Silver, JM, Im, BS, Wall, SP, Brown, R, Baete, S, Kirov, II, and Madelin, G. Quantitative sodium and diffusion imaging of mild traumatic brain injury: regional analysis ndings. In *Proceedings of the 2021 ISMRM & SMRT Annual Meeting Exhibition*, May 2021.

[45] Teresa Gerhalter, Anna M Chen, Seena Dehkharghani, Rosemary Peralta, Fatemeh Adlparvar, James S Babb, Tamara Bushnik, Jonathan M Silver, Brian S Im, Stephen P Wall, Ryan Brown, Steven H Baete, Ivan I Kirov, and Guillaume Madelin. Global decrease in brain sodium concentration after mild traumatic brain injury. *Brain Communications*, 3(fcab051), April 2021.

[46] Olaf Kühl. *Phosphoros-31 NMR spectroscopy: a concise introduction for the synthetic organic and organometallic chemist*. Springer, Berlin Heidelberg, 2008. OCLC: 310127955.

[47] Malcolm H. Levitt. *Spin dynamics: basics of nuclear magnetic resonance*. John Wiley & Sons, Chichester, England ; Hoboken, NJ, 2nd ed edition, 2008. OCLC: ocn141380283.

[48] Slichter, Charles P. *Principles of Magnetic Resonance*. Springer, Berlin, Heidelberg, 1990. OCLC: 992863340.

[49] Guillaume Madelin, Jae Seung Lee, Ravinder R. Regatte, and Alexej Jerschow. Sodium MRI: Methods and applications. *Progress in Nuclear Magnetic Resonance Spectroscopy*, 79:14–47, 2014. Publisher: Elsevier B.V.

[50] Ileana Hancu, Johan R.C. van der Maarel, and Fernando E. Boada. A Model for the Dynamics of Spins 3/2 in Biological Media: Signal Loss during Radiofrequency Excitation in Triple-Quantum-Filtered Sodium MRI. *Journal of Magnetic Resonance*, 147(2):179–191, December 2000.

[51] Costin Tanase and Fernando E. Boada. Algebraic description of spin 3/2 dynamics in NMR experiments. *Journal of Magnetic Resonance*, 173(2):236–253, 2005. ISBN: 1090-7807.

[52] Gil Navon, Hadassah Shinar, Uzi Eliav, and Yoshiteru Seo. Multiquantum filters and order in tissues. *NMR in Biomedicine*, 14(2):112–132, 2001. ISBN: 0952-3480.

[53] Johan R.C. van der Maarel. Thermal relaxation and coherence dynamics of spin 3/2. I. Static and fluctuating quadrupolar interactions in the multipole basis. *Concepts in Magnetic Resonance*, 19A(2):97–116, 2003.

[54] Johan R.C. van der Maarel. Thermal relaxation and coherence dynamics of spin 3/2. II. Strong radio-frequency field. *Concepts in Magnetic Resonance*, 19A(2):117–133, 2003.

[55] Walther Gerlach and Otto Stern. Der experimentelle Nachweis der Richtungsquantelung im Magnetfeld. *Zeitschrift fur Physik*, 9(1):349–352, December 1922.

[56] Horst Schmidt-Böcking, Lothar Schmidt, Hans Jürgen Lüdde, Wolfgang Trageser, Alan Templeton, and Tilman Sauer. The Stern-Gerlach experiment revisited. *The European Physical Journal H*, 41(4):327–364, November 2016.

[57] WebElements: Extended periodic table, March 2022. URL:https://www.webelements.com Accessed:2022-03-07.

[58] W. D. Rooney and C. S. Springer. A comprehensive approach to the analysis and interpretation of the resonances of spins 3/2 from living systems. *NMR in biomedicine*, 4(5):209–226, October 1991.

[59] W. D. Rooney and C. S. Springer. The molecular environment of intracellular sodium: 23Na NMR relaxation. *NMR in biomedicine*, 4(5):227–245, October 1991.

[60] Arijitt Borthakur, Eric Mellon, Sampreet Niyogi, Walter Witschey, J Bruce Kneeland, and Ravinder Reddy. Sodium and T1rho MRI for molecular and diagnostic imaging of articular cartilage. *NMR in biomedicine*, 19(7):781–821, 2006. ISBN: 0952-3480.

[61] Robert W. Brown, Yu-Chung N. Cheng, E. Mark Haacke, Michael R. Thompson, and Ramesh Venkatesan. *Magnetic resonance imaging: physical principles and sequence design*. John Wiley & Sons, Inc, Hoboken, New Jersey, second edition edition, 2014.

[62] Frank Riemer, Bhavana Shantilal Solanky, Matthew Clemence, Claudia Wheeler-Kingshott, and Xavier Golay. Bi-exponential 23Na T2* components analysis in the human brain. *Proc Intl Soc Mag Reson Med 20*, 20(133), 2012.

[63] Guillaume Madelin, Richard Kline, Ronn Walvick, and Ravinder R. Regatte. A method for estimating intracellular sodium concentration and extracellular volume fraction in brain in vivo using sodium magnetic resonance imaging. *Scientific Reports*, 4:1–7, 2014.

[64] Arthur Coste, Fawzi Boumezbeur, Alexandre Vignaud, Guillaume Madelin, Kathrin Reetz, Denis Le Bihan, Cécile Rabrait-Lerman, and Sandro Romanzetti. Tissue sodium concentration and sodium T1 mapping of the human brain at 3 T using a Variable Flip Angle method. *Magnetic Resonance Imaging*, 58:116–124, May 2019.

[65] Greg J Stanisz, Ewa E Odrobina, Joseph Pun, Michael Escaravage, Simon J Graham, Michael J Bronskill, and R Mark Henkelman. T1, T2 relaxation and magnetization transfer in tissue at 3T. *Magnetic resonance in medicine : official journal of the Society of Magnetic Resonance in Medicine / Society of Magnetic Resonance in Medicine*, 54(3):507–12, September 2005.

[66] William D Rooney, Glyn Johnson, Xin Li, Eric R Cohen, Seong-Gi Kim, Kamil Ugurbil, and Charles S Springer. Magnetic field and tissue dependencies of human brain longitudinal 1H2O relaxation in vivo. *Magnetic resonance in medicine : official journal of the Society of Magnetic Resonance in Medicine / Society of Magnetic Resonance in Medicine*, 57(2):308–18, February 2007.

[67] S. K. Hilal, A. A. Maudsley, J. B. Ra, H. E. Simon, P. Roschmann, S. Wittekoek, Z. H. Cho, and S. K. Mun. In vivo NMR imaging of sodium-23 in the human head. *Journal of Computer Assisted Tomography*, 9(1):1–7, February 1985.

[68] A. A. Maudsley and S. K. Hilal. Biological Aspects of Sodium-23 Imaging. *British Medical Bulletin*, 40(2):165–166, 1984.

[69] Guy Jaccard, Stephen Wimperis, and Geoffrey Bodenhausen. Multiple-quantum NMR spectroscopy of S=3/2 spins in isotropic phase: A new probe for multiexponential relaxation. *The Journal of Chemical Physics*, 85(11):6282, 1986. ISBN: 9780874216561.

[70] Alina Gilles, Armin M. Nagel, and Guillaume Madelin. Multipulse sodium magnetic resonance imaging for multicompartment quantification: Proof-of-concept. *Scientific Reports*, 7(1):17435, December 2017.

[71] Roopa Kalyanapuram, Viswanathan Seshan, and Navin Bansal. Three-dimensional triple-quantum-filtered 23Na imaging of the dog head in vivo. *Journal of Mag-*

netic Resonance Imaging, 8(5):1182–1189, 1998. _eprint: https://onlinelibrary.wiley.com/doi/pdf/10.1002/jmri.1880080527.

[72] James Pekar, Perry F Renshaw, and John S Leigh. Selective detection of intracellular sodium by coherence-transfer NMR. *Journal of Magnetic Resonance (1969)*, 72(1):159–161, March 1987.

[73] Robert B. Hutchison and Joseph I. Shapiro. Measurement of intracellular sodium with NMR methods. *Concepts in Magnetic Resonance*, 3(4):215–236, 1991. _eprint: https://onlinelibrary.wiley.com/doi/pdf/10.1002/cmr.1820030404.

[74] Linda A Jelicks and Raj K Gupta. On the extracellular contribution to multiple quantum filtered 23Na NMR of perfused rat heart. *Magnetic resonance in medicine*, 29(1):130–133, 1993. Publisher: Wiley Online Library.

[75] Linda A Jelicks and Raj K Gupta. Double-quantum NMR of sodium ions in cells and tissues. Paramagnetic quenching of extracellular coherence. *Journal of Magnetic Resonance*, 81(3):586–592, February 1989.

[76] Charles S. Springer. MEASUREMENT OF METAL CATION COMPARTMENTALIZATION IN TISSUE BY HIGH-RESOLUTION METAL CATION NMR. *Annual Review of Biophysics and Biophysical Chemistry*, 16(1):375–399, June 1987.

[77] Patrick M. Winter and Navin Bansal. TmDOTP5– as a 23Na shift reagent for the subcutaneously implanted 9L gliosarcoma in rats. *Magnetic Resonance in Medicine*, 45(3):436–442, 2001.

_eprint: https://onlinelibrary.wiley.com/doi/pdf/10.1002/1522-2594%28200103%2945%3A3%3C436%3A%3AAID-MRM1057%3E3.0.CO%3B2-6.

[78] H. Naritomi, M. Kanashiro, M. Sasaki, Y. Kuribayashi, and T. Sawada. In vivo measurements of intra- and extracellular Na+ and water in the brain and muscle by nuclear magnetic resonance spectroscopy with shift reagent. *Biophysical Journal*, 52(4):611–616, October 1987.

[79] R. K. Gupta, P. Gupta, and R. D. Moore. NMR studies of intracellular metal ions in intact cells and tissues. *Annual Review of Biophysics and Bioengineering*, 13:221–246, 1984.

[80] Susan J. Kohler and Nancy H. Kolodny. Sodium magnetic resonance imaging and chemical shift imaging. *Progress in Nuclear Magnetic Resonance Spectroscopy*, 24(5):411–433, 1992. Publisher: Elsevier.

[81] Guillaume Madelin and Ravinder R. Regatte. Biomedical applications of sodium MRI in vivo. *Journal of magnetic resonance imaging : JMRI*, 38(3):511–29, 2013.

[82] S. S. Winkler. Sodium-23 magnetic resonance brain imaging. *Neuroradiology*, 32(5):416–420, 1990.

[83] A.R. Bogdan, H.L. Kundel, P. Joseph, L. Ayes, and E. High. Dextran-magnetite as a contrast agent for sodium MR imaging of pulmonary edema. United States, 1988. Radiological Society of North America Inc.

[84] R. M. Summers, P. M. Joseph, P. F. Renshaw, and H. L. Kundel. Dextran-magnetite: a contrast agent for sodium-23 MRI. *Magnetic Resonance in Medicine*, 8(4):427–439, December 1988.

[85] Joel C. Watkins and Eiichi Fukushima. High-pass bird-cage coil for nuclear-magnetic resonance. *Review of Scientific Instruments*, 59(6):926–929, June 1988.

[86] Matt A Bernstein, KF Kevin F King, and XJ Xiaohong Joe Zhou. *Handbook of MRI pulse sequences*, volume 1. Elsevier Academic Press, Burlington, MA, 1 edition, April 2004. ISSN: 00942405.

[87] Donald W. McRobbie, Moore, Elizabeth A., Graves, Martin J., and Prince, Martin R. *MRI from picture to proton*. Cambridge University Press, Cambridge, UK ; New York, 2nd ed edition, 2007.

[88] R Mezrich. A perspective on K-space. *Radiology*, 195(2):297–315, May 1995.

[89] Armin M. Nagel, Frederik B. Laun, Marc-André Weber, Christian Matthies, Wolfhard Semmler, and Lothar R. Schad. Sodium MRI using a density-adapted 3D radial acquisition technique. *Magnetic Resonance in Medicine*, 62(6):1565–1573, 2009.

[90] James G. Pipe, Nicholas R. Zwart, Eric A. Aboussouan, Ryan K. Robison, Ajit Devaraj, and Kenneth O. Johnson. A new design and rationale for 3D orthogonally oversampled k-space trajectories. *Magnetic Resonance in Medicine*, 66(5):1303–1311, 2011.

[91] Sònia Nielles-Vallespin, Marc André Weber, Michael Bock, André Bongers, Peter Speier, Stephanie E. Combs, Johannes Wöhrle, Frank Lehmann-Horn, Marco Essig, and Lothar R. Schad. 3D radial projection technique with ultrashort echo times for sodium MRI: Clinical applications in human brain and skeletal muscle. *Magnetic Resonance in Medicine*, 57(1):74–81, 2007. ISBN: 0740-3194 (Print)\n0740-3194 (Linking).

[92] R. Jerecic, M. Bock, C. Wacker, W. Bauer, and L.R. Schad. 23NA-MRI OF THE HUMAN HEART USING A 3D RADIAL PROJECTION TECHNIQUE. *Biomedizinische Technik/Biomedical Engineering*, 47(s1a):458–459, 2002.

[93] J G Pipe and P Menon. Sampling density compensation in MRI: rationale and an iterative numerical solution. *Magnetic resonance in medicine : official journal of the Society of Magnetic Resonance in Medicine / Society of Magnetic Resonance in Medicine*, 41(1):179–86, January 1999.

[94] W.Q. Malik, H.a. Khan, D.J. Edwards, and C.J. Stevens. A gridding algorithm for efficient density compensation of arbitrarily sampled Fourier-domain data. In *IEEE/Sarnoff Symposium on Advances in Wired and Wireless Communication, 2005.*, pages 125–128. IEEE, 2005.

[95] Olgica Zaric, Katja Pinker, Stefan Zbyn, Bernhard Strasser, Simon Robinson, Lenka Minarikova, Stephan Gruber, Alex Farr, Christian Singer, Thomas H. Helbich, Siegfried Trattnig, and Wolfgang Bogner.

Quantitative Sodium MR Imaging at 7 T: Initial Results and Comparison with Diffusion-weighted Imaging in Patients with Breast Tumors. *Radiology*, 280(1):39–48, July 2016.

[96] Michael A. Jacobs. Multiparametric Magnetic Resonance Imaging of Breast Cancer. *Journal of the American College of Radiology*, 6(7):523–526, July 2009.

[97] Michael A. Jacobs, Ronald Ouwerkerk, Ihab Kamel, Paul A. Bottomley, David A. Bluemke, and Hyun S. Kim. Proton, diffusion-weighted imaging, and sodium (23Na) MRI of uterine leiomyomata after MR-guided high-intensity focused ultrasound: A preliminary study. *Journal of Magnetic Resonance Imaging*, 29(3):649–656, 2009. _eprint: https://onlinelibrary.wiley.com/doi/pdf/10.1002/jmri.21677.

[98] Rolf F. Schulte, Laura Sacolick, Martin H. Deppe, Martin A. Janich, Markus Schwaiger, Jim M. Wild, and Florian Wiesinger. Transmit gain calibration for nonproton MR using the Bloch–Siegert shift. *NMR in Biomedicine*, 24(9):1068–1072, November 2011.

[99] Martin Uecker, Frank Ong, Jonathan I Tamir, Dara Bahri, Patrick Virtue, Joseph Y Cheng, Tao Zhang, and Michael Lustig. Berkeley Advanced Reconstruction Toolbox. In *Proc Intl Soc Mag Reson Med*, page 2486, Toronto, CA, 2015.

[100] Stephen M Smith, Mark Jenkinson, Mark W Woolrich, Christian F Beckmann, Timothy E J Behrens, Heidi Johansen-berg, Peter R Bannister, Marilena De Luca, Ivana Drobnjak, David E Flitney, Rami K

Niazy, James Saunders, John Vickers, Yongyue Zhang, Nicola De Stefano, J Michael Brady, Paul M Matthews, Marilena De Luca, and Nicola De Stefano. Advances in functional and structural MR image analysis and implementation as FSL. *NeuroImage*, 23 Suppl 1:S208–19, January 2004.

[101] Antonio González-López, Pedro Antonio Campos-Morcillo, and José Domingo Lago-Martín. Technical Note: An oversampling procedure to calculate the MTF of an imaging system from a bar-pattern image. *Medical physics*, 43(10):5653, 2016.

[102] JD Hunter. Matplotlib: A 2D graphics environment. *Computing in Science & Engineering*, 9(3):90–95, 2007.

[103] Glyn O. Phillips and Peter A. Williams, editors. *Handbook of hydrocolloids*. Woodhead publishing in food science and technology. CRC Press [u.a.], Boca Raton, Fla., repr edition, 2005.

[104] Donald E. Woessner. NMR relaxation of spin-3/2 nuclei: Effects of structure, order, and dynamics in aqueous heterogeneous systems. *Concepts in Magnetic Resonance*, 13(5):294–325, 2001. _eprint: https://onlinelibrary.wiley.com/doi/pdf/10.1002/cmr.1015.

[105] Geoffrey S Payne and Peter Styles. Multiple-quantum-filtered 23Na NMR spectroscopy in model systems. *Journal of Magnetic Resonance (1969)*, 95(2):253–266, 1991. Publisher: Elsevier Science.

[106] Kevin D. Harkins, Mark D. Does, and William A. Grissom. Iterative Method for Predistortion of MRI Gradient Waveforms. *IEEE Transac-*

tions on Medical Imaging, 33(8):1641–1647, August 2014. Conference Name: IEEE Transactions on Medical Imaging.

[107] Hui Liu and Gerald B. Matson. Accurate Measurement of Magnetic Resonance Imaging Gradient Characteristics. *Materials*, 7(1):1–15, January 2014. Number: 1 Publisher: Multidisciplinary Digital Publishing Institute.

[108] Alireza Akbari. *Development and Optimization of Sodium Magnetic Resonance Advanced Techniques in the In Vivo Assessment of Human Musculoskeletal Tissue*. PhD thesis, McMaster University, 2016.

[109] Katherine L. Wright, Jesse I. Hamilton, Mark A. Griswold, Vikas Gulani, and Nicole Seiberlich. Non-Cartesian parallel imaging reconstruction. *Journal of Magnetic Resonance Imaging*, 40(5):1022–1040, 2014. _eprint: https://onlinelibrary.wiley.com/doi/pdf/10.1002/jmri.24521.

[110] Kelvin J. Layton, Stefan Kroboth, Feng Jia, Sebastian Littin, Huijun Yu, and Maxim Zaitsev. Trajectory optimization based on the signal-to-noise ratio for spatial encoding with nonlinear encoding fields. *Magnetic Resonance in Medicine*, 76(1):104–117, 2016. _eprint: https://onlinelibrary.wiley.com/doi/pdf/10.1002/mrm.25859.

[111] Carlotta Ianniello, Guillaume Madelin, Linda Moy, and Ryan Brown. A dual-tuned multichannel bilateral RF coil for 1H/23Na breast MRI at 7 T. *Magnetic Resonance in Medicine*, 82(4):1566–1575, 2019. _eprint: https://onlinelibrary.wiley.com/doi/pdf/10.1002/mrm.27829.

[112] Joshua D. Kaggie, J. Rock Hadley, James Badal, John R. Campbell, Daniel J. Park, Dennis L. Parker, Glen Morrell, Rexford D. Newbould, Ali F. Wood, and Neal K. Bangerter. A 3 T sodium and proton composite array breast coil. *Magnetic Resonance in Medicine*, 71(6):2231–2242, 2014. arXiv: NIHMS150003 ISBN: 1522-2594.

[113] Karthik Lakshmanan, Ryan Brown, Guillaume Madelin, Yongxian Qian, Fernando Boada, and Graham C. Wiggins. An eight-channel sodium/proton coil for brain MRI at 3 T. *NMR in Biomedicine*, 31(2):e3867, February 2018.

[114] Dong Liang, Bo Liu, Jiunjie Wang, and Leslie Ying. Accelerating SENSE using compressed sensing. *Magnetic resonance in medicine : official journal of the Society of Magnetic Resonance in Medicine / Society of Magnetic Resonance in Medicine*, 62(6):1574–84, December 2009.

[115] Michael Lustig and John M Pauly. SPIRiT: Iterative self-consistent parallel imaging reconstruction from arbitrary k-space. *Magnetic resonance in medicine : official journal of the Society of Magnetic Resonance in Medicine / Society of Magnetic Resonance in Medicine*, 64(2):457–71, August 2010.

[116] Martin Uecker, Peng Lai, Mark J. Murphy, Patrick Virtue, Michael Elad, John M. Pauly, Shreyas S. Vasanawala, and Michael Lustig. ESPIRiT - An eigenvalue approach to autocalibrating parallel MRI: Where SENSE meets GRAPPA. *Magnetic Resonance in*

Medicine, 71(3):990–1001, 2014. arXiv: 15334406 ISBN: 1522-2594 (Electronic)\r0740-3194 (Linking).

[117] Friedrich Wetterling, Martin Tabbert, Sven Junge, Lindsay Gallagher, I. Mhairi MacRae, and Andrew J. Fagan. A double-tuned 1H/23Na dual resonator system for tissue sodium concentration measurements in the ratbrain via Na-MRI. *Physics in Medicine and Biology*, 55(24):7681–7695, 2010. ISBN: 0031-9155.

[118] F. David Doty, George Entzminger, Jatin Kulkarni, Kranti Pamarthy, and John P. Staab. Radio frequency coil technology for small-animal MRI. *NMR in Biomedicine*, 20(3):304–325, 2007.

[119] Rigoberto Pérez de Alejo, Carlos Garrido, Palmira Villa, Ignacio Rodriguez, Juan José Vaquero, Jesús Ruiz-Cabello, and Manuel Cortijo. Automatic tuning and matching of a small multifrequency saddle coil at 4.7 T. *Magnetic Resonance in Medicine*, 51(4):869–873, 2004.

[120] Sung-Min Sohn, Lance DelaBarre, Anand Gopinath, and John Thomas Vaughan. Design of an Electrically Automated RF Transceiver Head Coil in MRI. *IEEE Transactions on Biomedical Circuits and Systems*, 9(5):725–732, October 2015. Conference Name: IEEE Transactions on Biomedical Circuits and Systems.

[121] Mohammad Sabati and Andrew A. Maudsley. Fast and high-resolution quantitative mapping of tissue water content with full brain coverage for clinically-driven studies. *Magnetic Resonance Imaging*, 31(10):1752–1759, December 2013.